12-2019

Assessment of Hydroclimate Responses to Anthropogenic Forcing and Implications for Human Systems

Deeksha Rastogi
University of Tennessee, drastogi@vols.utk.edu

To the Graduate Council:

I am submitting herewith a dissertation written by Deeksha Rastogi entitled "Assessment of Hydroclimate Responses to Anthropogenic Forcing and Implications for Human Systems." I have examined the final electronic copy of this dissertation for form and content and recommend that it be accepted in partial fulfillment of the requirements for the degree of Doctor of Philosophy, with a major in Energy Science and Engineering.

Moetasim Ashfaq, Major Professor

We have read this dissertation and recommend its acceptance:

Moetasim Ashfaq, Katherine J. Evans, Asad Khattak, Salil Mahajan, Auroop Ganguly

Accepted for the Council:

Dixie L. Thompson

Vice Provost and Dean of the Graduate School

(Original signatures are on file with official student records.)

Assessment of Hydroclimate Responses to Anthropogenic Forcing and Implications for Human Systems

A Dissertation Presented for the

Doctor of Philosophy

Degree

The University of Tennessee, Knoxville

Deeksha Rastogi

December 2019

Acknowledgements

I express sincere gratitude to my doctoral advisor Dr. Moetasim Ashfaq and highly appreciate his valuable guidance and encouragement throughout the Doctor of Philosophy program. I thank Dr. Kate Evans for being a wonderful mentor, constantly believing in me and providing scientific insights. I gratefully acknowledge Dr. Shih-Chieh Kao at Oak Ridge National Laboratory (ORNL), Dr. Flavio Lehner at National Center for Atmospheric Research (NCAR) and Dr. Scott Holladay at The University of Tennessee, Knoxville (UTK) for their crucial guidance in the development of the studies that led to a comprehensive dissertation. I also acknowledge Dr. Asad Khattak, Dr. Auroop Ganguly and Dr. Salil Mahajan for their valued scientific inputs at different stages of dissertation development.

I am thankful for the Bredesen Center fellowship award for interdisciplinary research and graduate education at UTK and ORNL that enabled this research. The support was primarily provided by the Energy Exascale Earth System Model (E3SM), U.S. Department of Energy, Office of Science, Office of Biological and Environmental Research. I am also grateful for the Advance Study fellowship awarded by Graduate Visitor Program at NCAR that provided support for part of the research. The research used resources of the Oak Ridge Leadership Computing Facility at ORNL and Computational Information Systems Laboratory at NCAR.

Abstract

Changes in the mean and extreme climate characteristics are undeniably evident in observational records. Over the United States, the mean temperature has approximately increased by 1°C since the late 19th century and an additional warming of up to 2.2°C is projected by the mid 21st century. Similarly, changes in the temperature and precipitation extremes are also visible through a decreasing trend in the number of rain days and an increasing trend in the frequency of droughts, heat waves and heavy downpours. Discernable evidence suggests that such changes in hydroclimate characteristic are impacting human systems such as energy, agriculture and critical infrastructure. Within this context, this research investigates the responses of regional hydroclimate over the United States to projected increases in radiative forcing in the near term future and its implications for the human systems. This investigation is divided in four parts. The first part quantifies potential changes in county-level residential space heating and cooling requirements as a result of projected changes in heating and cooling degree days. The second part investigates the characteristics of dry versus humid heatwaves and the associated thermodynamic changes in the present and warmer future climate. The third part studies changes in the spatial and temporal characteristics of precipitation events, including extent, intensity and frequency in response to increase in radiative forcing. The fourth part evaluates potential changes in the magnitude of probable maximum precipitation, which is used as a design criteria for critical infrastructure, in the warmer and moister future climate over a hydrological basin in the southeastern United States. Overall, this research should enable development of rigorous analytical frameworks for better planning to cope with the challenges posed by climate change.

Table of Contents

List of Tables

List of Figures

Chapter 1

Introduction

Continued warming of earth's atmosphere has resulted in changes in the mean and extreme climate characteristics. These variations include, but are not limited to, sub seasonal to seasonal shifts in the mean temperature and precipitation distributions, changes in the characteristics of low frequency and high intensity wet, hot and dry extremes [*Diffenbaugh et al*., 2017]. In particular, over the United States (hereafter US), annual average temperature has increased by 1°C since the late 19th century [*Vose*, 2017]. Recent climate projections suggest a further warming of up to 2.2°C across the US by the mid 21st century [*Ashfaq et al*., 2016; *Melillo*, 2014]. Given that eight out of ten warmest years on record have occurred in the last 20 years, [*NOAA*, 2018], a shift in the temperature distribution is quite evident. More importantly, strongest observed changes in the mean temperature have occurred over the higher elevations in the western US that receive substantial amount of snow, resulting in an earlier snowmelt and consequently changes in the regional hydrological cycle [*Barnett et al*., 2008]. In addition to changes in the mean climate, US has also witnessed extended periods of extreme high temperatures, droughts and floods during the recent past [NOAA 2018]. According to the National Centers for Environmental Information (NCEI) database, US has sustained a total of 241 weather and climate disasters during 1980 to 2018 period exceeding a total cost of $1.6 trillion. These changes in the extremes have been partly driven by an increase in the frequency of precipitation related multi-billion dollar disasters with almost a doubling in the 5 most recent years (11.6 events/year) as compared to the average during 1980 to 2017 period (6 events/year).

In the absence of comprehensive climate legislations to curb greenhouse gases emissions, the prevailing trends are expected to continue or even intensify in the foreseeable near future, which has implications for the human systems such as human settlements, energy, agriculture, transportation routes and other critical infrastructures. For instance, rising temperatures will likely

impact both energy production and energy consumption [*Bartos and Chester*, 2015; *McFarland et al*., 2015; *Wilbanks*, 2008] due to potential reduction in the water availability and enhanced space cooling requirements respectively. Similarly, the projected increase in the hot extremes will increase energy demand during peak hours in the summer months [*Auffhammer et al*., 2017]. Agriculture is another important human system that may experience adverse impacts due to climate change [*Calzadilla et al*., 2013; *Lobell et al*., 2011; *Zhu and Troy*, 2018]. For instance, changes in the temperature distribution is causing a shift in the growing seasons across the US. Excessive heat and reduced water availability, as a result of an increase in the intensity and the frequency of extreme hot days, can potentially cause irreversible damages to the crops resulting in a decrease in yield [*Lesk et al*., 2016; *Lobell et al*., 2013; *Lobell et al*., 2011]. Similarly, changes in the precipitation distribution may increase the need for irrigation [*Wada et al*., 2013] or cause damage to crops due to excessive water [*Rosenzweig et al*., 2002]. Moreover, widespread extreme precipitation events are a major cause of flooding that results in a loss of life and/or damages to critical infrastructures such as transportation networks and electric grids. [*Melillo*, 2014].

Given the multidimensionality of climate change and its potential impacts, the goal of this doctoral dissertation is to develop an analytical framework that provides a benchmark for the evaluation of projected hydroclimate variations and their implications for the human systems. To this end, this research considers use cases related with the temperature and precipitation extremes such as heatwaves, strong and widespread storms and probable maximum precipitation to demonstrate how methodological choices may influence our understanding of impact of future climate change on human lives. Moreover, this work also uses highly resolved climate projections to not only highlight the implications of climatic changes for the US energy system at household level but also

to inform the stakeholders and scientific community of the modeling and analytical needs for climate impact analyses at policy relevant scales.

Overall, this research work consists of four studies that leverage high resolution numerical modeling outputs. The first and the third study utilize one of the most detailed (to date) ensemble of climate simulations over the US [*Ashfaq et al*., 2016] that regionally downscales 11 General Circulation Models (GCMs) from Coupled Model Inter-comparison Project Phase 5 (CMIP5). The second study uses a set of reanalysis driven 13-year high resolution simulations, detailed in *Liu et al*. [2017], conducted using Weather Research Forecasting (WRF) model over the US following the pseudo global warming approach. The fourth study develops a framework using WRF to downscale extreme storms from reanalysis and GCM to fine scale [*Rastogi et al*., 2017]. A brief description of each part is as follows:

- The first part of this research provides a comprehensive picture of the residential energy demand in response to changes in degree days. We develop observations based econometric models that relate the residential energy demand to human population and climatic conditions. Subsequently, these models are used to estimate future changes in both the electricity and the natural gas demands for space heating and cooling [*Rastogi et al*., 2019].
- The second part of this research investigates the characteristics of dry versus humid heatwaves across the US. Using a compound heatwave definition, we identify daily maximum- temperature and apparent temperature heatwaves in a pair of high-resolution convection permitting simulations. Further, we investigate the variations in the thermodynamic factors such as humidity and heat fluxes during the two kind of heatwaves and their role in changing the characteristics of heatwaves in future period.

- The third part of this research focuses on the indirect impacts of climate change on human systems that are driven by changes in precipitation characteristics. For this purpose, we categorize precipitation events in terms of their intensity and spatial extent. Specifically, we apply a continuous component labeling technique on precipitation data to identify mid-size and widespread events. Finally, we examine the historical and future characteristics of selected events. Any change in the characteristics of these hydroclimate extremes has important implications for formulating strategies for damage control planning.
- The fourth part of this research focuses on the evaluation of probable maximum precipitation (PMP) in the southeastern US in a warmer and a moister climate. PMP is used as the strictest design standard for highly important energy-water infrastructures. In this study, we employ WRF model, driven by reanalysis and GCM, for downscaling and maximization of 120 extreme storms to generate PMP estimates for the historical and future periods. The simulated PMP estimates are evaluated against the conventional PMP values and the impact of changing climate on PMP estimates is examined [*Rastogi et al*., 2017].

Chapter 2

Shift in Seasonal Climate Patterns Likely to Impact Residential Energy Consumption in the United States

A version of this chapter was originally published by Deeksha Rastogi, James Scott Holladay, Katherine J. Evans, Ben L. Preston, Moetasim Ashfaq in *Environmental Research Letters*.

Rastogi, D., Holladay, J. S., Evans, K. J., Preston, B. L., & Ashfaq, M. (2019). Shift in seasonal climate patterns likely to impact residential energy consumption in the United States. *Environmental Research Letters, 14*(7), 074006. https://iopscience.iop.org/article/10.1088/1748-9326/ab22d2/meta

Abstract

We develop a highly-resolved ensemble of climate simulations and empirical relationships between weather and household energy consumption to provide one of the most detailed estimates to date for potential climate-driven changes in the United States residential energy demand under the highest greenhouse gas emissions pathway. Our results indicate that more intense and prolonged warm conditions will drive an increase in electricity demand while a shorter and milder cold season will reduce natural gas demand by the mid 21st century. The environmental conditions that favor more cooling degree days in summer and reduced heating degree days in winter are driven by changes in daily maximum temperatures and daily minimum temperatures in the respective seasons. Our results also indicate that climate driven change can potentially reverse impacts of a projected decrease in rural population on residential energy demand. These projected changes in climate-driven energy demand have implications for future energy planning and management.

2.1 Introduction

Frequent occurrences of hotter summers and warmer winters across the United States (US) reflect a potentially permanent change in temperature distribution that is progressively reshaping energy demands [*EPA*, 2014; *Petri and Caldeira*, 2015]. In particular, warming trends are the strongest on record in recent decades with seven out of the ten warmest years since 1998 [EPA 2014]. Given the current trajectory of emissions, most recent temperature projections suggest warming of 1.1°C to 2.2°C across the continental US by the mid 21st century [*Ashfaq et al*., 2016; *Melillo et al*., 2014]. Increase in the mean temperatures is the strongest over the higher elevations and the part of US that presently receive significant amounts of cold season precipitation in the form of snow while southwest and southeast are projected to be the hot spots for increases in maximum temperatures. Additional warming will likely exert further influence on the US energy system making adaptation a necessity to meet the challenges of future energy demand.

Changes in ambient temperatures have implications for the two dominant sources of energy that are used for residential space heating and air conditioning in the US Electricity is the dominant source of energy used for space cooling and therefore temperature increases associated with climate change are anticipated to drive electricity demand associated with greater air conditioning use. A recent study projected that by the end of the 21st century, residential energy costs in relatively warm states (such as Florida) could increase by $200/year [*Huang and Gurney*, 2017]. Meanwhile, natural gas is the dominant fuel source for residential space heating. Hence, demand for natural gas is expected to decline in the future as rising temperatures reduce heating demand [*Wilbanks et al*., 2008]. Nevertheless, given the diversity in the climate characteristics and the magnitude of projected climate change across the US, substantial geographic heterogeneity in the response of residential energy demand (hereafter RED) to climate change should be expected. This

variability will exert contrasting controls on natural gas and electricity demand, leading to inevitable fine-scale variations in the energy system response.

A comprehensive investigation of the fine-scale changes in the RED is important for planning future enhancements to the electricity generation and distribution system, as well as the natural gas pipeline network. There are several technological, societal, economic and environmental factors that will frame the future RED. However, given the interdisciplinary nature of these factors and lack of reliable future estimates for many, it is practically impossible to incorporate their combined influences in a single study. Due to these limitations, this study mainly focuses on the influences of climate driven long-term environmental variations on RED within the context of projected population increase. Thus far, a number of studies have investigated potential variations in the US energy system in the future climate, but results to date are relatively limited. Most of the studies either use spatially and/or temporally aggregated data [*McFarland et al*., 2015; *Sailor and Munoz*, 1997; *Zhou et al*., 2014], or have focused on a particular geographic sub-region within the US [*Amato et al*., 2005; *Maximilian Auffhammer and Aroonruengsawat*, 2011; *Ruth and Lin*, 2006]. Similarly, most of the studies often have only investigated changes in electricity consumption [*Allen et al*., 2016; *M. Auffhammer et al*., 2017; *McFarland et al*., 2015], without considering changes in natural gas demand. Likewise, RED investigations at spatially disaggregated scales so far have obtained future climate data either directly from general circulation models (GCMs) [*Huang and Gurney*, 2016; *Wang and Chen*, 2014] or via statistical downscaling of GCMs [*Dirks et al*., 2015]. While GCMs remain the most reliable tool for understanding future climate change, a mismatch between their resolution and the scales that are relevant for policymaking preclude their direct use when making reliable estimates of climate change impacts [*Ashfaq et al*., 2016; *Ashfaq et al*., 2009; *Diffenbaugh et al*., 2005; *Suggitt et al*.,

2011]. Likewise, statistical downscaling has its own limitations given that it cannot refine climate change signal without altering the simulated process-based climate system response in GCMs [Ashfaq et al, 2013]. Therefore, while computationally expensive and data intensive, regional climate modeling based dynamical downscaling of GCMs remains the most sophisticated methodology for the generation of fine-scale climate projections.

In this study, we seek to build on previous work and provide a more comprehensive and applicable picture of RED in response to climate change. We develop observations based economic models that describe the relationship of RED to human population and climatic conditions. Further, leveraging one of the most detailed (to date) ensemble of climate change simulations over the US. [*Ashfaq et al*., 2016], economic models are used to provide estimates for future changes in residential energy use for space heating and cooling in response to changes in climatic conditions. Our analyses provide estimates for future changes in both electricity and natural gas demand for residential space heating and cooling across the US at the county level.

2.2 Data and Methodology

2.2.1 Data

This study is based on the following datasets:

2.2.1.1 Observed Meteorological Data

Gridded daily maximum temperature (Tmax) and daily minimum temperature (Tmin) from the Parameter-Elevation Regressions on Independent Slopes Model (PRISM) observations [*Daly et al*., 2008] for 1981 to 2005 at 4km horizontal grid spacing.

2.2.1.2 Simulated Meteorological Data

Hybrid downscaled 11-member ensemble of GCMs (see Table 2.1)). (Note: All tables and figures referred in this dissertation are placed in Appendix attached towards the end of this document) from Coupled Model Inter-comparison Project Phase 5 (CMIP5). Each GCM is dynamically downscaled to 18 km horizontal grid spacing over the US using a regional climate model (RegCM4) for 1966 to 2005 in the historical period and 2011 to 2050 in the future period under Representative Concentration Pathway 8.5 (RCP 8.5). The historical period analyses in this study are only limited to 1981 to 2005 simulation period that overlaps with the gridded daily PRISM observations. Details of dynamical downscaling experiments and projections are provided in *Ashfaq et al*. [2016]. The daily Tmax and Tmin from each downscaled ensemble member are bias corrected at 4 km PRISM grid over the continental US through a quantile mapping approach that is detailed in *Ashfaq et al*. [2010]; *Ashfaq et al*. [2013].

2.2.1.3 Energy Data

US Energy Information System (EIA) state-level monthly i) energy consumption data for residential electricity retail sales and natural gas consumption for 1990 to 2005 [*EIA*, 2016a; b], and ii) residential energy consumption survey [*RECS*] data for each of 10 US census divisions (Figure 2.1) for four recent surveys (1997, 2001, 2005 & 2009) RECS data provides percentages of total residential electricity used for space heating and cooling and percentage of total residential natural gas used for space heating at the US census division level (Figure 2.1). It also provides percentage of fuel (electricity versus natural gas) used in a census division for space heating. Given discontinuous RECS data availability and its low temporal variation, we use average RECS data using the four recent surveys while we use EIA demand data for each year.

2.2.1.4 Population Statistics

US Census Bureau yearly population estimates for each county in the US obtained for 1981-2005 [*Census*, 2016].

2.2.2 Methodology

There are multiple steps in the analyses that are detailed in the following sub-sections. Additionally, Figure 2.2 provides a schematic summary of these steps.

2.2.2.1 Heating and Cooling Degree Days

We use degree days to quantify the energy requirements for residential heating and cooling. Heating (Cooling) degree days is defined as the number of degrees (in degree Celsius; °C) to be heated (cooled) below (above) a given threshold. Using a base temperature of 18.3° C (65 degrees Fahrenheit), we employ the UK Met Office equations [*Day*, 2006] to calculate daily heating degree days (HDD) and daily cooling degree days (CDD) at each point on the 4km grid of observations and model simulations. Daily gridded values are aggregated both spatially over the counties and states, and temporally over the months to calculate monthly HDD and CDD for each county and state.

Since both electricity and natural gas are used for heating, we calculate the percentage use of each energy source from averaged RECS data. The average value is disaggregated equally to all counties within each division. We attribute the percentage usage of electricity and natural gas in each county to HDD to obtain the HDD requirement fulfilled by electricity (hereafter HDD_{elec}) and the HDD requirement fulfilled by natural gas (hereafter HDD_{ng}).

2.2.2.2 Econometric Model

Equation 1 and 2 represent the econometric models for residential electricity and natural gas consumption. Each econometric model is based on state level observed EIA energy (electricity or natural gas) consumption, state level degree-days from aggregated PRISM meteorological observations and state level population from Census for 1990 to 2005.

$$\log(E_{sch}^{smy}) = c_e + \alpha_{e0}\left(HDD_{elec}^{smy}\right) + \alpha_{e1}\left(HDD_{elec}^{smy}\right)^2 + \beta_{e0}(CDD^{smy}) + \beta_{e1}(CDD^{smy})^2 + \gamma_{e0}\left(P_{sy}\right) + f_s + f_m + \varepsilon_o \quad (1)$$

$$\log(NG_{sh}^{smy}) = c_{ng} + \alpha_{ng0}\left(HDD_{ng}^{smy}\right) + \alpha_{ng1}\left(HDD_{ng}^{smy}\right)^2 + \gamma_{ng0}\left(P_{sy}\right) + f_s + f_m + \varepsilon_1 \quad (2)$$

RECS-based percentage usage is applied to total residential electricity and natural gas consumption to obtain the relative shares of electricity (E_{sch}^{cmy}), used for space heating and cooling, and the natural gas (NG_{sh}^{cmy}), used for space heating for state *s*, month *m* and year *y*.

Similarly, HDD_{elec}^{smy} , HDD_{ng}^{smy} and CDD^{smy} are HDD fulfilled by electricity, HDD fulfilled by natural gas and CDD for respective state, month and year. c_e and c_{ng} are constant terms, α_{e0}, α_{e1}, β_{e0}, β_{e1}, γ_{e0}, α_{ng0}, α_{ng1}, γ_{ng0} are coefficients of respective terms as shown in the equations and ε_o, ε_1 are error terms. Additionally, we use f_s and f_m as fixed effects for states and months respectively. Fixed effects are used in a regression model to control for some types of omitted variable bias. The state fixed effects account for the average difference in time-invariant state characteristics. The month of year fixed effects account for common shocks to all states in a month of the year and can capture seasonal patterns unobserved in the data. In this case, inclusion of state and month fixed effects allows control for differences in the magnitude of degree days that arise i) among states because of differences in population size and ii) among months because of seasonal

variations. It should be noted that while the month fixed effects account for intra-annual differences among the states, the differences between years arising from factors such as macroeconomic fluctuations are not incorporated. Moreover, the electricity model uses all months while summer months (June, July and August) are excluded for the natural gas model. Overall, the econometric models are able to precisely estimate the determinants of electricity and natural gas demand. The R-square values for the models are 0.99 and 0.98 respectively and there are significant t-statistics for all the coefficients at 95% significance level. The F-statistics suggest that the results are jointly as well as individually statistically significant (Table 1.2 and 1.3). We also perform additional tests to rule out any temporal or spatial correlation in our datasets. First, we perform regressions using Newey-West standard errors with 45 and 34 lags for electric and natural gas models respectively. Second, we estimate these regression using [*Driscoll and Kraay*, 1998] standard errors. These standard errors are robust to very general forms of temporal and spatial correlation with all coefficients being statistically significant at the 1 % level.

The fixed effect regression models established in equations 1 and 2 are subsequently applied to each of the RegCM4 ensemble members by replacing the PRISM degree days with the simulated degree days in the 25 years in the historical period (1981-2005) and the 40 years period in the future (2011-2050). For the future models, the population is kept at the 2005 level to isolate the variations in energy demand that arise solely because of climatic changes.

2.2.2.3 Energy Data Disaggregation

We devised a weighting method to disaggregate state-level estimated energy consumption data to the county level. This accounts for differences in the population, heating and cooling requirements across counties within each state. First, we calculate monthly electricity and natural gas weighting factors ($wf_{electric}^{cmy}, wf_{ng}^{cmy}$) for each county *c*, every month *m* in a given year *y* (equations 1 and

2). The weight is a product of county population (P_{cy}) for that year and total degree days for that month, normalized by the state total (equations 3 and 4). Total degree days are calculated as the sum of HDD fulfilled by electricity and total CDD $\left(HDD_{elec}^{cmy} + CDD^{cmy}\right)$ for electricity and only HDD fulfilled by natural gas $\left(HDD_{ng}^{cmy}\right)$ for natural gas. Second, electricity (E^{cmy}) and natural gas (NG^{cmy}) consumptions for each county are calculated by multiplying the estimated state consumptions for electricity and natural gas (i.e,, E_{sch}^{smy} , NG_{sch}^{smy}) with the respective weighing factors of the county (equations 5 and 6).

$$wf_{electric}^{cmy} = \frac{\left(HDD_{elec}^{cmy} + CDD^{cmy}\right) * P_{cy}}{\sum_{c=0}^{c}\left(\left(HDD_{elec}^{cmy} + CDD^{cmy}\right) * P_{cy}\right)} \quad (3)$$

$$wf_{ng}^{cmy} = \frac{\left(HDD_{ng}^{cmy}\right) * P_{cy}}{\sum_{c=0}^{c}\left(HDD_{ng}^{cmy} * P_{cy}\right)} \quad (4)$$

$$E^{cmy} = wf_{electric}^{cmy} * E_{sch}^{smy} \quad (5)$$

$$NG^{cmy} = wf_{ng}^{cmy} * NG_{sch}^{smy} \quad (6)$$

2.2.2.4 Time Series Analysis

We investigate annual variations in HDD, CDD, electricity demand and natural gas demand for ten metropolitan areas across the US, New York-Jersey City–White Plains (NY-NJ), Chicago, (IL), Dallas-Fort Worth-Arlington and Houston, (TX), Washington, D.C.-Arlington-Alexandria,

(DC-VA), Philadelphia-Camden-Wilmington, (PA), Miami-Fort Lauderdale-West Palm Beach, (FL), Atlanta-Sandy Springs-Roswell, (GA), Boston-Cambridge Newton, (MA), San Francisco-Oakland-Hayward, (CA), and Seattle-Tacoma-Bellevue,(WA)). We compare the RegCM4 based HDD and CDD with the PRISM observations. While the RegCM4 based electricity and natural gas demands are compared with EIA observations. All the time series are standardized with respect to their means, and the significance of the trend is tested by using the modified Mann-Kendall test with a 95 percent confidence interval. While we perform analyses individually for each of the 11 RegCM4 ensemble members, results are presented as an ensemble mean.

2.3 Results and Discussion

2.3.1 Historical Comparisons

Across the US, residential space heating requirements are generally higher than the space cooling requirements given the higher number of HDD than CDD (Figures 2.3a, 2.3b). Cooler temperatures associated with continental air and higher elevations drive maximum space heating requirements in the north central US (up to >3400 °C) whereas space cooling requirements peak mostly over southern US such as Florida, Texas and parts of the southwest (up to >2000 °C). The spatial variability in the degree days, along with their magnitudes are simulated exceptionally well in the RegCM4 simulations compared to the observations (Figures 2.3a-d).

Observations exhibit a decreasing (increasing) trend in HDD (CDD) across the US, which is also captured in the simulations (Figures 2.3e-h, 2.4-2.5). However, the simulated decrease in HDD (up to 350 °C) is substantially milder than observed (up to 550 °C) over the Rockies, and the strongest observed increase in CDD over the southwest is approximately 1.5 times higher than the simulated trends. The trends in HDD are significant in both the observations and the simulations in most of the western half and parts of the eastern half of the US. However, the increasing trend

in CDD is only significant over parts of the southwest and Pacific Northwest in the observations in contrast to the simulations that also exhibits significant trends over the southeast and parts of the northeast. HDD and CDD trends in ten metropolitan regions exhibit similar characteristics in both the observations and the simulations. For instance, both datasets exhibit a decreasing trend in HDD over all ten regions, which is also statistically significant over three regions. Similarly, both datasets exhibit increasing but insignificant trends in CDD over 9 out of 10 regions (Figures 2.1i, 2.4-2.5). Collectively, these comparisons demonstrate that the downscaled data exhibits good skill in the simulation of the mean HDD and CDD, and first-order skill in the simulation of their historic trends (Figures 2.3-2.5). This is important because historic trends in HDD and CDD provide a precursor for future changes in energy demands in warmer climates.

Driven by the skillfulness of downscaled data in capturing the characteristics of HDD and CDD, simulations-based electric and natural gas demands also compare well with the EIA observations, particularly at low and medium demand levels (< 4000 GWh for electricity and < 60000 MMcf for natural gas) (Figures 2.6-2.8). The simulated electric demand also exhibits skill at the metropolitan level where statistically significant trends are simulated across all ten metropolitan regions in both the RegCM4 simulations and the observations (Figures 2.3i, 2.6) . The trend in simulated natural gas demand compares well with the observations for 7 out of 10 regions (Figures 2.1i, 2.7). Both electricity and natural gas demand exhibit an upward trend, due to the rising population over the historical period.

2.3.2 Future Changes in Energy Demand and Net Cost

To understand the impacts of climate variations on RED, we fix all other factors including population and other economic drivers that may influence energy system response. Such an approach is a standard in the future climate studies. For instance, all RCPs driven GCMs

simulations only simulate climate system response to changes in representative concentration pathways. With population kept at 2005 levels, electricity demand is projected to increase across the US with the exception of some parts of western US, which exhibit a decrease of up to 7% in parts of Arizona, Nevada, and California by 2050 (Figure 2.9a). The magnitude of increase across the rest of the US is up to 10 %. For metropolitan regions considered in this study, an increase in electricity demand is projected for eight out of ten, ranging from approximately 0.5 % for Boston-Cambridge Newton, MA to more than 7% for Miami-Fort Lauderdale-West Palm Beach, FL (Figure 2.9e). In the case of natural gas, the demand is projected to decrease over most of the US (Figure 2.9f) with the exception of parts of some states such as Texas, Arizona, and Florida that exhibit a strong increase. However, these strong percent increases over parts of these states primarily driven by their relatively small natural gas demand during the historical period. Given that natural gas is mainly used for space heating, the decrease in natural gas demand is driven by the changes during the winter months (i.e., September to May). RegCM4 ensemble members show a robust decrease in natural gas demand (up to 4%) across all ten metropolitan centers, which is mainly driven by a decrease in HDD (Figures 2.9f, 2.9g). The decrease is larger during the transition months i.e., April and May in spring, and September and October in fall compared to winter months.

2.3.3 Driving Climate Variations

We investigate the factors driving future changes in RED by defining changes in the summer-like (hereafter summer) and the winter-like (hereafter winter) conditions. Summer (winter) conditions are defined as the longest consecutive period when CDD (HDD) is greater than HDD (CDD). Figure 2.10 shows a comparison of accumulated degree days and degree days per day (CDD for summer and HDD for winter) in the PRISM observations and the RegCM4 simulations for summer

and winter respectively. Accumulated CDD (HDD) range from 0 to >1400 (0 to >4000) °C whereas CDD (HDD) per day range from 0 to 10 (0 to 18) °C during summer (winter). The total and per day degree days are based on the timing and duration of summer and winter. Summer starts as early as April in the south and as late as June/July in the north, with a gradual decrease in the duration (>200 to <40 days) and the cooling requirements (>1400 to <200 °C). Winter starts as early as September in the north and as late as December/January in the south, with a gradual decrease in duration (>280 to <40 days) and heating requirements (>4000 to <400 °C) from north to south. This seasonal duration shift intensifies with the increase (decrease) in latitude and/or elevation for summer (winter) (Figure 2.11)

While electricity is used for both space heating and cooling, future changes in the characteristics of summer and winter suggest that the projected increase in the electricity demand is primarily driven by an increase in the cooling demand. A late onset of winter, particularly over the higher elevations, and an early arrival of summer shrink the length of winter conditions (Figure 2.12) by a few days in the parts of southeast to as much as a month in the parts of the western US, reducing the HDD by 20 °C to as much as 400 °C respectively (Figure 2.13b). On the other hand, there is an increase in the length of summer conditions (Figure 2.12c) by a few degree days in the parts of Pacific Northwest and Rockies to as much as a month in most of the southwest, increasing the CDD by 20 °C to as much as 300 °C respectively (Figure 2.13a). The per day degree day change in heating (cooling) demand that ranges from -0.7 to 0 (0 to 1) °C is mainly driven by changes in minimum (maximum) daily temperature during winter (summer) (Figures 2.13e, 2.13f).

2.3.4 Socioeconomic Drivers

While this study only focuses on the climate driven long-term environmental variations that can potentially influence RED, there are other socioeconomic factors that may reverse, mute or amplify the projected influence of climate-driven changes. We elaborate on such an impact of socioeconomic variations by considering projected changes in population distribution (Figure 2.14a) in our economic model. We use 5-yearly population projections data from Intergovernmental Panel on Climate Change (IPCC) Special Report on Emissions Scenarios (SRES) A2 scenario, which is analogous for RCP8.5 [*EPA*, 2010], and linearly interpolate it at yearly time-scale to match the future period (2011 to 2050). Use of both climate and population changes in our economic model enables comparisons of future changes in energy demand caused by changes in climate (Figures 2.2a, 2.2b) with those caused by changes in both population and climate (Figures 2.14b, 2.14c). With the exception of Texas, California, and Florida where future population increase is projected to be statewide, urban areas are mainly expected to experience population growth. The projected increase in RED due to population increases (Figures 2.14b, 2.14c) in these three states and urban areas across the US will outpace the projected increase in RED due to climate (Figures 2.9a, 2.9b). On the other hand, most of the rural areas are projected to witness a decline in the population (Figure 2.14a); however, climate-driven increase in RED in those rural areas will overwhelm the decrease caused by population changes (Figures 2.9, 2.14). Compared to climate driven changes, our results indicate that an increase (decrease) in urban (rural) population can potentially result in as much as 10 fold increase (as low as 5 fold decrease) in residential electricity demand. Similarly, compared to climate driven changes, increase (decrease) in urban (rural) population can potentially result in as much as 5 fold increase (as low as 5 fold decrease) in natural gas demand.

In addition to changes in the population, economic factors can potentially exert a significant influence on the pace of technological advancements and residential energy prices. Moreover, a growing economy boosts advancement in technology, resulting in more efficient heating and cooling systems, efficient building designs etc. Likewise, factors such as supply and demand variations and inflation in the energy sector can also drive changes in residential energy prices. However, due to the absence of reliable estimates for the future energy supply and demand, economic conditions and technological innovations, no other socioeconomic factors have been considered in this study.

2.4 Summary and Conclusions

This study uses econometric models and one of the most detailed climate projections over the continental US to investigate future variation in residential energy demand by the mid-21st century in response to increases in radiative forcing. The econometric model (RegCM4) exhibits exceptional skill across the US in the prediction (simulation) of the characteristics of RED (degree days). Future climate is projected to exhibit an increase in the span of hot conditions due to the early arrival of summer-like conditions and delay in the onset of winter-like conditions, leading to a net increase in the residential electricity demand and a decrease in the residential natural gas demand by the mid-21st century. However, driven by the spatial heterogeneity in the climate change signal and the background cooling and heating demands, there are important variations in the characteristics of future RED. For instance, counties in the southern half of US and parts of Midwest are projected to experience stronger increases in the residential electricity demand as compared to those in the northeast and northwest. Similarly, the decrease in natural gas demand is higher in the parts of southeast and parts of the south as compared to its demand in the northwest and Midwest. The projected shift in the energy needs from natural gas to electricity may affect

greenhouse gas (GHG) emissions, depending on the source of electricity generation. Electricity generation from natural gas and coal based thermal plants contributes to GHG emissions, while electricity generation from renewable sources such as hydropower and solar does not. An increase in space cooling requirements will necessitate enhanced electricity generation capacity to meet the electricity demand, which may lead to additional construction and operational costs and higher electric bills.

While keeping the main focus on climate driven changes in the future RED, this study also highlights the importance of socioeconomic drivers that may either reverse, mute or amplify the impacts of climate change on energy systems. Using the projected population changes as an example, we demonstrate that while urban areas will likely experience a strong increase in the future RED due mainly to the greater influx of migrating population, rural areas may also exhibit an increase in the future RED due to climate driven changes despite a decline in rural population. However, as previously pointed out, other socioeconomic drivers and technological advancements, which have not been considered in this study, will also be important determining factors of the future changes in energy demand. Lastly, it should also be noted that biases arising from methodological choices such as disaggregation technique, statistical model errors, and uncertainties in the future climate projections may also have influenced our estimates of climate impacts on the future RED. Nonetheless, the results presented in this study should pave the way for the development of more rigorous and comprehensive analysis frameworks for understanding the response of RED to future changes in climate and socioeconomic conditions.

Acknowledgement

This study was supported as part of the Energy Exascale Earth System Model (E3SM) formerly known as Accelerated Climate Modeling for Energy (ACME) project, funded by the U.S. Department of Energy, Office of Science, Office of Biological and Environmental Research. The research also received support from the Oak Ridge National Laboratory Project Development funds and Regional and Global Climate Modeling program of the U.S. Department of Energy (DOE) Office of Science. Support for model simulations, data storage and analysis is provided by the Oak Ridge Leadership Computing Facility at the Oak Ridge National Laboratory (ORNL), which is supported by the Office of Science of the U.S. Department of Energy (DOE). The authors are employees of UT-Battelle, LLC, under contract DEAC05-00OR22725 with the US Department of Energy (DOE). The US government retains and the publisher, by accepting the article for publication, acknowledges that the US government retains a nonexclusive, paid-up, irrevocable, worldwide license to publish or reproduce the published form of this manuscript, or allow others to do so, for US government purposes.

Chapter 3

Increase in Temperature to Drive the Future Amplification of Dry As Well As Humid Heatwaves over the United States

Abstract

The frequency and the intensity of heatwaves in the US is projected to increase in the 21st century. Despite its importance for amplifying heat stress, the role of humidity in future heatwaves is still uncertain. Here, we investigate heatwaves in a pair of high-resolution model simulations that constraint large-scale atmospheric circulations, to understand the thermodynamic impacts on the characteristics of future heatwaves over four regions across the US. We use daily maximum-temperature and apparent temperature to identify dry and humid heatwaves respectively. While the two kinds of heatwaves show differences in Southeast, Northeast-Midwest, their characteristics are largely similar in Central and West US. Further, relative humidity is projected to decrease during dry heatwaves whereas it remains unchanged during the humid heatwaves. However, the increase in daily maximum temperature still intensifies heat stress during the future humid heatwaves across all the regions. Moreover, these results confirm studies using unconstrained climate models and thus underscore that thermodynamic processes are largely sufficient to explain the projected changes during dry heatwaves whereas a weak land-atmosphere coupling exists during humidity driven heatwaves.

3.1 Introduction

Heatwaves, generally defined as persistent hot conditions above certain threshold, severely impact the social-ecological systems by affecting human health and productivity, by exerting stress on energy and other infrastructure, and by adversely impacting agricultural yields and other ecosystems [*Auffhammer et al*., 2017; *Bobb et al*., 2014; *Burke et al*., 2015; *Coffel et al*., 2017; *Lesk et al*., 2016; *Rastogi et al*., 2019]. Upward trends in the frequency, intensity and duration of heatwaves are already evident globally as well as in the United States (US) [*Perkins et al*., 2012; *Shiva et al*., 2019; *Smith et al*., 2013]. These observed changes in the characteristics of heatwaves have been attributed to global warming and are projected to prevail or further exacerbate in response to a projected increase in global temperature [*Dosio et al*., 2018; *Jaeger et al*., 2008; *King et al*., 2018; *Schoetter et al*., 2015]. Additionally, the presence of high humidity levels during heatwaves can further enhance physiological heat stress, and poses severe risks to human health [*Fischer and Knutti*, 2013; *Glaser et al*., 2016] by reducing human body's ability for evaporative cooling and by limiting heat tolerance [*Dunne et al*., 2013; *Sherwood and Huber*, 2010].

The characteristics of a heatwave are defined by a combination of many dynamic (i.e. atmospheric circulations) and thermodynamic factors (such as moisture and heat fluxes). Heatwaves are often associated with atmospheric blocking patterns. Further, the build-up and entrainment of dry and hot air causes dry heatwaves and advection of hot and humid air from warm ocean results in more humid heatwaves. The thermodynamic characteristics of heatwaves also depend on the regional scale land-atmosphere interactions [*Fischer et al*., 2007; *Miralles et al*., 2014; *Raghavendra et al*., 2019; *Russo et al*., 2017]. Land surface processes can play an important role in amplifying or dampening a heatwave by influencing the partitioning of the available energy between sensible and latent heat fluxes. When soil moisture is abundant, higher evaporation results in conversion of

more energy to latent heat, reducing sensible heat and therefore limiting air temperature rise. Conversely, under limited soil moisture conditions, more energy is partitioned towards sensible heat, causing air temperature to intensify and resulting in drier heat [*Cheng et al*., 2019; *Lee et al*., 2016; *Lorenz et al*., 2010; *Ukkola et al*., 2018]. These land-atmosphere interactions are expected to change in response to increase in radiative forcing [*Donat et al*. 2017; *Lee et al*., 2016], which may result in an enhanced surface drying and an increase in atmospheric moisture following the Clausius Clapeyron relationship. Such changes in the thermodynamic characteristics have the potentially to significantly alter the nature of future heatwaves. Many studies [*Lee et al*., 2016; *Teuling et al*., 2010] provide ample evidence regarding the influence of land-atmospheric interactions in the amplification of warming during heatwaves. For instance, reduced evaporative cooling as a result of soil moisture depletion enhanced the record-breaking European heatwave during both in terms of the intensity and duration [*Lorenz et al*., 2010; *Teuling et al*., 2010]. Similarly, soil moisture availability exerts controls on the relationship between latent-sensible heat flux partitioning and the heatwave frequency during spring and summer over the Central US [*Lee et al*. 2016]. Likewise, *Cheng et al*. [2019] demonstrated a strong soil moisture-temperature coupling in relatively dry regions of the southern Great Plains and the southwestern US whereas a weak coupling that remains unchanged in the moisture-abundant region over the northern and northeastern US in a warmer climate. Overall, these studies outline the importance of land-atmosphere coupling during the heatwaves especially associated with water limited conditions.

Following the Clausius-Clapeyron relationship, at the global scale, the near-surface specific humidity is projected to rise with an increase in air temperature, resulting in no change in relative humidity [*Sherwood et al*., 2010]. A decrease in relative humidity is projected during the hottest days over land [*Fischer and Knutti*, 2013] but these changes in humidity during the heatwaves

need further evaluation. Moreover, commonly used heat stress indices such as wet bulb temperature or apparent temperature often include nonlinear relationships between temperature and relative humidity and are amplified by an increase in temperature even when relative humidity remains unchanged. Therefore, use of such indices restricts our ability to exclusively understand the role of humidity during a heatwave. A few studies have examined these relationships [*Coffel et al*., 2019; *Fischer and Knutti*, 2013; *Raymond et al*., 2017; *Russo et al*., 2017]. *Raymond et al*. [2017] investigated the primary factors driving the wet bulb temperature extremes using National Climate Data Center's Integrated database and found that these extreme days coincide more frequently with the specific humidity extreme days than with the temperature extreme days over the eastern and parts of the western US during 1981 to 2015 period. *Coffel et al*. [2019] depict that the effects of amplified warming on the wet bulb temperature are counter balanced by an enhanced drying, resulting in a dampening of extreme wet bulb temperatures globally. On the other hand, *Dahl et al*. [2019] and *Russo et al*. [2017] project an increase in the maximum apparent temperature and an enhanced human exposure to extreme heat events by the end of 21st century. However, most of these studies are based on the data from General Circulation Model (GCM) form the 5th phase of Coupled Model Intercomparison Project (CMIP5) that conducted simulations at grid spacing not suitable for resolving processes that generate convective precipitation [*Liu et al*., 2017]. Moreover, synoptic conditions suitable for the occurrence of heatwaves (e.g. blocking), are often not very well represented in GCMs, which further limits the representation of heatwaves in GCMs based studies [*Rasmijn et al*., 2018]. Further, the simultaneous changes in dynamic (i.e. atmospheric circulations) and thermodynamic components (such as moisture and heat fluxes) in GCMs also complicate process attribution of projected changes in heatwaves [*Wehrli et al*., 2018]

Given the methodological and modeling limitations in the earlier studies, we employ a pair of high resolution convection-permitting spectrally nudged numerical model simulation [*Liu et al*., 2017] and a methodology that enables the isolation of moisture related impacts on heatwaves to investigate potential changes in the characteristics of dry and humid heatwaves in a warmer climate. Use of two different kinds of heatwaves allows isolation of impacts that moister atmosphere many have in the future climates. Moreover, convection-permitting design of model simulations has the potential to realistic simulate the conditions conducive for the occurrence of heatwaves. Further, the large-scale atmospheric circulations are spectrally nudged towards reanalysis data under both present day and future climate boundary conditions. This setup keeps large-scale conditions almost identical in the two experiments and allows for the reoccurrences of present day real-world atmospheric events (e.g. heatwave) in the future warmer climate. Therefore, this permits a direct comparison of events in the two climates and enables us to isolate the thermodynamically-driven changes in the characteristic of the events.

3.2 Materials and Methods

3.2.1 Model Simulations

We use a pair of 13-year simulations that employ the Weather Research Forecasting (WRF) model Version 3.4.1 [*Skamarock et al*., 2008] over a domain covering the contiguous US and parts of Canada and Mexico. We refer the readers to *Liu et al*. [2017] for a detailed description of the experimental setup. Briefly, each model simulation is conducted at a 4 km horizontal grid spacing with 1360 grid point along the longitude and 1016 grid point along the latitude. The first simulation is a control simulation (WRF-CTRL) that is driven by 6-hourly 0.7^{o} ERA-Interim data [*Dee et al*., 2011] to reproduce the current climate. The second simulation is a climate change experiment that follows the pseudo global warming (PGW) approach (WRF-PGW). The WRF-PGW simulation is

driven by modified ERA-Interim that includes a climate perturbation based on the climate change signal (2071 to 2100 minus 1976 to 2005) from Coupled Model Intercomparison Phase 5 (CMIP5) multimodel ensemble mean under the Representative Concentration Pathway 8.5 (i.e., $CMIP5_{2071–2100}$ minus $CMIP5_{1976–2005}$). The climate change perturbation is applied to horizontal wind fields, geopotential, temperature, specific humidity, sea surface temperature, soil temperature, sea level pressure, and sea ice. The simulations extend from 1 October 2000 to 30 September 2013. These simulations use a spectral nudging approach for the scales on the order of 2000 km and greater, thus allowing the reproduction of present-day specific synoptic weather events in the perturbed simulations. In this study, we use daily-scale maximum temperature (T_{max}), mean specific humidity, soil moisture, and sensible and latent heat flux from these simulations. Further, we calculate evaporative fraction (EF) as the ratio of latent heat flux to total heat flux (latent + sensible) to depict energy partitioning between the two heat fluxes. The use of EF in the analyses is motivated by the reasoning that if the warming during the heatwaves is related to energy partitioning, changes in T_{max} should be correlated with changes in EF during the heatwaves days [*Donat et al*., 2017].

3.2.2 Observational Dataset

We use Parameter-Elevation Regressions on Independent Slopes Model (PRISM) [*Daly et al*., 2008] observations for comparison and model validation. We obtain daily T_{max} and daily mean dew point from the dataset for 2001 to 2013 period. The dataset is available at 4 km horizontal grid spacing over the continental US.

3.2.3 Maximum Apparent Temperature

We use maximum apparent temperature (AT_{max}), also referred to as heat index or “feels like” temperature for human body [*Steadman*, 1979], to account for the role of humidity during

heatwaves. AT_{max} is calculated by applying the Heat Index equation (1) used by National Oceanic and Atmospheric Administration. The equation 1 provides AT_{max} values in degrees Fahrenheit (°F) that are converted to degrees Celsius (°C). Additional adjustments for different range of T_{max} and relative humidity are applied as detailed in the NOAA factsheet

(https://www.wpc.ncep.noaa.gov/html/heatindex_equation.shtml). We calculate relative humidity from daily mean specific humidity and T_{max} for the WRF simulations and from daily mean dew point temperature and T_{max} for the PRISM observations. In order to isolate impacts of temperature and humidity on heatwaves, we substitute AT_{max} values that are below T_{max} with T_{max} values. Minor differences between the magnitudes of AT_{max} and T_{max} during the heatwaves suggest temperature as a driving factor while major differences between the magnitudes of AT_{max} and T_{max} during the heatwaves suggest humidity as a driving factor. *Russo et al*. [2017] follow similar approach to account for the effect of relative humidity during the heatwaves.

$$AT = c_1 + c_2T + c_3R + c_4TR + c_5T^2 + c_6R^2 + c_7T^2R + c_8TR^2 + c_9T^2R^2 \quad (1)$$

Where,

AT is the apparent temperature in °F

T is the temperature in °F

R is the in relative humidity in % between 0 and 100

3.2.4 Compound Heatwave Definition

There are numerous ways to define heatwaves. One of the most common definitions involves use of minimum number of consecutive days above a certain threshold (absolute or percentile based) [*Baldwin et al*., 2019; *Horton et al*., 2016]. However, heatwaves may often continue after break of

a day, therefore, use of consecutive days criteria may underestimate the actual length of a heatwave. Therefore, following *Baldwin et al*. [2019], we use a compound heatwave definition. Using this definition, a period during the summer season (June-July-August, JJA) is considered a heatwave if at least 3 consecutive days cross a given threshold. In our definition, the heatwave continues on the subsequent days after the consecutive days period if only a single day separates the days fulfilling the threshold requirements. We use grid based 95th percentiles of T_{max} (T_{95}) and AT_{max} (AT_{95}), which are based on all the days in 13 summer seasons, as a threshold. We calculate two separate thresholds for WRF-CTRL and WRF-PGW JJA periods respectively. We identify the heatwaves in WRF-CTRL using only WRF-CTRL thresholds (hereafter $CTRL_{CTRL}$) while the heatwaves in WRF-PGW are identified using both the WRF-CTRL thresholds (hereafter PGW_{CTRL}) and the WRF-PGW thresholds (hereafter PGW_{PGW}). The use of two separate thresholds to find heatwaves in WRF-PGW enables the comparison of the characteristics of heatwaves 1) occurring in the warmer climate with respect to the present climate and 2) occurring in the present climate (WRF-CTRL) with respect to present (WRF-CTRL) threshold ($CTRL_{CTRL}$) and occurring in the future climate (PGW) with respect to future (WRF-PGW) threshold (PGW_{PGW}). This allows for a direct comparison between the present and the future heatwaves given that similar heatwave can occur in the two cases (i.e. $CTRL_{CTRL}$ and PGW_{PGW}) . We apply the heatwave definition on T_{max} and AT_{max} using T_{95} and AT_{95} thresholds to identify T_{max} and AT_{max} heatwaves respectively for the $CTRL_{CTRL}$, the PGW_{PGW} and the PGW_{CTRL}.

3.2.5 Heatwave Indices

We use several indices to calculate heatwave characteristics as defined below:

1. Duration of heatwave is defined as the total number of days above the threshold including the break days.

2. Mean amplitude is calculated as the average of T_{max} over the length of heatwave excluding the break days.

3. Mean heatwave intensity is the average difference between T_{max} and T_{95} over the length of heatwave excluding the break days.

4. Number of heatwaves are the total count of heatwaves that occur during a summer season

5. Percentage area under heatwave or extent is defined as the fraction of the total grid points (in percent) in a region where a heatwave is occurring. We aggregate the results over the whole season including all days when a heatwave is present for the scatter and box plots.

3.2.6 Regional Analysis

We focus our analysis primarily on four regions across the US: Southeast, Northeast-Midwest, Central and West, which are marked in Figure 3.1m. These regions are derived from United States Geological Survey (USGS) climate adaptation science center regions. For the ease of presentation, we combine Northwest and Southwest regions and North Central and South Central regions to create West and Central regions respectively. We evaluate changes in the heatwave characteristics such as heat wave indices, humidity and heat fluxes for all the four regions. The significance of change in each characteristics has been tested using two tailed Student's T-test.

3.3 Results

3.3.1 Characteristics of T_{max} versus AT_{max} Heatwaves

We first evaluate the characteristics (duration, intensity, area) of the T_{max} and the AT_{max} heatwaves (Figure 3.1) that occurred during the analyses period (2001 to 2013) over the four geographical regions across the US. Southeast, which is the most humid region in the US, generally shows higher mean percentage area and mean intensity for the AT_{max} heatwaves as compared to the T_{max}

heatwaves with the exception of a few years (Figure 3.1a,e). We illustrate this point by showing a comparison for 2010, when higher percentage of the Southeast was under the AT_{max} heatwave during the summer season when compared with the percentage area under the T_{max} heatwave (Figure 3.1i). This comparison reflects that humidity can also potentially exacerbate geographical footprint of heatwaves. Such an impact of AT_{max} heatwave is further evident from the large average differences between AT_{max} and T_{max} values during 2010 heatwaves (Figure 3.1k,l). Contrarily, 2012 summer was comparatively dry even for the Southeast, with a higher percentage of area under the T_{max} compared to that under the AT_{max} heatwaves and comparatively smaller mean differences between AT_{max} and T_{max} during the heatwaves (Figure 3.1j,m,n).

The Northeast-Midwestern US displays mixed behavior with generally higher mean intensity values for the AT_{max} as compared to the T_{max} heatwaves, whereas the mean percentage area is similar under the AT_{max} and the T_{max} heatwaves (Figure 3.1b,f). On the other hand, the Central (Figure 3.1c-d) and the West regions (Figure 3.1g-h), generally exhibit indistinguishable characteristics for the two kinds of heatwaves, consistent with the predominantly dry summer over these regions with little moisture in the atmosphere. Consequently, the AT_{max} and T_{max} heatwaves show very similar characteristics in terms of mean intensity and mean percentage area under heatwaves, particularly over the Western US. Overall, heatwaves last for up to 8 days, with the majority lasting between 3 to 6 days across the four regions for both T_{max} and AT_{max} (Figure 3.1a-h).

3.3.2 WRF-CTRL versus Observations

We compare the simulated (WRF-CTRL) and the observed (PRISM) characteristics of both the T_{max} and the AT_{max} heatwaves for the analyses period (Figure 3.1a-h, Figure 3.2-3.3). Overall, WRF-CTRL simulates a comparable range for both the mean intensity (Figure 3.1a-d) and the

mean percentage area (Figure 3.1e-f) averaged over the four regions. The spatial patterns for simulated characteristics, including average length, total heatwaves, average amplitude, average intensity of the T_{max} and the AT_{max} heatwaves, and T_{95} and AT_{95}, compare well with the observed characteristics with the exception of a few noticeable biases in their magnitudes (Figure 3.2-3.3). For instance, WRF-CTRL underestimates the number of T_{max} and AT_{max} heatwaves in the western US and the number of AT_{max} heatwaves in the Southeast US and parts of Midwest (Figure 3.2b,g and Figure 3.3b,g). WRF-CTRL also exhibits positive biases in the average amplitudes of both the T_{max} and the AT_{max} heatwaves (Figure 3.2c,h and Figure 3.3c,h) and T_{95} and AT_{95} (Figure 3.2e,h and Figure 3.3e,h), primarily over the Central US and the Southeast. These biases in the magnitude of heatwaves are possibly associated with the prevailing warm season (May to October) biases in these simulations. A near-surface temperature bias of up to 3°C exists in the Central US followed by lower biases of up to 2°C in the Southeast and the Midwest and up to 1°C bias in the Northeast in the WRF model during JJA. The warm bias over the Central US during JJA is attributed to high biases in daytime temperatures [*Liu et al*., 2017].

To further explain the WRF model agreements and differences with the observations using the T_{max} and the AT_{max} heatwaves over the Southeast in 2010 and 2012. In 2010, WRF-CTRL reproduces the percentage area under the T_{max} and the AT_{max} heatwaves suggested by PRISM (Figure 3.1i). Figure 3.1k and 3.1l shows where AT_{max} is larger than T_{max} during 2010, the spatial pattern of which is well simulated. WRF-CTRL slightly underestimates the amplification of AT_{max} relative to T_{max} along the Lower Mississippi (Figure 3.1k,l). During 2012, WRF-CTRL show comparatively larger biases in simulating these characteristics (Figure 3.1 j, m, n). Nevertheless, WRF-CTRL is able to capture the overall spatial and temporal characteristics of the observed heatwaves during 2001-2013.

3.3.3 Changes in the Characteristics of Heatwaves under a Warmer Climate

Changes in the moisture availability during heatwaves can potentially change their characteristics. To investigate such thermodynamic influences, we plot relative humidity against T_{max} during both the T_{max} and the AT_{max} heatwaves in the PRISM observations, and the $CTRL_{CTRL}$, the PGW_{CTRL} and the PGW_{PGW} (Figure 3.4). During the T_{max} heatwaves, relative humidity shows small changes when it is compared between the PGW_{CTRL} and the $CTRL_{CTRL}$ (Figure 3.4a-d). Contrarily, T_{max} in the PGW_{CTRL} heatwaves is projected to be higher than T_{max} in the $CTRL_{CTRL}$ heatwaves. Further, a strong and significant increase in average duration and average number of heatwaves in the PGW_{CTRL} as compared to the $CTRL_{CTRL}$ is projected (Figure 3.5). Consequently, more than half of the summer days over majority of the US (Figure 3.6) qualify as a part of the heatwaves per the $CTRL_{CTRL}$ threshold. Therefore, the characteristics of the heatwaves during the PGW_{CTRL} closely resemble the average summer conditions in the future. Contrarily, the PGW_{PGW}, which represents the future heatwaves defined relative to future climate, includes comparatively stronger heatwaves with T_{max} increasing by an average of at least 5°C in all regions compared to $CTRL_{CTRL}$ (Figure 3.4). Relative humidity during the T_{max} heatwaves in the PGW_{PGW} is projected to decrease in all the regions except the West where relative humidity during the heatwaves is historically low. The strongest decrease is exhibited in the Southeast and the Northeast-Midwest (Figure 3.4a-d). The decrease is relative humidity during the T_{max} heatwaves corresponds with no noticeable changes in the specific humidity (Figure 3.7a-d) and increase in T_{max} (Figure 3.4a-d). On the other hand, during the AT_{max} heatwaves, relative humidity remains largely unchanged, given an increase in both the specific humidity and T_{max} (Figure 3.7e-h) in the PGW_{PGW} as well as the PGW_{CTRL}. This suggests that the humid heatwaves will persist in a future warmer climate, which, together with

increasing T_{max}, greatly increases heat stress during the future AT_{max} heatwaves in all the regions (Figure 3.4e-h).

Given the spectral nudging in these simulations, heatwaves in the CTRL are likely to reappear in the PGW by design, which allows us to directly compare the PGW_{PGW} heatwaves with the corresponding $CTRL_{CTRL}$ heatwaves (Figure 3.6a,c,d,f). Therefore, we calculate the paired differences for each of the 13 years between the characteristics of the PGW_{PGW} and the $CTRL_{CTRL}$ heatwaves. We note that the differences in the duration, the extent and the frequency of the T_{max} and the AT_{max} heatwaves are indistinguishable and not significant between the $CTRL_{CTRL}$ and the PGW_{PGW}. However, we find noticeable differences in the intensities between the $CTRL_{CTRL}$ and the PGW_{PGW} heatwaves that are significant for the Central and the West US during the T_{max} heatwaves and for all the four regions during the AT_{max} heatwaves at 95 percent confidence interval (Figure 3.8).

Further, we analyze thermodynamic changes in the characteristics of heatwaves. For the T_{max} heatwaves in the PGW_{CTRL}, which span more than half of future summer over majority of the US (Figure 3.6 b, e), the latent and the sensible heating do not show robust changes with respect to the $CTRL_{CTRL}$ for all the regions except for small but significant increases in latent heat for the Southeast and the Central and sensible heat in Northeast-Midwest (Figure 3.9a,b). For the T_{max} heatwaves in the PGW_{PGW}, on the other hand, the latent heat decreases while the sensible heat increases with respect to the $CTRL_{CTRL}$ and these changes are significant at 95 percent confidence level for all the four regions (Figure 3.9a,b). This corroborates the results in Figure 3.4, which suggest future summers will see constant or increased relative humidity, but the future heatwaves will see decreases in relative humidity, thus relatively damping heat stress on the hottest days in the future [*Coffel et al.*, 2019]. During the AT_{max} heatwaves, the PGW_{PGW} show small changes in

the latent heat and the sensible heat with respect to the $CTRL_{CTRL}$ for the Southeast and the Northeast-Midwest regions whereas no mean change in heat fluxes are projected in the PGW_{CTRL} heatwaves with respect to the $CTRL_{CTRL}$ (Figure 3.9c,d). These changes in heat fluxes correspond with the changes in soil moisture during the heatwaves (Figure 3.10).

To further establish the role of land-atmosphere interactions in driving variations in the characteristics of heatwaves, we investigate the relationship between changes in the evaporative fraction (EF) and changes in T_{max} during the future heatwaves with respect to the CTRL (Figure 3.9e-l). During the T_{max} heatwaves, changes in EF are negatively correlated with changes in T_{max} over most regions with comparatively high correlation coefficients during both the PGW_{CTRL} and the PGW_{PGW} heatwaves in the Northeast-Midwest and Central US and during the PGW_{CTRL} heatwaves in the West (Figure 3.9e-h). However, for the AT_{max} heatwaves, correlations between EF and T_{max} show mixed signs and small magnitudes except for the West where it shows stronger negative correlations (Figure 3.9i-l). Overall, these changes depict that the amplified warming during T_{max} heatwaves are more closely associated with reduced evaporative cooling portraying land-atmosphere interactions as primary driver during these heatwaves. Conversely, a weak relationship between changes in EF and changes in Tmax during AT_{max} heatwaves indicates a weak land-atmosphere coupling during these heatwaves.

3.4 Conclusion and Discussion

Using a set of convection-permitting spectrally nudged high resolution WRF model simulations, we evaluate changes in the characteristics of T_{max} and AT_{max} heatwaves under a warmer climate. We find a decrease in the relative humidity during the future T_{max} heatwaves and no significant change in the relative humidity during the future AT_{max} heatwaves with reference to the T_{max} and AT_{max} heatwaves in the control period. Given that AT_{max} depends on both relative humidity and

temperature, higher T_{max} during the humid heatwaves drives an increase in AT_{max} as relative humidity remains unchanged. Further, changes in T_{max} during the T_{max} heatwaves are correlated with changes in EF, which reflects a stronger land-atmosphere coupling during these heatwaves. Contrarily, no relationship exists between the changes in EF and the changes in T_{max} during the AT_{max} heatwaves indicating a weak land-atmosphere coupling during such heatwaves.

The findings associated with T_{max} heatwaves, are generally consistent with the findings of previous studies, which associate intensification of temperature extremes with higher partitioning to sensible heat as a result of stronger land-atmosphere coupling under water-limited circumstances in the future climates [*Donat et al*., 2018; *Donat et al*., 2017; *Fischer and Knutti*, 2013; *Lee et al*., 2016; *Teuling et al*., 2010]. Contrarily, in water-abundant circumstances, such as described by AT_{max} heatwaves, the lack of changes in energy flux partitioning yields no amplification of heatwave characteristics beyond the mean warming. This is again consistent with previously reported undetectable changes in land-atmosphere interactions in water-abundant regions [*Cheng et al*., 2019].

Overall, this study provides a new perspective towards the changing characteristics of heatwaves in the future climate. Design of our experiments and analyses allows us to more robustly associate these changes in heatwave characteristics to thermodynamic processes. However, future heatwaves are likely to be affected by changes in atmospheric circulation, although these are typically less robust in model intercomparisons [*Gibson et al*., 2017]. Still, a comprehensive assessment of heat stress hazard needs to take into account both dynamic and thermodynamic factors. This study further highlights the importance of incorporating the effect of humidity in the heatwaves studies. A lack of humidity consideration in these studies can lead to an underestimation of heat stress as perceived by humans resulting in a lower estimate of heatwave impacts on society.

Acknowledgement

This study was supported as part of the Energy Exascale Earth System Model (E3SM) formerly known as Accelerated Climate Modeling for Energy (ACME) project, funded by the U.S. Department of Energy, Office of Science, Office of Biological and Environmental Research. The Advance Study fellowship awarded by Graduate Visitor Program at National Center for Atmospheric Research (NCAR) also provided support for part of the research. Support for data storage and analysis is provided by Computational Information Systems Laboratory at the National Center for Atmospheric Research (NCAR).

Chapter 4

Shift Towards Intense and Widespread Precipitation Events over the United States by Mid Century

Abstract

Recent decades have witnessed an increase in the frequency of precipitation events across the United States that are not only more intense but also spatially widespread. Observations exhibit an increasing trend in precipitation over eastern half of the United States that is largely driven by an increase in daily-scale events that receive at least 12.5 mm precipitation and cover an area over 200 thousand square km. Despite these observed changes in both the spatial and the temporal characteristics of precipitation events, most of the research regarding future changes in precipitation has almost entirely focused on precipitation intensity and/or frequency. Given that prevailing observed trends in precipitation characteristics suggest a need for more comprehensive understanding of precipitation response to increase in radiative forcing, this study investigates potential changes in the characteristic of daily-scale precipitation events both in terms of their intensity and spatial extent in the near-term future. We use high-resolution regionally downscaled climate simulations data that spans 1966 to 2005 in the historical period and 2011 to 2050 in the future period under Representative Concentration Pathway 8.5. We classify precipitation events based on their intensity and spatial extent through a feature continuous labeling algorithm. Our simulated ensemble captures observed changes in the characteristics of precipitation events in the historical period and projects a further increase in the intensity and occurrence of widespread precipitation events by mid 21st century. These changes in the spatial and temporal characteristics of precipitation are attributed to an increase in the occurrence of intense and/or widespread events and a decrease in the occurrence of moderate and small-scale events. We note that such a change in precipitation characteristics is projected to be episodic in nature with extreme years of historical period in terms of frequency of mid to widespread events becoming commonplace in the coming

decades. Overall, this analyses suggest an upwards shift in the intensity as well as spatial extent of precipitation events in response to an unchecked increase in radiative forcing.

4.1 Introduction

Intense, widespread and damaging storms have become more frequent across the United States (hereafter US) in the recent past. National Centers for Environmental Information (NCEI) [2018], database suggests that annual average frequency of multi-billion dollar precipitation related disasters in the 5 most recent years has almost doubled (11.6 events/year) compared to their long term average during 1980-2017 (6 events/year). Some of these events are not only intense but widespread. For example, storm Alberto caused extensive and intense rain resulting in flash flooding and damages in multiple southeastern and northeastern states including Florida and Maryland during May 2018. Similarly, winter storm Harper brought widespread snow across several states in the west, Midwest and northeast causing extensive damage during January 2019. The widespread damages associated with these storms signify the importance of the spatial extent in addition to the intensity of precipitation events in determining the spread of associated risks.

The focus of most studies investigating precipitation characteristics have been on intensity and/or frequency of the events [*Donat et al*., 2016a; *Donat et al*., 2016b] while a complete understanding of spatial characteristics of precipitation is still lacking. These studies find a magnification in number and magnitude of intense precipitation events over the past century [*Dittus et al*., 2015; *Donat et al*., 2016a; *Karl and Knight*, 1998] and are projected to increase further under enhanced radiative forcings in the 21st century [*Donat et al*., 2016b; *Rastogi et al*., 2017]. This intensification of the precipitation events is attributed to enhanced atmospheric water-holding capacity, which is expected to increase exponentially with temperature based on Clausius-Clapeyron equation (6.0-7.5% per degree Celsius warming) [*Min et al*., 2011; *Santer et al*., 2007; *Willett et al*., 2007]. An increase in atmospheric moisture may impact multiple precipitation characteristics including the spatial extent in addition to the frequency and intensity. However, only a limited number of studies

have investigated the spatial characteristics of precipitation mean [*Benestad*, 2018; *Guinard et al*., 2015] and precipitation extreme [*Chang et al*., 2016; *Hamada et al*., 2014; *Wasko et al*., 2016] events. These studies concluded that the areal extent of daily precipitation has either declined or remain unchanged at global as well as at regional scale while the precipitation intensity has increased resulting in more spatially concentrated rainfall over past decade as well as by the end of 21st century [*Benestad*, 2018]. However, these studies are limited by their coarse spatial scales with analysis being conducted at either global scale [*Benestad*, 2018; *Hamada et al*., 2014] or regional scale using coarse horizontal resolution data [*Guinard et al*., 2015] and hence missing the fine scale information. Contrarily, the precipitation distribution shows strong regional variations even within the conterminous US. For example, west and Midwest exhibit high seasonality with precipitation concentrated during winter and spring and spring and summer respectively whereas southeast exhibit low seasonality with precipitation spread throughout the year. The changes in average annual precipitation have also exhibited regional differences resulting in a higher contrast between wet and dry areas [*Ashfaq et al*., 2016]. Similarly, the spatial characteristics of precipitation events are likely to vary across regions depending upon the source of precipitation such as large scale frontal systems, hurricanes or local convective storms and associated changes in these weather patterns [*Kunkel et al*., 2012], but the exact picture is obscure. Therefore, in this study, we aim to understand spatial extent in addition to other characteristics of daily precipitation events at regional scale to better prepare for possible future changes and associated risks. The study brings a new perspective by conducting a comprehensive investigation of multiple precipitation characteristics. We investigate spatial extent in addition to intensity and frequency of precipitation events using precipitation outputs from a high resolution dynamically downscaled climate model projections for historic and future periods [*Ashfaq et al*., 2016]. We specifically focus on large

scale events since these have major impacts on extensive areas across the US and the changing characteristics of these events have important implications for formulating strategies for damage control planning.

4.2 Data and Methodology

4.2.1 Data

This study is based on the analyses of daily simulated and observed precipitation datasets as described below.

4.2.1.1 Observation

Observed daily precipitation is obtained from Parameter-Elevation Regressions on Independent Slopes Model (PRISM) observations [*Daly et al*., 2008] for 1981 to 2005. This dataset is available at 4 km horizontal grid spacing over the continental US.

4.2.1.2 Simulation

Simulated daily precipitation is obtained from a dynamically downscaled and bias corrected ensemble of climate simulations at 4 km. The dynamical downscaled data is taken from Ashfaq et al. (2016), which uses a regional climate model RegCM4 to downscale 11 general circulation models (GCMs) from the Coupled Model Inter-comparison Project Phase 5 (CMIP5) at 18 km horizontal grid spacing over a domain that cover continental US and the parts of Mexico and Canada. The bias correction of daily precipitation from RegCM4 ensemble is based on the methodology described in *Ashfaq et al*. [2010, 2013], which uses quantile mapping to adjust the magnitudes of simulated quantiles with respect to observation while conserving the auto-correlation of the simulated time series. Bias correction is applied on the monthly data and correction factors are disaggregated to the daily values. For the bias correction of precipitation

from RegCM4 ensemble members, we use monthly PRISM observations. Each bias corrected ensemble member covers 1966 to 2005 in the historical period and 2011 to 2050 in the future period under Representative Concentration Pathway 8.5 (RCP 8.5).

4.2.2 Methodology

4.2.2.1 Precipitation Events

We classify precipitation events based on their intensity (I) and spatial extent (S). In the case of intensity, on each day, only those grid points are considered in analysis where daily precipitation is at least 0.5 inch (12.5mm). Further, We divide events in two categories: 1) moderate to heavy event (Total number of events; T_i): when each grid receives at least 0.5 inch (12.5 mm) of daily precipitation on a given day, and 2) heavy event (H_i): when each grid receives at least 1 inch (25 mm) of daily precipitation on a given day. It should be noted that H_i events are a subset of T_i events. Our use of 0.5 inch and 1.0 inch as thresholds for the two categories is based on the fact that for 90% of the US, 65 percent of precipitation is less than 0.5 inch whereas 85 percent of precipitation is less than 1.0 inch (Figure 4.1).

We further divide T_i and H_i events in two categories in terms of their spatial extent. All events with area between 200 to 400 thousand square kilometers (hereafter TSK) are classified as midsize events (M_s), and all events with area >400 TSK are classified as widespread events (W_s). Spatial extent of a precipitation event is calculated through the use of continuous labeling technique. On a given day, all grids where daily precipitation is at least 0.5 inch are labelled. For each labelled grid, 8 neighboring grid points are examined for values above the threshold. This search is continued until the adjacent grids have daily precipitation values below the threshold. The area spanning the connected grids is then calculated to find the spatial extent of the event. The process

is repeated for all H_i events. All precipitation events that do not meet minimum criteria for intensity (0.5 inch) and/or spatial extent (>200 TSK) are not considered in our analyses.

4.2.2.2 Regional Analysis

We consider four regions (southeast, northeast, west and Midwest) in the continental US for regional analyses (Figure 4.2e). Using the centroid of an event, we attempt to assign one of the four regions to each T_i event. Additionally, various characteristics of the precipitation events, including mean, maximum, volume and frequency are calculated for each category (of intensity and size). Precipitation mean and maximum are calculated by taking mean and maximum of precipitation over all the grid point that are part of the daily event. Precipitation volume is calculated as the product of mean precipitation of the daily event multiplied with the total area of that event.

4.3 Results

Observations exhibit an increasing trend in precipitation over most of the upper and lower Midwest and eastern half of US with an increase up to 15 mm per year during 1981 to 2016 period (Figure 4.2a). On the other hand, most of the western US with some exceptions in parts of the Pacific Northwest, exhibit a decreasing trend in precipitation over the same period. It is important to note that the regions that have been experiencing an increase have such a precipitation change dominated by an increase in precipitation from those daily-scale events that receive at least 0.5 inch (12.5 mm) of precipitation (Figure 4.2b). The positive change in precipitation is also driven by an increase in contribution from events that not only exhibit magnitudes greater than 12.5 mm but also a spatial extent of at least 200 thousand square kilometers (Figure 4.2c). This consistency in precipitation increases and increase in the contribution from widespread medium to heavy intensity events suggests that climatic variations may be causing not only an intensification of

precipitation events but also an increase in the spatial extent of those events. It should be noted that these precipitation trends have visibly intensified over last decade as observations show similar but less widespread trends in precipitation for 1981 to 2005 period. We use 1981 to 2005 period to compare trends in the RCM ensemble simulations and observations given that RCM simulations for the historical period only go up to 2005. Interestingly, majority of the RCM ensemble members exhibit changes similar in sign to those in PRISM observations (agreement is shown by stippling) (Figure 4.3). It should be noted that a number of regions in PRISM observations, especially parts of upper and lower Midwest, exhibit a reversal of precipitation trend from negative to positive during last decade, which provides an indication that coming decades may see a further intensification of precipitation increase across the US, driven by more intense and widespread precipitation extremes. Given that intense and widespread precipitation extremes have been responsible for several multi-billion dollar disasters across US, it is imperative to investigate changes in such precipitation characteristics in response to higher levels of radiative forcing that are expected in coming decades.

4.3.1 Historical Characteristics of Precipitation

Historically, US receives up to 200 annual wet days (> 1mm) (Figure 4.4a,b) contributing to over 1500 mm of precipitation (Figure 4.5a,b) during the historical period. These precipitation events exhibit strong regional characteristics across the US The total annual wet days range from less than 20 days in parts of southern California, Arizona and Nevada to up to 150 days in south eastern and up to 200 days in the north western US (Figure 4.4a,b) contributing less than 100 mm over southwestern US to over 1500 mm annual precipitation in the north west and south east (Figure 4.5a,b) respectively. Both the observations and the simulations (RegCM4 ensemble mean; RCM) show southeastern and western US as the hot spots for T_i events receiving around 50% of wet days

in this category (Figure 4.4 c,d). Approximately half of the T_i events fall in the H_i category (Figure 4.6b,d) corresponding to up to 20 -25% of total wet days in the southeast and the west (Figure 4.4 e,f). Moreover, T_i events contribute to up to 80% while H_i events contribute to up to 60% of total precipitation in the two regions (Figure 4.5c-f). Similarly, parts of the upper and lower Midwest experience up to 30 days of T_i events with up to half of them falling in the H_i category (Figure 4.6a-d). In these regions, T_i events correspond to up to 40% of wet days and contribute to up to 80% of total precipitation whereas H_i events correspond to up to 15% of wet days and contribute to up to 45% of total precipitation (Figures 4.4 and 4.5). Seasonally, while both T_i and H_i events are well distributed across the four seasons over the southeast, those are more seasonal in the west (winter to spring) and in the Midwest (spring to summer) (Figures 4.7, 4.8), given the high seasonality of precipitation over these regions [*Ashfaq et al* 2016]. It should be noted that simulated data is not corrected directly at daily scale (see *Methods*), still, it exhibits remarkable skill in the simulation of the spatial and temporal characteristics of precipitation events (Figures 4.4-4.6).

Characteristic of precipitation events in terms of their sizes also vary at regional scale. For instance, majority (up to 20 days) of T_i events in the southeast fall in the W_s category (i.e. >400 TSK) while none of the events in the west fall in this category (Figure 4.7). Conversely, frequency of H_i events is stronger for M_s (up to 6 days) than for the W_s (up to 4 days) over the southeast (Figure 4.8). Over northeast and Midwest, at least half of T_i events occur at M_s or W_s scale whereas fewer H_i events have M_s or W_s scale. Temporally, W_s events over the southeast mostly occur during winter, spring and fall while M_s events are more distributed across all seasons. (Figures 4.7, 4.8).Over northeast and Midwest, both M_s and W_s events are predominant during fall and spring.

More than one third (>33%) of the T_i precipitation over the continental US comes in the form of W_s events. Regionally, the largest contribution from W_s events comes over southeast (>50%)

followed by that over Midwest and northeast where they contribute approximately 32 % and 21.5 % respectively. In contrast, M_s events contribute up to 20% to the annual T_i precipitation over the continental US with regional contribution varying from approximately 25% over northeast, west and Midwest to < 20% over southeast. If only H_i events are considered then M_s events contribute more than W_s events both at regional and at continental scale (Figure 4.6f).

At seasonal scale, precipitation contribution from W_s events to T_i is higher during winter, fall and spring seasons as compared to summer whereas precipitation contribution from M_s events to T_i is relatively more uniform across seasons over southeast and northeast where precipitation does not exhibit much seasonality (Figure 4.9). For Hi events precipitation contribution is dominated during winter, fall and spring irrespective of the spatial scales over the southeast. It should be noted that these characteristics of precipitation events are simulated in the RCM with reasonable accuracy.

4.3.2 Future Changes in the Characteristics of Precipitation

Increase in the radiative forcing will result in a robust increase in the frequency of H_i events both at M_s and W_s scale in the future period (Figure 4.10). With the exception of the parts of southeast, northeast and Pacific Northwest, robust increase in the frequency of T_i events is also witnessed (Figure 4.10a). The decrease in T_i events over southeast and northeast is partly driven by a decline in the occurrence of T_i events at M_s scale events which show small decrease in these regions (Figure 4.10c). It is important to note that both of these regions exhibit one of the strongest increases in H_i events at W_s and M_s, which implies that despite a decrease in T_i events these regions are also experiencing a shift towards heavier and widespread events (Figure 4.10d,f). Seasonally, strongest decline in the occurrence of the M_s events is exhibited during fall season for the H_i events and during fall and winter for T_i events over parts of southeast, northeast and Midwest. Both T_i and H_i

events at W_s scale are projected to increase during winter and spring whereas a decline is projected for T_i at W_s scale during fall. (Figures 4.11, 4.12).

In addition to the changes in the frequency of precipitation events of various intensities and sizes, there is also a change in the relative contribution from these events to the annual precipitation. With the exception of the northeast, W_s events are projected to contribute more to both T_i and H_i precipitation. However, there are regional variations in the characteristics of these contributions. For instance, over the southeast, increase in the contribution from W_s events is at the cost of contribution from M_s events that exhibits a decrease. On the other side, west exhibits increase in the contribution to H_i precipitation regardless of their spatial extent. Similarly, changes in the relative contribution from various categories of precipitation events is opposite in the northeast as it exhibits a decrease in contribution from W_s events (Figure 4.13a). At seasonal scale, fall (winter) exhibits the largest number of declines (increases) in the contribution for different events categories and regions (Figure 4.9). More importantly, we note that increases in the contribution from M_s and W_s events is not distributed uniformly across the years in the future period. When contribution from different categories of precipitation events is ranked across the years and a change is calculated at different quantile levels, we note that increase in the contribution from M_s and W_s events to both H_i and T_i precipitation is more concentrated in the higher quantiles than in lower quantile (Figure 4.13b-c). This suggests that more years are likely to witness higher frequency of larger spatial scale events in the future period.

We summarize changes in various characteristics of precipitation events, including frequency, mean and maximum of magnitude, volume, and mean and maximum of spatial extent using heat maps. In general, precipitation events volume and frequencies are projected to increase for both M_s and W_s events regardless of their intensities. It is interesting to note that when examined across

the regions and precipitation events, mean precipitation (ranging from -1.5 to 5.5%) and mean area (ranging from 0 to 10%) of an event exhibit relatively smaller changes compared to the respective changes in the maximum (ranging from -7 to 19% and -2 to 14.5%). We also note that changes are relatively stronger for W_s events. For instance, changes in precipitation volume in the case of W_s scale T_i events range between 20% to 35% compared to those from M_s scale T_i events that range from 5%, to 23 %. Likewise, change in the frequency of W_s events ranges between 17% to 25% from northeast to southeast compared to change in the frequency of M_s events that ranges between 2% to 22% from southeast to Midwest (Figure 4.13). Overall these results show a shift of precipitation events towards higher intensity and larger scale.

4.4 Summary and Discussion

Overall, RCM_{mean} exhibit exceptional skills in simulating spatial precipitation characteristics over the conterminous US. By 2050, a shift towards heavy and widespread events is projected across the US. While a decrease in the frequency of medium to heavy events is projected over the parts of southeast, northeast and Pacific Northwest, this decline is only partly driven by decrease in midsize and/or midscale events implying a decrease in smaller scale events since frequency of widespread events is increasing over these regions. This decline is predominant in the summer season over northeast and southeast which is dominated by small scale convective storms. Further, a stronger increase is projected in maximum precipitation and extent as compared to their respective means and the increase in precipitation characteristics such as volume, mean and maximum areal extent show stronger increase for widespread scale as compare to midscale events. The projected increase in the frequency and intensity of heavy precipitation events is in accordance with the past studies that have established a rise in the number of destructing weather storms and their precipitation intensities [*Balling and Goodrich*, 2011] [NOAA NCEI 2013].However, the

projected rise in frequency of midscale and widespread scale events and their associated areal extent is contradictory to previous studies that find likely shrinking of precipitation storms [*Benestad*, 2018; *Hamada et al*., 2014] resulting in less severe flood impact than expected with increase precipitation intensity under climate change [*Chang et al*., 2016]. The differences in results can be partly attributed to the difference in methodology and threshold used in this study. Nevertheless, these results provide a different perspective and highlights that while we are likely to witness a rise in frequency of heavy precipitation events, their spatial extent is likely to increase as well.

These heavy and widespread precipitation events cause extensive devastation resulting in tremendous damages to property and claiming numerous lives [NOAA NCEI 2013]. Any increase in the frequency, intensity and spatial extent of such precipitation events will result in extensive societal and economic damages resulting from flooding, wind damage, electric grid failure resulting in widespread loss of power etc. Therefore, accurate estimation of spatial characteristics of precipitation extremes is crucial and have important implications for future emergency planning for damage control and restoration.

Acknowledgement

This research was supported as part of the Energy Exascale Earth System Model (E3SM) formerly known as Accelerated Climate Modeling for Energy (ACME) project, funded by the U.S. Department of Energy, Office of Science, Office of Biological and Environmental Research. The research also received support from the Oak Ridge National Laboratory Project Development funds and Regional and Global Climate Modeling program of the U.S. Department of Energy (DOE) Office of Science. Support for model simulations, data storage and analysis is provided by the Oak Ridge Leadership Computing Facility at the Oak Ridge National Laboratory (ORNL), which is supported by the Office of Science of the U.S. Department of Energy (DOE) under Contract No. DE-AC05-00OR22725.

Chapter 5

Effects of Climate Change on Probable Maximum Precipitation: A Sensitivity Study over the Alabama-Coosa-Tallapoosa River Basin

A version of this manuscript were originally published by Deeksha Rastogi, Shih-Chieh Kao, Moetasim Ashfaq, Rui Mei, Erik D. Kabela, Sudershan Gangrade, Bibi S. Naz, Benjamin L. Preston, Nagendra Singh, and Valentine G. Anantharaj in *Journal of Geophysical Research-Atmospheres*

Rastogi, D., S.-C. Kao, M. Ashfaq, R. Mei, E.D. Kabela, S. Gangrade, B. S. Naz, B. L. Preston, N. Singh, and V.G. Anantharaj (2017), Effects of climate change on probable maximum precipitation: A sensitivity study over the Alabama-Coosa-Tallapoosa River Basin. *Journal of Geophysical Research: Atmospheres*, *122*(9), 4808-4828, doi: /10.1002/2016JD026001.

Abstract

Probable maximum precipitation (PMP), defined as the largest rainfall depth that could physically occur under a series of adverse atmospheric conditions, has been an important design criterion for critical infrastructures such as dams and nuclear power plants. To understand how PMP may respond to projected future climate forcings, we used a physics-based numerical weather simulation model to estimate PMP across various durations and areas over the Alabama-Coosa-Tallapoosa (ACT) river basin in the southeastern United States. Six sets of Weather Research and Forecasting (WRF) model experiments driven by both reanalysis and global climate model projections, with a total of 120 storms, were conducted. The depth-area-duration relationship was derived for each set of WRF simulations and compared with the conventional PMP estimates. Our results showed that PMP driven by projected future climate forcings is higher than 1981–2010 baseline values by around 20% in the 2021–2050 near-future and 44% in the 2071–2100 far-future periods. The additional sensitivity simulations of background air temperature warming also showed an enhancement of PMP, suggesting that atmospheric warming could be one important factor controlling the increase in PMP. In light of the projected increase in precipitation extremes under a warming environment, the reasonableness and role of PMP deserves more in-depth examination.

5.1 Introduction

Probable maximum precipitation (PMP) is defined as "*the greatest depth of precipitation for a given duration meteorologically possible for a design watershed or a given storm area at a particular location at a particular time of year*" [*World Meteorological Organization*, 2009], and it represents the largest rainfall that could physically occur under a series of adverse atmospheric conditions [*Casas et al*., 2008 and 2011; *Douglas and Barros*, 2003; *Schreiner and Riedel*, 1978; *Fernando and Wickramasuriya*, 2011]. Distinguished from the statistically based *T*-year extreme rainfall estimate that associates depth with annual exceedance probability (AEP = 1/*T*; see *Kao and Ganguly*, 2011), PMP is the deterministic upper bound of extreme storms. By definition, PMP is greater than all *T*-year rainfalls and can theoretically be considered as the approximated value when *T* approaches infinity (or AEP approaches 0). The National Research Council [1994] estimates that the return periods of PMP in the United States (hereafter US) are in the range of 10^5 to 10^9 years. As the upper bound of extreme storms, PMP and the resulting probable maximum flood (PMF) are hence used as the strictest design/evaluation standard for highly important energy-water infrastructures that cannot tolerate any failure, such as dams and nuclear power plants [*Prasad et al*., 2011]. Many important facilities such as large schools, hospitals, and waste treatment plants are also purposely located outside of the PMF flood plain [*Biringer et al*., 2013; *Hossain et al*., 2015]. Failure of such critical infrastructure can have serious consequences. For instance, heavy rains in February 2017 caused the failure of Twenty Mile Dam in Nevada, which resulted in flooding and damage to property in the downstream region [*Griggs et al*., 2017].

Although various methods have been developed for estimating PMP [*World Meteorological Organization*, 2009; *Hershfield*, 1961; *Schreiner and Riedel*, 1978; *Hansen*, 1987; *Rakhecha and Singh*, 2009], how to reasonably and objectively estimate PMP remains a challenging task. Clearly,

since PMP is located at the far end of an extreme rainfall distribution, statistically based methods [e.g., *Hershfield*, 1961 and 1965] are limited because of insufficient historic observations (i.e., how can one estimate extreme rainfall with a return period of thousands of years based on decades of data?). Another popular approach is the storm moisture maximization, transposition, and envelopment method that has been used in a series of National Weather Service (NWS) hydrometeorological reports e.g., HMR51 by *Schreiner and Riedel,* [1978]. For a location of interest, this method starts by collecting all historic storms that have occurred in the same region or in regions with similar meteorological settings that allow storm transposition. Based on the hydrostatic and pseudo-adiabatic assumption, a representative surface dew point value (or a sea surface temperature [SST] value if the selected moisture source is on the ocean) is selected as a surrogate to estimate the theoretical precipitable water ($PW_{Control}$) for each storm. A ratio between observed and climatologically maximum air moisture (PW_{PMP}) is then estimated to convert all observed rainfall depths into "moisture maximized" depths to identify the maximum value as PMP. Although this approach is perhaps the most widely used PMP method to date, there are concerns and criticisms regarding the validity of this deterministic approach [*Papalexiou and Koutsoyiannis*, 2006], as well as the large and unsettled uncertainty of PMP estimates [*Micovic et al*., 2015]. *Abbs* [1999] showed that the relation between precipitable water and dew point temperature on the surface is nonlinear. *Chen and Bradley* [2006 and 2007] pointed out that the 12-hour persisting dew point used to calculate maximum precipitable water is not uniquely defined and can be affected by subjective judgment. Above all, it should be noted that this conventional approach is data-driven, and it is challenging to verify whether one has collected a sufficient number of historic storms to confidently derive PMP.

Another important issue is the effects of climate change on PMP. While a warming atmosphere will lead to intensification of *T*-year rainfall extremes [*Kao and Ganguly*, 2011], whether the deterministic storm upper bound will increase correspondingly is yet to be confirmed. Currently, the World Meteorological Organization (WMO, 2009) specifically defines PMP "*under modern meteorological conditions*" and "*with no allowance made for long-term climatic trends*." Nevertheless, in the Chapter 1.8, "PMP and Climate Change," *WMO* [2009] indicated that extreme rainfall events would likely increase in the 21st century (owing to the overall increase in available moisture in a warming climate) and highlighted the need for carefully examination of potential climate change effects on major PMP driving mechanisms such as moisture availability, depth-area curves, storm types, storm efficiency, and generalized rainfall depths.

Recent studies have suggested PMP is likely to increase under a warming environment [*Kunkel et al*., 2013; *Beauchamp et al*., 2013; *Rousseau et al*., 2014; *Stratz and Hossain*, 2014; *Klein et al*., 2016]. Using outputs from multiple Coupled Model Intercomparison Project phase-5 (CMIP5) global climate models (GCMs) with spatial resolution generally greater than 150 km, *Kunkel et al*. [2013] showed that the maximum precipitable water is projected to increase across various GCMs and inferred that PMP is likely to increase correspondingly. This is consistent with *Robinson*'s [2000] finding that the observed hourly dew point (from 178 stations in the conterminous US) increased by approximately 1°/100 year during 1951–1990. Beauchamp et al. (2013), *Rousseau et al*. [2014], and *Rouhani and Leconte* [2016] analyzed the downscaled climate projections at 45-km spatial resolution produced by the Canadian Regional Climate Model (CRCM; Music and Caya, 2007) for the estimation of PMP over watersheds in Quebec. They all followed the same conventional moisture maximization and adjustment approach (used in the NWS hydrometeorological reports) but used more enriched CRCM outputs (e.g., simulated total

precipitable water, atmospheric air temperature, and convective available potential energy [CAPE]) to improve the estimation of $PW_{Control}$, PW_{PMP}, and the maximization factor (PW_{PMP} / $PW_{Control}$). Given the projected increase in future precipitable water, they also suggested a likely increase in PMP. Although further exploration is needed for various types of geographical/meteorological locations at refined spatial resolution, an increase in PMP is highly plausible. Considering the importance of infrastructures designed according to PMP, it is therefore imperative to better understand the effects of climate change on this critical and sensitive design parameter.

The advance of computational power in the recent decade has enabled the enhancement of PMP evaluation using numerical weather forecasting models. Using the European Centre for Medium-Range Weather Forecasts reanalysis (ECMWF) [*Gibson et al*., 1997] as the boundary forcing, *Abbs* [1999] applied the Colorado State University Regional Atmospheric Modeling System (RAMS) [*Pielke et al*., 1992] at 7-km spatial resolution to simulate an extreme storm event in Australia to examine multiple assumptions used in conventional PMP analysis. Driven by the National Center for Environmental Prediction/National Center for Atmospheric Research Reanalysis I (NCEP/NCAR R1) [*Kalnay et al*., 1996], *Ohara et al*. [2011] and *Ishida et al*. [2015] developed a relative humidity moisture maximization method (RHM) and used the fifth-generation mesoscale model (MM5) [*Grell et al*., 1994] to simulate PMP for the American River Watershed in California. The atmospheric boundary condition shifting method (ABCS) [*Ishida et al*., 2014] were subsequently developed to estimate PMP for other watersheds in California. *Tan* [2010] and *Chen and Hossain* [2016] utilized multiple reanalysis data sets and the Weather Research and Forecasting model (WRF) [*Skamarock et al*., 2008] to reconstruct major historic storms to estimate PMP. To test how land use/land cover (LULC) change may influence extreme precipitation,

Woldemichael et al. [2012] and [2014] also conducted numerical weather simulations using RAMS under various LULC scenarios. Despite the high modeling uncertainty of rainfall depth, these numerical weather prediction models can provide a theoretically sound framework for a process-based understanding of climate change effects on extreme rainfall and PMP.

To understand the effects of climate change on PMP, in this study we developed PMP estimates using a numerical weather forecasting model and evaluated the sensitivity of PMP estimates to projected future climate conditions over the Alabama-Coosa-Tallapoosa (ACT) river basin in the southeastern US. The WRF model, driven by both reanalysis and GCM projections, was used to downscale and simulate a total of 120 extreme storms at 3-km horizontal grid spacing. The RHM method [*Ohara et al*., 2011; *Ishida et al*., 2015] was then used to simulate moisture-maximized storms and derive PMP across various durations and areas. The changes in the PMP depth-area-duration (DAD) relationship were also quantified and discussed. Our main objectives are to test whether PMPs will increase in the future (through two different modeling strategies, one using GCM-based climate change simulations as the boundary forcing and the other increasing the background air temperature in the reanalysis-driven control historic simulations directly) and to examine whether the changes in total precipitable water are consistent with the changes in PMP depth. This paper is structured as follows: Section 2 introduces the overall method, data, and study area; Section 3 illustrates and describes results; and Section 4 presents discussion and the conclusion of this study.

5.2 Methods

5.2.1 Study Area

The study area covers the ACT river basin, which spans across the northeastern and eastern-central regions of Alabama, northwestern Georgia, and parts of Tennessee, including the Coosa,

Tallapoosa, and Alabama rivers and their tributaries. The upper Coosa River Basin lies in Georgia and overlaps with the Atlanta metropolitan area. The total ACT drainage area is around 59,050 km^2 (22,800 mi^2). The topography is relatively flat, with an average elevation of around 197 m (646 ft, calculated from National Elevation Dataset) [*Gesch et al*., 2002]. Precipitation occurs in all seasons, and the total annual precipitation is around 1,364 mm (53.7 inch). Major winter storms are large-scale frontal systems formed when warm, moist air masses from the Gulf of Mexico meet with cold, drier air masses from the north [*US Army Corps of Engineers*, 2013]. The storms that occur in summer or early fall are usually regional-scale convective systems with high rainfall intensities over smaller areas. Occasionally, tropical storms or hurricanes also bring significant amounts of precipitation during summer and fall. There are more than 16 large dams in the ACT, mainly owned and operated by the US Army Corps of Engineers or the Alabama Power Company.

5.2.2 Data and Storm Selection

To identify and select major historic extreme storms in the ACT river basin, two widely used gridded precipitation data sets were used: (1) the 4-km spatial resolution Oregon State University PRISM [*Daly et al*., 2008] and (2) the 1-km spatial resolution Oak Ridge National Laboratory (ORNL) Daymet [*Thornton et al*., 1997]. Based on comprehensive rain gauge observations across the conterminous US (e.g., NWS Cooperative Observer Network and others), both products used various gridding and orographic correction methodologies to form refined daily rainfall fields for various research needs. Given the consideration of orographic effects, both products should be able to provide more reliable spatial rainfall distributions than the conventionally used Thiessen polygon approach [*Thiessen*, 1911]. Another useful data source is NCEP Stage IV precipitation [*Lin*, 2011] that assimilates both radar and gauge observations (e.g., used by *Gagnon et al*. [2012] to estimate the parameters of a rainfall spatial disaggregation model). While we did not use NCEP

Stage IV in this study, mainly because the data are available only since 2002, we note that PRISM has also incorporated radar measurements in its daily precipitation estimates since 2002.

For both data sets, complete daily precipitation data from 1981–2011 were collected. Focusing on the study domain from 30.5°N to 35.5°N and from 84.5°W to 88.5°W, the 3-day (72-hour) precipitation total was calculated to identify the largest 30 storms (Table 5.1) with the highest rainfall depth during 1981–2011 for WRF control simulation and model verification.

5.2.3 Numerical Weather Simulation

We used WRF version 3.6 [*Skamarock et al*., 2008] to simulate extreme storms for the ACT river basin. The WRF model, a successor of MM5, is a mesoscale numerical weather simulation model designed for both atmospheric research and operational forecasting. In addition, WRF has been widely used to dynamically downscale coarser-resolution GCM signals into finer-resolution climate projections that can better represent fine-scale meteorological processes such as precipitation extremes [*Caldwell et al*., 2009; *Lo et al*., 2008; *Rasmussen et al*., 2014; *Yoo et al*., 2016]. In this study, we used a two-way nested WRF domain at 9-km and 3-km horizontal spacing, with 110 by 122 and 184 by 220 grids in each domain, respectively (Figure 5.1) and 45 vertical levels to conduct the simulation. All precipitation and moisture analyses were conducted on a study domain (from 30.5°N to 35.5°N and from 84.5°W to 88.5°W) that is slightly smaller than the WRF inner simulation domain but covers the entire ACT river basin.

To reconstruct the historic storms listed in Table 5.1, the Climate Forecast System Reanalysis I (CFSR) [*Saha et al*., 2010] was used as the boundary forcing to drive WRF. CFSR is a coupled atmosphere-ocean–land surface–sea ice system with high horizontal (38 km) as well as vertical spacing (64 pressure levels). The presence of both ocean and sea ice makes CFSR more comprehensive and accurate than earlier NCEP global reanalysis products [*Saha et al*., 2010]. The

CFSR was chosen over the North American Regional Reanalysis (NARR) [*Mesinger et al*., 2006] because (1) the 2009 version of the Noah land-surface model is used in the CFSR versus the 2003 version in the NARR; and (2) *Mo et al*. [2011] found NARR did not partition evapotranspiration and runoff well, leading to very high values of evapotranspiration and low values of runoff across the entire US. Although biases exist in the CFSR, they are mainly contained in the western US and Great Plains [*Mo et al*., 2011].

For each storm, a 5-day simulation was conducted that started 1 day before and ended 1 day after the identified 3-day period. To determine a most appropriate cumulus parameterization and cloud microphysics scheme for the selected storms in the ACT river basin, we tested six different combinations of parameterization schemes by changing cumulus and microphysics parameterizations (Table 5.2) [*Grell and Dévényi*, 2002; *Hong et al*., 2004; *Kain and Fritsch* 1990, 1993; *Kain*, 2004; *Lin et al*., 1983; *Thompson et al*., 2004] for each historic storm. The parameterization scheme that yielded the best model performance in the study area (discussed in Section 3.2) was then used for further climate downscaling and PMP simulation. In addition to the control simulation, we tested the sensitivity of PMP to background temperature adding 1°C and 2°C on the control simulation.

To explore how PMP may change in projected future climate conditions, we used the Community Climate System Model version 4 (CCSM4) [*Gent et al*., 2011] r6i1p1 ensemble member under the RCP8.5 emission scenario from the CMIP5 archive as the boundary forcing to drive WRF. Following the same storm selection procedures described in Section 2.2, we calculated the 3-day (72-hour) precipitation total over the study area and selected extreme storms from the baseline (BL: 1981–2010), near-future (F1: 2021–2050), and far-future (F2: 2071–2100) periods.

The selected CCSM4 storms and their maximum 72-hour domain average precipitation within a 5-day simulation period are reported in Table 5.3.

Overall, six sets of WRF experiments with a total of 120 storms were set up for this study:

(1) **CFSR-WRF-CT**: Control simulation that includes 30 storms driven by 1981–2011 CFSR reanalysis

(2) **CFSR-WRF-T1**: CFSR-WRF-CT with 1°C increase in air temperature

(3) **CFSR-WRF-T2**: CFSR-WRF-CT with 2°C increase in air temperature

(4) **CCSM4-WRF-BL**: Baseline simulation that includes 30 storms driven by both 1981–2005 in historical period and 2006–2010 in future period under RCP8.5 scenario of CCSM4 experiments

(5) **CCSM4-WRF-F1**: Near-future simulation that includes 30 storms driven by 2021–2050 CCSM4 projection under RCP8.5 scenario

(6) **CCSM4-WRF-F2**: Far-future simulation that includes 30 storms driven by 2071–2100 CCSM4 projection under RCP 8.5 scenario

We selected RCP8.5 because it is closest to the observed emissions during 2006–2010 [*Peters et al*., 2013] and because we wanted to test how the 2071–2100 far-future PMP may change in the highest emission concentration pathway in CMIP5. The numerical simulations were conducted on the Titan supercomputer maintained by the Oak Ridge Leadership Computing Facility at ORNL, used more than 3 million computational hours, and generated over 10 terabytes of hourly WRF output to support further analysis and applications.

5.2.4 PMP Simulation and Analysis

To simulate PMP, the RHM method [*Ohara et al*., 2011; *Ishida et al*., 2015] was used. For each storm, the moisture of boundary forcing was maximized by modifying the relative humidity in the boundary conditions to 100% (i.e., fully saturated), which raised the atmospheric moisture to its theoretical maximum levels (governed by air temperature, pressure, and other meteorologic variables). A 5-day WRF simulation was then repeated for each extreme storm with maximized moisture to simulate PMP. Although not directly comparable to the conventional HMR approach [*Schreiner and Riedel*, 1978], the concept of moisture maximization is somewhat similar. For each storm within the HMR, the total precipitable water was estimated by an observed surface dew point (or SST). At the same location where (and the same timing when) the dew point was selected, the historic maximum dew point was looked up to calculate the climatically maximum total precipitable water. However, the biggest difference is that the HMR used the ratio between original and maximized total precipitable water (PW_{PMP} / $PW_{Control}$) to linearly re-scale the observed rainfall depth ($Depth_{Control}$) to form the PMP ($Depth_{PMP}$), whereas RHM simulated PMP using a numerical weather forecasting model directly.

We selected RHM in this study given that the total precipitable water is known to be the most important variable controlling PMP (especially for the long-duration rainfall depth). However, there are other factors affecting PMP that may not be satisfied by RHM. For instance, we noticed that CAPE does not always increase in PMP simulations when RHM is used, suggesting that there could be further room to maximize convective rainfall depth through modification of temperature, wind, and other meteorological variables that may positively influence CAPE. Such inconsistency in CAPE response also suggests the need to explore further meteorologically justifiable adjustment strategies to simulate PMP. The recent work by *Rouhani and Leconte* [2016] explored using CAPE

as a filtering criterion to select more defensible annual maximum precipitable water values to estimate 100-year return period precipitable water as PW_{PMP}. Another example is the ABCS method [*Ishida et al.*, 2014] that was designed for regions where extreme precipitation is associated with sustained moisture inflow through atmospheric rivers (e.g., western US). Overall, given that the RHM method does not require the subjective judgment of a surface representative dew point location and value (for comparison with the conventional HMR method), it can be methodologically more objective. We conducted PMP simulations for all of the 120 storms reported in Section 2.3.

To evaluate the simulated PMP, we summarized the DAD relationship of each storm. Within the study domain and for the entire 5-day period, we used elliptic moving windows with different combinations of eccentricity and orientation (i.e., to mimic the shapes of synthetic storms generated by HMR52; Hansen et al., 1982) to thoroughly search the maximum precipitation under 6-, 12-, 24-, 48-, and 72-hour storm durations and 25.9-, 518-, 2,590-, 12,900-, 25,900-, and 51,800-km^2 (10-, 200-, 1,000-, 5,000-, 10,000-, and 20,000-mi^2) storm areas. The use of elliptic spatio-temporal moving windows allowed us to examine the simulated precipitation extremes across various storm durations, areas and orientations, not limited to a particular temporal and spatial scale. By identifying the maximum simulated value across all combinations of durations and areas, we constructed the DAD of the PMP. We computed the PMP DADs separately for CFSR-WRF-CT, CFSR-WRF-T1, CFSR-WRF-T2, CCSM4-WRF-BL, CCSM4-WRF-F1, and CCSM4-WRF-F2. The conventional HMR51 PMP values at the same durations and areas from *Schreiner and Riedel* [1978] for the ACT river basin (33°N, 86°E) were also looked up for comparison.

5.3 Results

5.3.1 Representativeness of the Selected GCM Projection

Given that only one climate simulation was used in this study, we started by evaluating the representativeness of the selected GCM (CCSM4-r6i1p1) simulation within the CMIP5 ensemble. Focusing on annual precipitation and temperature averaged across the entire outer WRF domain (Figure 5.1), a scatter plot (Figure 5.2) was prepared for a total of 70 CMIP5 simulations (from 30 GCMs) for three time periods, including a 1981–2010 baseline (1981–2005 from historical and 2006–2010 from RCP8.5 scenario for future simulations) and two future periods, 2021–2050 and 2071–2100, under the RCP8.5 scenario. Dashed lines denote the ensemble median of 70 CMIP5 simulations, and blue squares indicate the selected CCSM4-r6i1p1.

In terms of the multi-model median, the annual temperature was projected to increase by ~1°C from the baseline to the near future, and by ~4°C from the baseline to the far future. The change in mean annual precipitation was less obvious, around a 2.7% increase from the baseline to the near future and a 3.6% increase from the baseline to the far future. Nevertheless, note that the change in precipitation extremes could be more significant than the mean annual precipitation, which has been suggested by multiple studies [*Kharin et al*., 2013; *O'Gorman*, 2015]. In all three periods, CCSM4-r6i1p1 lay very close to the median lines for both annual precipitation and temperature, suggesting that the selected model should not provide overly wet/dry or hot/cold projections compared with other CMIP5 members.

We further compared the synoptic features of CCSM4-r6i1p1 air temperature, specific humidity, and wind (i.e., three main boundary forcing variables for WRF simulation) with both the CFSR and the CMIP5 multi-model mean in Figures 5.3 and 5.4. For winter months (Figure 5.3—December, January, and February) and summer months (Figure 5.4—June, July, and August), the

1981–2005 average zonal temperature (°C) and specific humidity (kg/kg) were illustrated at various pressure levels. In addition, the 500-mb wind direction and magnitude were illustrated for the entire US. As a result of the available data at the time of analyses, 46 GCMs were used for air temperature, 37 GCMs were used for specific humidity and 31 GCMs were used for winds from CMIP5 archives. During winter, CFSR is generally warmer, wetter, and has stronger jetstream over the study area compared with CCSM4. During summer, CCSM4 near-surface humidity in the southern domain is higher than in CFSR, but magnitudes are more comparable in the case of temperature and winds. Overall, the synoptic features of CCSM4 are very close to those of the CMIP5 multi-model mean, and also remain largely similar to CFSR.

The skillfulness of CCSM4 over the US has also been reported in earlier studies. For the southeastern US, *Rupp* [2016] recently conducted a thorough model evaluation of 41 CMIP5 GCMs using multiple observational datasets and 42 diagnostic metrics, including mean/seasonal temperature and precipitation, strength of El Niño Southern Oscillation (ENSO) teleconnection, and other metrics. In his evaluation, CCSM4 is among the most highly ranked models. In addition, *Liu et al*. [2013] investigated the Atlantic warm pool (AWP) variability in the historical run of 19 CMIP5 GCMs and concluded that CCSM4 is among the best three CMIP5 models in simulating AWP SST variability. Moreover, CCSM4 is also used in *Yoo et al*. [2016] as the boundary forcings in WRF to simulate and study tropical cyclones. Given the relatively better performance of CCSM4 within all CMIP5 models, we believe that CCSM4 is a reasonable choice for the purpose of this study.

5.3.2 WRF Tuning and Validation

For the selected 30 extreme storms during 1981–2011, we tested various parameterization schemes (Table 5.2). Given that our focus is on rainfall depth, we computed the simulated 3-day domain

average precipitation (mm) for each storm and compared it with both Daymet/PRISM observations (Table 5.1). The coefficient of determination (R^2) and root mean square error (RMSE) between the simulated and observed storms were also calculated. Overall, the results suggested that the P1 parameter set (Grell-Devenyi cumulus parameterization and *Lin et al*. [1983] cloud microphysics scheme) provided the most similar results to both the Daymet and the PRISM observations with the highest R^2 (Daymet: 0.725; PRISM: 0.704) and lowest RMSE (Daymet: 19 mm; PRISM: 19 mm).

For further insight into the influence of different schemes, the example of an August 24–26, 2008, storm is illustrated in Figure 5.5. Rainfall depth seemed to be more sensitive to cumulus parameterization than to the cloud microphysics scheme. The rainfall depth simulated by the Grell-Devenyi ensemble scheme (118–126 mm, panels a–c) was much closer to Daymet (121 mm) and PRSIM (117 mm) than the depth simulated by the Kain-Fritsch scheme (164–174 mm, panel d–f). The influence of the cloud microphysics scheme seemed to be less obvious; in it, all storms patterns remained largely similar (panels a–c) with smaller variation in local storm cells and rainfall depth. While the Thompson scheme (panel c) was more representative for the illustrated storm in Figure 5.5, overall, the Lin et al. (1983) scheme (P1) worked better across all storms (Table 5.1).

Although one set of parameterization schemes may not be the best for all types of storms under different meteorological and climatic conditions, it is important to identify a generally suitable set from all of the reanalysis-driven control storms to increase the objectivity of the process. In particular, in conducting a GCM-driven WRF simulation, one would be unable to adjust the parameterization specifically for each storm (i.e., given the lack of a ground truth such as PRISM/Daymet). The evaluation focused on rainfall depth (Table 5.1) could help us identify and exclude inappropriate choices that could lead to unreasonable estimates of extreme rainfall and

PMP. Given the overall better performance of P1, we hence used it for all CCSM4-WRF PMP simulations.

5.3.3 PMP during Historic Period

The maximum rainfall depth under various durations and areas for each set of simulated storms was summarized; PMPs of different durations are illustrated in Figure 5.6, and PMPs with different areas are illustrated in Figure 5.7. For comparison, the conventional HMR51 estimates are also included.

In comparing HMR51 with CFSR-WRF-CT, it can be seen that CFSR-WRF-CT is generally larger than HMR51 (Figure 5.6). The most similar results are shown for a 6-hour duration (Figure 5.6a). As the duration increased, the simulated PMP started to diverge from HMR51 (Figures 5.6 and 5.7). For example, at 25.9 km^2 (10 mi^2) and 6 hours, the PMP for HMR51 and CFSR-WRF-CT was 787 mm and 821 mm, respectively (4% difference, Figure 5.6a and 5.7a). When the duration was increased to 72 hours, their values became 1295 mm and 1979 mm, respectively (53% difference, Figure 5.6e and 5.7a). At 518,00 km^2 (20,000 mi^2) and 6 hours, the PMP for HMR51 and CFSR-WRF-CT was 127 mm and 158 mm, respectively (17% difference, Figure 5.6a and 5.7a). The values at 72 hours became 483 mm and 908 mm, respectively (88% difference, Figure 5.6e and 5.7a). Overall, the PMP levels simulated by WRF using CFSR forcing were higher than HMR51 in all 30 combinations of durations and areas examined in this study.

We further evaluated the change in precipitable water versus the change in rainfall depth due to the RHM moisture maximization (Figure 5.8). For the 30 CFSR-WRF-CT storms, we calculated the 72-hour average precipitable water over the study domain from the original simulations ($PW_{Control}$) and the ones with RHM (PW_{PMP}). Correspondingly, we also calculated the maximum 6- and 72-hour and 25.9- and 51,800-km^2 (10- and 20,000-mi^2) rainfall depths from the original

simulation ($Depth_{Control}$) and the ones using RHM ($Depth_{PMP}$). The ratios PW_{PMP} / $PW_{Control}$, indicating the change in average precipitable water, and $Depth_{PMP}$ / $Depth_{Control}$, indicating the change in rainfall depth, are illustrated in various scatter plots (Figure 5.8). Conventionally, in HMR51, the PW_{PMP} / $PW_{Control}$ ratio is calculated using storm representative and climatology maximum dew point values. HMR51 further assumes PW_{PMP} / $PW_{Control}$ = $Depth_{PMP}$ / $Depth_{Control}$ to calculate $Depth_{PMP}$ across various durations and areas.

Overall, with a few exceptions, both precipitable water and rainfall depth increased as a result of the influence of RHM. However, these two ratios had a large spread and did not fall near the 1:1 line. The range of PW_{PMP} / $PW_{Control}$ was from 1.2 to 2, but the range of $Depth_{PMP}$ / $Depth_{Control}$ was from 0.7 to 5.5. While conventionally it is assumed that the change in precipitable water will be consistent with the change in rainfall depth (because of moisture maximization), such a relationship was not presented in these simulations. Again, we found a large difference in the scatter patterns between a shorter precipitation duration ($Depth_{PMP}$ / $Depth_{Control}$ average 1.64 and 1.48 in panels a and c) and a longer duration ($Depth_{PMP}$ / $Depth_{Control}$ average 2.18 and 2.41 in panels b and d). This could be one explanation for the difference in the longer-duration HMR51 and simulated PMP values in Figures 5.5 and 5.7. In a few cases, particularly for a shorter duration (panels a and b) or smaller area (panels a and c), the change in moisture could actually alter the original storm structure and lead to a slightly decreased maximum rainfall depth (i.e., $Depth_{PMP}$ / $Depth_{Control} < 1$).

Another explanation for the larger difference at longer duration can be associated with how the storm precipitable water (i.e., $PW_{Control}$) is estimated in the conventional approach. For each historic storm, the air moisture trajectory before the occurrence of a storm was identified (from wind and pressure charts) to select weather stations with representative dew point observations to estimate

$PW_{Control}$ (see *Chen and Bradley* [2006 and 2007] for a more in-depth discussion). Conceptually speaking, the conventional approach provides a snapshot of the total precipitable water right before a storm occurs, but not in or during the development of a storm. Therefore, while the conventional approach can be a reasonable approximation for a shorter-duration storm, the method, by design, is unable to capture the variation in total precipitable water of a longer-duration storm (because of front movement, local moisture recycling, and other meteorological moisture exchange mechanisms that occur after a storm starts). The RHM method, on the other hand, is designed to maximize the total precipitable water during the entire storm period of a numerical simulation and hence can lead to a more significant increase in precipitation over a longer duration. We note that *Beauchamp et al*. [2013] and *Rousseau et al*. [2014] define $PW_{Control}$ for an event as the maximum of all instantaneous precipitable water values simulated over a regional climate model (CRCM) tile during and before the start of an event (2 days earlier in *Beauchamp et al*. [2013] and 18 hours earlier in *Rousseau et al*. [2014]); hence, the concepts are more similar to the conventional approach. Although the implications of these differences deserve further exploration and thinking, it is our opinion that the simulated PMP should be closer to the spirit of a theoretical PMP (i.e., the meteorological upper bound—if exists).

Despite this difference in longer-duration events, the similarity of the PMP between the conventional and simulated estimates at a 6-hour duration is in fact intriguing. Note that the methods used in HMR51 and in this study are totally different, so the similarity suggests a possible convergence of two approaches. The shorter-duration PMP is particularly important for the evaluation of the local intense precipitation-driven flash flooding risk for critical infrastructures such as nuclear power plants.

5.3.4 Effects of Climate Change on PMP

In this section, we investigate the effects of climate change on PMP, comparing the DAD relationship of the CCSM4-driven simulations for the baseline and future periods. The simulated PMP during three time periods (1981–2010, 2021–2050, and 2071–2100) is also illustrated in Figures 5.6 and 5.7.

In comparing CCSM4-WRF-BL with CFSR-WRF-CT, it can be seen that CFSR-driven PMP exceeds CCSM4-driven PMP in most durations and areas (3 of 30 cases) during the baseline period, suggesting that CCSM4 forcing could potentially lead to an underestimation of PMP (under the assumptions that the CCSM4 modeling bias will consistently persist and that CFSR-driven PMP is more accurate). In comparing CCSM4-WRF-BL with CCSM4-WRF-F1 and CCSM4-WRF-F2, it can be seen that, moving further into the future, PMP estimates increase (under the RCP8.5 scenario). For instance, at a 6-hour duration and over a 25.9-km^2 (10-mi^2) area, the simulated PMP for the CCSM4 baseline, near-future, and far-future periods was 731 mm, 761 mm, and 960 mm, respectively (Figure 5.6). The largest increase during the F1 period was found to be 39% for a 6-hour duration and over a 12,950-km^2 (5,000-mi^2) area, and the largest increase during the F2 period was found to be 63% at a 12-hour duration and over a 2,590-km^2 (1,000-mi^2) area, compared with the baseline period. Average increases of 20% and 44% in PMP were found for the 30 combinations of duration and area for the F1 and F2 periods, respectively. PMP estimates for the far future were higher than those for the near future at all durations and areas, suggesting a consistent increase in PMP with an increase in radiative forcing during the 21st century. Overall, our results suggest the PMP is projected to increase in the future, which is consistent with findings from previous studies [*Kunkel et al*., 2013; *Beauchamp et al*., 2013; *Rousseau et al*., 2014; *Rouhani and Leconte*, 2016].

Although there are various factors in future climate projections that could affect extreme precipitation and PMP (e.g., circulation and wind patterns), it is generally understood that atmospheric warming plays a critical role. Enhanced radiative forcing under a changing climate will cause a rise in atmospheric temperature. A warmer atmosphere is in turn capable of holding more moisture, following the Clausius-Clapeyron relationship [see *Lenderink and van Meijgaard*, 2008; *Berg et al*., 2013; *Loriaux et al*., 2016 for further discussion]. These factors may lead to an intensification in the hydrological cycle due to increased precipitable water and evapotranspiration, resulting in more intense extreme precipitation events.

To test the sensitivity of PMP to background air temperature warming, we conducted further CFSR-WRF-T1 and CFSR-WRF-T2 simulations. These simulations used the same setup as CFSR-WRF-CT, but increased the CFSR air temperature by 1°C and 2°C. Combined with RHM, this temperature adjustment led to an increase in total precipitable water in the WRF boundary forcings. The simulated PMP is included in Figures 5.6 and 5.7 for comparison. As expected, the higher background temperatures led to increased rainfall depth in nearly all cases, especially over longer durations (Figure 5.6d and 5.6e). The higher temperatures may also have led to stronger evapotranspiration and a faster local moisture recycling rate that also increased the PMP. Once again, the increase in total precipitable water and PMP is nonlinear and exhibits a large variation. This is similar to what we observed and discussed in regard to Figure 5.8, in which the change in precipitable water could be inconsistent with the change in rainfall depth, and the original storm structure could be altered by a change in the moisture pattern.

It is interesting that the influence of temperature increases on PMP at 6 hours was very minor. It suggests that, although the precipitable water increased (as a result of increasing temperature), the maximum precipitation at 6 hours seemed to reach a maximum. It is also interesting to note that,

although the projected future PMPs (CCSM4-F1 and CCSM4-F2) were larger than those in temperature sensitivity runs (CFSR-T1 and CFSR-T2) in smaller storm areas (Figures 5.7a–c), the order was reversed in larger storm areas (Figures 5.7d–f). As mentioned, although we think atmospheric warming is one important factor affecting the projected future PMP values, there are also other factors affecting PMP that cannot be fully explained by temperature. Further exploration is hence needed for other modeling choices and other study areas to better understand the effects of climate change on PMP.

5.3.5 Uncertainties in PMP Simulation

Finally, we examined the uncertainty across all simulated storms in Figure 5.9. We used a box plot to illustrate the maximum, minimum, and three quartiles of RHM rainfall depth among the 30 storms in each set of simulations across various storm durations and areas. As a reminder, since our objective was to identify the maximum possible rainfall, the maximum value in each set of simulations (i.e., each box) was what we identified as the PMP.

Taking a 6-hour storm duration as an example, it can be seen that the CFSR-driven RHM rainfall depth range is 43–236 mm for 10,000 mi^2 (Figure 5.9–e1) and 150–821 mm for 10 mi^2 (Figure 5.9–a1). For a 72-hour duration, the CFSR-driven RHM depth range is 95–1083 mm for 10,000 mi^2 (Figure 5.9–e5) and 392–1979 mm for 10 mi^2 (Figure 5.9–a5). CCSM4-driven RHM depths at 6-hour duration during the baseline period range from 39–157 mm for 10,000 mi^2 (Figure 5.9–e1) and from 157–731 mm for 10 mi^2 (Figure 5.9–a1). For a 72-hour duration, the CCSM4-driven RHM depth range is 160–930 mm for 10,000 mi^2 (Figure 5.9–e5) and 254–1843 mm for 10 mi^2 (Figure 5.9–a5), lower than the CFSR-driven control estimates. The range of depths simulated for the future periods of CCSM4 is higher than in the baseline period. At a 6-hour duration, the CCSM4-driven RHM depth range is 65–198 mm and 78–225 mm for the two future periods for

10,000 mi² (Figure 5.9–e1), and 223–761 mm and 239–959 mm for 10 mi² (Figure 5.9–a1). Moreover, at 72 hours, CCSM4-driven RHM depth range is 154–961 mm and 216–1,450 mm for the two future periods under 10,000 mi² (Figure 5.9–e5), and 288–2,298 mm and 544–2,800 mm for 10 mi² (Figure 5.9–a5).

A key observation from Figure 5.9 is the high uncertainty associated with the simulated RHM depths. Although the moisture was maximized in all storms, there was still a large spread in the simulated rainfall depth, again suggesting moisture is not the only necessary factor controlling PMP. In addition, not a single storm produced a maximum depth across all durations and areas (not shown here). Therefore, it is imperative to incorporate a large set of storms in order to more reliably identify the PMP (e.g., such as the work done by Rousseau et al. [2014] and Rouhani and Leconte [2016]). In other words, the PMP values could be underestimated if only a few storms are considered (which seems to be true for both conventional analysis and the numerical simulation used in this study). However, incorporating more storms will bring a large computational burden to the already extensive simulation of each extreme storm. Additional modeling considerations—such as different reanalysis and climatic forcings, weather forecasting models, domains and parameterizations—would all increase the dimension of complexity in the simulation of PMP.

Another note concerns the use of maximum value to derive PMP. Although from the medians of these simulated storms we may conclude that CCSM4-F2 is always greater than CCSM4-F1 and then CCSM4-BL, the maximum value itself may sometimes be misleading. For instance, in Figure 5.9–d5, the maximum CCSM4-BL value is slightly greater than the maximum CCSM4-F1, opposite the case for the median values. This is in fact a limitation to which the maximum is prone in the existence of statistical outliers. Nevertheless, unless we are willing to move forward from

pure deterministic thinking in PMP evaluation and application (i.e., focusing only on maximum rainfall and flood events), such challenges are likely to linger.

5.4 Conclusion and Discussion

In this study, a physics-based numerical weather simulation model was used to estimate PMP over the ACT river basin and to understand the effects of climate change on these estimates. The WRF model was tuned by six different combinations of cumulus and microphysics parameterization schemes for 30 historical storms and evaluated against gridded observations from Daymet and PRISM. Six sets of WRF experiments with a total of 120 storms were set up to estimate the PMP and its sensitivity associated with changes in climate forcings and atmospheric warming. Overall, our results suggest that RHM-based PMP [*Ohara et al*., 2011; *Ishida et al*., 2015] is projected to increase in the future climate condition. This finding is related with the following factors for further consideration.

(1) We used a numerical weather simulation approach to estimate PMP using RHM method that is different from the conventional data-driven storm moisture maximization, transposition, and envelopment method [*Schreiner and Riedel*, 1978]. Although both methods provided comparable estimates at a 6-hour duration (Figure 5.6a), the numerically simulated PMP was found to be much larger than the conventional PMP at a longer storm duration. We believe one main reason is related to the use of a storm representative dew point in the conventional approach that cannot capture the total precipitable water of a longer-duration storm. The RHM method was designed to maximize the total precipitable water during the entire storm period and hence could lead to a more significant increase in precipitation in a longer-duration storm.

(2) Although it is generally assumed that the change in precipitable water (due to moisture maximization) is around the same scale as the change in rainfall depth, such a relationship was not

found in this study. The applicability of this linear relationship was also questioned by *Abbs* [1999]. In addition to the large uncertainty across different storms (Figure 5.8), the change in rainfall depth was generally smaller in shorter-duration and larger in longer-duration storms. This can be another explanation for the difference between longer-duration HMR51 and simulated PMP (Figures 5.6 and 5.7).

(3) Despite the differences between the CFSR- and CCSM4-driven PMP estimates during the baseline period, the overall results can be used to understand the effects of climate change on PMP estimates by comparing the PMP estimated under different sets of CCSM4-driven experiments. PMPs for the two future periods were found to be higher than the baseline PMP, indicating an increase in PMP under enhanced radiative forcing. The additional sensitivity simulations of background air temperature warming also showed an enhancement of PMP, suggesting that atmospheric warming could be an important factor controlling the increase in PMP. Therefore, like the intensification of *T*-year rainfall extremes [*Kao and Ganguly*, 2011], an increase in the deterministic PMP storm upper bound in a warming environment is also likely. Further studies to identify other controlling factors (e.g., circulation and moisture patterns) would be useful to enhance our understanding of PMP.

(4) Given the large uncertainty across different storms, durations, and areas (Figure 5.9), we showed that a large number of storms are required to identify the most critical combinations of meteorological conditions that may lead to the formation of the PMP. A PMP value based on few storms is hence at risk of underestimation. However, it is challenging to confirm whether one has already collected a sufficient number of storms to construct the PMP. Additional modeling considerations, such as different reanalysis forcings, models, domains, and parameterizations, can also be tested to identify the maximum PMP forming conditions.

(5) The PMP estimates generated in this study are used by *Gangrade et al*. [2019 and 2018] to run a distributed hydrology model followed by a flood model to generate probable maximum flood estimates and conduct flood assessment studies.

Finally, while we have shown that the simulated PMP is projected to increase under future climate conditions, how to further strengthen the simulated PMP for engineering applications deserves further thinking. For instance, although the maximum moisture condition (RHM) is plausible in the coastal region, it may not be reasonable to adopt it for an inland desert (where moisture is less likely to reach). Various types of modeling uncertainties—from driving forcings, the ability of numerical models to simulate rainfall depth, and approaches to achieving PMP rainfall, to the selection of extreme storms—all need to be better understood before a simulated PMP can be developed for application. On the other hand, given the lack of improvement in conventional PMP methods and estimates, inaction is not an option. As shown in this and previous studies, various fundamental assumptions regarding the conventional PMP method (e.g., using change in precipitable water to infer change of rainfall depth) have been found to be questionable and need to be reexamined. Philosophically speaking, the biggest issue for estimating PMP for engineering practice is perhaps its deterministic nature. Given the goal of maxima searching, there is hardly any room to consider risk and likelihood. The community should start assigning uncertainties to PMP estimates [*Micovic et al*., 2015] or seek an alternative method, such as probabilistic flood hazard assessment [*US Nuclear Regulatory Commission*, 2013]. In light of the projected increases in precipitation extremes under a warming environment, the reasonableness and role of PMP deserves a more in-depth examination.

Acknowledgement

This study was funded by the Laboratory Directed Research and Development Program of ORNL and used resources of the Oak Ridge Leadership Computing Facility at ORNL. The authors are employees of UT-Battelle, LLC, under contract DE-AC05-00OR22725 with DOE. Accordingly, the U.S. Government retains and the publisher, by accepting the article for publication, acknowledges that the U.S. Government retains a non-exclusive, paid-up, irrevocable, world-wide license to publish or reproduce the published form of this manuscript, or allow others to do so, for U.S. Government purposes.

Chapter 6

Summary and Outlook

This doctoral dissertation consists of multiple studies that use high-resolution process-based physical models' simulations to thoroughly investigate the anthropogenic hydroclimatic changes, which can severely impact human systems. In the first study, we develop empirical relationships between the observed climate and household energy demand. Subsequently, we apply these relationships on a high-resolution climate data [*Ashfaq et al*., 2016] to evaluate anthropogenically driven changes in the residential energy demand over the US by mid 21st century. We find that more intense and prolonged warm conditions will drive an increase in the electricity demand due to higher space cooling requirement, while shorter and milder winter will decrease natural gas usage for space heating [*Rastogi et al*., 2019]. In the second study, we use a pair of high-resolution numerical model simulations, which constraint large-scale atmospheric circulations [*Liu et al*., 2017] to evaluate the characteristics of dry and humid heatwaves in the control and the pseudo climate warming scenarios. A comparison of dry and humid heatwaves characteristics in their respective climates shows a decrease in relative humidity during the dry heatwaves whereas undetectable changes in relative humidity during the humid heat waves. Further, we find strong land-atmosphere coupling during the dry heatwaves and a weak coupling during the humid heatwaves. This study highlights the importance of incorporating humidity in heatwave identification, which can further enhance physiological heat stress, and poses severe risks to human health. In the third study, we investigate spatial and temporal characteristics of daily precipitation events and their projected changes by the mid 21st century in response to increase in radiative forcing. We apply a continuous component labeling technique and intensity thresholds to categorize precipitation events in terms of their spatial extent and magnitude. We find a shift towards more intense and spatially widespread events under warmer conditions in the future climates. In the fourth study, we evaluate PMP, which is used as a design criteria for highly

important infrastructures, and sensitivity of its magnitudes to changes in temperature and moisture in the future climates. We employ WRF model to downscale and maximize three-day extreme precipitation events in the boundary forcing of a reanalysis data and a GCM. We compare simulated PMP with the conventional estimates in the historical period and further evaluate the projected changes in PMP in a warmer and moister climate. We find 20% and 44% increase in PMP in the near-future (2021 to 2050) and far-future (2071 to 2100) with reference to the historical period (1981 to 2010) [*Rastogi et al*., 2017]. These results have strong implications for energy-water infrastructures.

Overall, this doctoral dissertation develops rigorous analytical frameworks, which can be used as a benchmark to assess various aspects of hydroclimate responses to anthropogenically driven changes. It provides important scientific insights that can be used to improve our understanding of risks associated with the changes in extreme temperature and precipitation events on human settlements, energy, and other important infrastructures. In the case of research related with future energy demand, most of the previous studies have used spatially aggregated scales that are not relevant for decision making. This research work addresses this limitation by using a relatively fine spatial scale climate data, which accounts for important regional to local scale differences that are present in the energy demand projections. Further, we find a shift in the net energy demand, used for residential space heating and cooling, from natural gas towards electricity. The decrease in natural gas demand primarily occurs during the winter months, which has important implications for natural gas prices and underground gas storage. The increase in electricity demand has important implications for greenhouse gas emissions depending upon the source of additional electricity generation and highlights that strategic planning is required to meet the energy demands across the US in the coming decades in economically feasible and environmental friendly ways.

Further, the previous studies that focus on evaluating heatwave characteristics mostly do not incorporate the effect of humidity. Moreover, these studies utilize coarse resolution GCM outputs that are unable to fully capture atmospheric blocking patterns, which commonly drive such extreme heat events. In order to improve on these limitations, this dissertation employs high resolution numerical outputs and incorporates humidity in the identification of heatwaves with a goal to improve the accuracy of heat stress estimation as perceived by humans.

We also note that US has received an increasing number of intense and widespread storms over the past decades. More recently, storm Alberto caused extensive and intense rain that resulted in flash flooding and damages in many eastern states during May 2018. Similarly, winter storm Harper brought widespread snow across multiple states in the west, Midwest and northeast, causing extensive damage during January 2019. Given that these storms often cause widespread damage, it is importance to investigate that how the spatial extent of precipitation events may vary in the coming decades. To this end, part of this dissertation work investigates changes in the temporal and spatial characteristics of daily-scale precipitation events in the coming decades. We find a potential increase in the intensity as well as the spatial extent of daily-scale precipitation events in the future projections, which has the potential to exacerbate the risk associated with the occurrences of such storms. Therefore, this research work highlights the need of better planning for damage control in this regard.

Lastly, this research highlights the need of better ways for more accurate estimation of PMP scale precipitation event that, if occur, can bring unprecedented damage to critical infrastructures. In recent past, the precipitation associated with hurricane Harvey exceeded conventional PMP estimates for certain durations and areas [*Kao et al*. 2019]. The storm flooded a chemical and processing facility and disabled the cooling equipment resulting in overheating, igniting fire and

shutting the plant *[Sebastian et al, 2017]*, among numerous other damages. Such occurrences highlight the importance of updating conventional estimates particularly in the context of projected increase in the intensity and extent of future storms. Through model based synthetic PMP experiments, this research has been able to show that PMP magnitudes will be higher in warmer and moister future climate. The PMP estimates generated in this work have been used by other scientists to investigate the changes in the occurrences probable maximum floods and their implications for critical infrastructure such as hydropower plants *[Gangrade et al*. 2019 and 2018*]*. The PMP modeling framework, developed in this dissertation, can be used as a benchmark to further improve the physical model based calculations of PMP for better understanding of human system vulnerabilities due to climate changes.

In the end, we also want to highlight a number of caveats in this research that are related with modeling choices, analytical methodologies and data limitations. All of modeling outputs are based on dynamical downscaling of coarse scale boundary forcing, which in some case have been statistically bias corrected. We have not investigated the uncertainties arising from the use of dynamical downscaling and the choice of correction procedure. We have also used empirical models whose limitations were not thoroughly tested. Similarly, moisture maximization at the boundaries is one way to achieve PMP estimates but there is a need to test other modeling approaches to understand the robustness of these estimates. Also, these PMP estimates were only based on a single reanalysis data and a single GCM and there is a need to conduct similar analyses using multiple reanalysis and GCMs to reduce modeling uncertainties. Some uncertainties also arise due to observed data limitations such as coarse scale energy demand data which we hope will reduce with time as observations are becoming more refined both spatially and temporally. Better observations should reduce the issues related with fine-scale disaggregation, which are presently

visible across state boundaries in our energy use estimates. Similarly, high temporal observations related with peak hour energy demand should enable better understanding of changes in climate extremes on household energy use. Lastly, all use cases in this dissertation are over the US. While we hope that analytical and modeling frameworks should be useful for similar studies over other geographical regions, transferability of these techniques to other regions requires rigorous evaluation. Nonetheless, the frameworks developed in this dissertation provide a foundation to motivate future work in these areas.

References

Allen, M. R., S. J. Fernandez, J. S. Fu, and M. M. Olama (2016), Impacts of climate change on sub-regional electricity demand and distribution in the southern United States, *Nat Energy*, *1*, doi:Artn 1610310.1038/Nenergy.2016.103.

Amato, A. D., M. Ruth, P. Kirshen, and J. Horwitz (2005), Regional energy demand responses to climate change: Methodology and application to the Commonwealth of Massachusetts, *Climatic Change*, *71*(1-2), 175-201.

Ashfaq, M., D. Rastogi, R. Mei, S. C. Kao, S. Gangrade, B. S. Naz, and D. Touma (2016), High-resolution ensemble projections of near-term regional climate over the continental United States, *J Geophys Res-Atmos*, *121*(17), 9943-9963, doi:10.1002/2016jd025285.

Ashfaq, M., S. Ghosh, S. C. Kao, L. C. Bowling, P. Mote, D. Touma, S. A. Rauscher, and N. S. Diffenbaugh (2013), Near-term acceleration of hydroclimatic change in the western US, *J Geophys Res-Atmos*, *118*(19), 10676-10693, doi:10.1002/jgrd.50816.

Ashfaq, M., L. C. Bowling, K. Cherkauer, J. S. Pal, and N. S. Diffenbaugh (2010), Influence of climate model biases and daily-scale temperature and precipitation events on hydrological impacts assessment: A case study of the United States, *J Geophys Res-Atmos*, *115*, doi:Artn D1411610.1029/2009jd012965.

Ashfaq, M., Y. Shi, W. W. Tung, R. J. Trapp, X. J. Gao, J. S. Pal, and N. S. Diffenbaugh (2009), Suppression of south Asian summer monsoon precipitation in the 21st century, *Geophys Res Lett*, *36*(1).

Auffhammer, M., P. Baylis, and C. H. Hausman (2017), Climate change is projected to have severe impacts on the frequency and intensity of peak electricity demand across the United States, *P Natl Acad Sci USA*, *114*(8), 1886-1891, doi:10.1073/pnas.1613193114.

Auffhammer, M., and A. Aroonruengsawat (2011), Simulating the impacts of climate change, prices and population on California's residential electricity consumption, *Climatic Change*, *109 (Supplement 1)*, 191-210, doi:10.1007/s10584-011-0299-y.

Baldwin, J. W., J. B. Dessy, G. A. Vecchi, and M. Oppenheimer (2019), Temporally Compound Heat Wave Events and Global Warming: An Emerging Hazard, *Earths Future*, *7*(4), 411-427, doi:10.1029/2018ef000989.

Balling, R. C., and G. B. Goodrich (2011), Spatial analysis of variations in precipitation intensity in the USA, *Theor Appl Climatol*, *104*(3-4), 415-421.

Barnett, T. P., et al. (2008), Human-induced changes in the hydrology of the western United States, *Science*, *319*(5866), 1080-1083, doi:10.1126/science.1152538.

Bartos, M. D., and M. V. Chester (2015), Impacts of climate change on electric power supply in the Western United States, *Nat Clim Change*, *5*(8), 748-752, doi:10.1038/Nclimate2648.

Benestad, R. E. (2018), Implications of a decrease in the precipitation area for the past and the future, *Environmental Research Letters*, *13*(4), 044022.

Bobb, J. F., R. D. Peng, M. L. Bell, and F. Dominici (2014), Heat-Related Mortality and Adaptation to Heat in the United States, *Environ Health Persp*, *122*(8), 811-816, doi:10.1289/ehp.1307392.

Burke, M., S. M. Hsiang, and E. Miguel (2015), Global non-linear effect of temperature on economic production, *Nature*, *527*(7577), 235-+, doi:10.1038/nature15725.

Calzadilla, A., K. Rehdanz, R. Betts, P. Falloon, A. Wiltshire, and R. S. J. Tol (2013), Climate change impacts on global agriculture, *Climatic Change*, *120*(1-2), 357-374, doi:10.1007/s10584-013-0822-4.

Census, U. S. (2016), Census U.S. Intercensal County Population Data, 1970-2014, in *http://www.nber.org/data/census-intercensal-county-population.html*, edited.

Chang, W., M. L. Stein, J. L. Wang, V. R. Kotamarthi, and E. J. Moyer (2016), Changes in Spatiotemporal Precipitation Patterns in Changing Climate Conditions, *J Climate*, *29*(23), 8355-8376.

Cheng, L., M. Hoerling, Z. Liu, and J. Eischeid (2019), Physical Understanding of Human-Induced Changes in US Hot Droughts Using Equilibrium Climate Simulations, *J Climate*, *32*(14), 4431-4443.

Coffel, E. D., R. M. Horton, J. M. Winter, and J. S. Mankin (2019), Nonlinear increases in extreme temperatures paradoxically dampen increases in extreme humid-heat, *Environ Res Lett*, *14*(8), doi:ARTN 08400310.1088/1748-9326/ab28b7.

Coffel, E. D., T. R. Thompson, and R. M. Horton (2017), The impacts of rising temperatures on aircraft takeoff performance, *Climatic Change*, *144*(2), 381-388.

Dahl, K., R. Licker, J. T. Abatzoglou, and J. Declet-Barreto (2019), Increased frequency of and population exposure to extreme heat index days in the United States during the 21st century, *Environmental Research Communications*, *1*(7), 075002.

Daly, C., M. Halbleib, J. I. Smith, W. P. Gibson, M. K. Doggett, G. H. Taylor, J. Curtis, and P. P. Pasteris (2008), Physiographically sensitive mapping of climatological temperature and precipitation across the conterminous United States, *Int J Climatol*, *28*(15), 2031-2064, doi:10.1002/joc.1688.

Day, T. (2006), Degree-days: Theory and Application, *The Chartered Institution of Building Services Engineers 222 Balham High Road, London SW12 9BS*.

Dee, D. P., et al. (2011), The ERA-Interim reanalysis: configuration and performance of the data assimilation system, *Q J Roy Meteor Soc*, *137*(656), 553-597, doi:10.1002/qj.828.

Diffenbaugh, N. S., et al. (2017), Quantifying the influence of global warming on unprecedented extreme climate events, *P Natl Acad Sci USA*, *114*(19), 4881-4886, doi:10.1073/pnas.1618082114.

Diffenbaugh, N. S., J. S. Pal, R. J. Trapp, and F. Giorgi (2005), Fine-scale processes regulate the response of extreme events to global climate change, *P Natl Acad Sci USA*, *102*(44), 15774-15778, doi:10.1073/pnas.0506042102.

Dirks, J. A., W. J. Gorrissen, J. H. Hathaway, D. C. Skorski, M. J. Scott, T. C. Pulsipher, M. Y. Huang, Y. Liu, and J. S. Rice (2015), Impacts of climate change on energy consumption and peak demand in buildings: A detailed regional approach, *Energy*, *79*, 20-32, doi:10.1016/j.energy.2014.08.081.

Dittus, A. J., D. J. Karoly, S. C. Lewis, and L. V. Alexander (2015), A Multiregion Assessment of Observed Changes in the Areal Extent of Temperature and Precipitation Extremes, *J Climate*, *28*(23), 9206-9220, doi:10.1175/Jcli-D-14-00753.1.

Donat, M. G., A. J. Pitman, and O. Angélil (2018), Understanding and Reducing Future Uncertainty in Midlatitude Daily Heat Extremes Via Land Surface Feedback Constraints, *Geophys Res Lett*, *45*(19), 10,627-610,636.

Donat, M. G., A. J. Pitman, and S. I. Seneviratne (2017), Regional warming of hot extremes accelerated by surface energy fluxes, *Geophys Res Lett*, *44*(13), 7011-7019, doi:10.1002/2017gl073733.

Donat, M. G., L. V. Alexander, N. Herold, and A. J. Dittus (2016a), Temperature and precipitation extremes in century-long gridded observations, reanalyses, and atmospheric model simulations, *J Geophys Res-Atmos*, *121*(19), 11174-11189.

Donat, M. G., A. L. Lowry, L. V. Alexander, P. A. O'Gorman, and N. Maher (2016b), More extreme precipitation in the world's dry and wet regions, *Nat Clim Change*, *6*(5), 508-+, doi:10.1038/Nclimate2941.

Dosio, A., L. Mentaschi, E. M. Fischer, and K. Wyser (2018), Extreme heat waves under 1.5 degrees C and 2 degrees C global warming, *Environ Res Lett*, *13*(5), doi:ARTN 054006 10.1088/1748-9326/aab827.

Driscoll, J. C., and A. C. Kraay (1998), Consistent Covariance Matrix Estimation with Spatially Dependent Panel Data, *Review of Economics and Statistics 80*(549–560).

Dunne, J. P., R. J. Stouffer, and J. G. John (2013), Reductions in labour capacity from heat stress under climate warming, *Nat Clim Change*, *3*(6), 563-566, doi:10.1038/Nclimate1827.

EIA, U. S. (2016a), Natural gas consumption by end use, in *http://www.eia.gov/dnav/ng/ng_cons_sum_a_EPG0_vrs_mmcf_m.htm*, edited.

EIA, U. S. (2016b), Retail sales of electricity to ultimate customers, in *https://www.eia.gov/electricity/data.php#sales*, edited.

EPA, U. S. (2010), ICLUS Tools and Datasets (Version 1.3 & 1.3.1). edited, U.S. Environmental Protection Agency, Washington, DC.

EPA, U. S. (2014), Climate change indicators in the United States., *Third Edition*(EPA 430-R-14-004.).

Fischer, E. M., and R. Knutti (2013), Robust projections of combined humidity and temperature extremes, *Nat Clim Change*, *3*(2), 126-130, doi:10.1038/Nclimate1682.

Fischer, E. M., S. I. Seneviratne, P. L. Vidale, D. Luthi, and C. Schar (2007), Soil moisture - Atmosphere interactions during the 2003 European summer heat wave, *J Climate*, *20*(20), 5081-5099, doi:10.1175/Jcli4288.1.

Gangrade, S., S.-C. Kao, T. T. Dullo, A. J. Kalyanapu, and B. L. Preston, 2019: Ensemble-based Flood Vulnerability Assessment for Probable Maximum Flood in a Changing Environment. *Journal of Hydrology*.

Gangrade, S., S. C. Kao, B. S. Naz, D. Rastogi, M. Ashfaq, N. Singh, and B. L. Preston, 2018: Sensitivity of Probable Maximum Flood in a Changing Environment. *Water Resour Res*, **54,** 3913-3936.

Gibson, P. B., A. J. Pitman, R. Lorenz, and S. E. Perkins-Kirkpatrick (2017), The role of circulation and land surface conditions in current and future Australian heat waves, *J Climate*, *30*(24), 9933-9948.

Glaser, J., et al. (2016), Climate Change and the Emergent Epidemic of CKD from Heat Stress in Rural Communities: The Case for Heat Stress Nephropathy, *Clin J Am Soc Nephro*, *11*(8), 1472-1483, doi:10.2215/Cjn.13841215.

Guinard, K., A. Mailhot, and D. Caya (2015), Projected changes in characteristics of precipitation spatial structures over North America, *Int J Climatol*, *35*(4), 596-612, doi:10.1002/joc.4006.

Hamada, A., Y. Murayama, and Y. N. Takayabu (2014), Regional Characteristics of Extreme Rainfall Extracted from TRMM PR Measurements, *J Climate*, *27*(21), 8151-8169, doi:10.1175/Jcli-D-14-00107.1.

Horton, R. M., J. S. Mankin, C. Lesk, E. Coffel, and C. Raymond (2016), A Review of Recent Advances in Research on Extreme Heat Events, *Curr Clim Change Rep*, *2*(4), 242-259.

Huang, J. H., and K. R. Gurney (2017), Impact of climate change on U.S. building energy demand: Financial implications for consumers and energy suppliers, *Energ Buildings*, *139*, 747-754.

Huang, J. H., and K. R. Gurney (2016), The variation of climate change impact on building energy consumption to building type and spatiotemporal scale, *Energy*, *111*, 137-153, doi:10.1016/j.energy.2016.05.118.

Jaeger, C. C., J. Krause, A. Haas, R. Klein, and K. Hasselmann (2008), A method for computing the fraction of attributable risk related to climate damages, *Risk Anal*, *28*(4), 815-823, doi:10.1111/j.1539-6924.2008.01070.x.

Kao, S.-C., S. T. DeNeale, and D. B. Watson (2019), Hurricane Harvey Highlights: Need to Assess the Adequacy of Probable Maximum Precipitation Estimation Methods, *Journal of Hydrologic Engineering*, *24*(4), 05019005.

Karl, T. R., and R. W. Knight (1998), Secular trends of precipitation amount, frequency, and intensity in the United States, *B Am Meteorol Soc*, *79*(2), 231-241.

King, A. D., M. G. Donat, S. C. Lewis, B. J. Henley, D. M. Mitchell, P. A. Stott, E. M. Fischer, and D. J. Karoly (2018), Reduced heat exposure by limiting global warming to 1.5 degrees C, *Nat Clim Change*, *8*(7), 549-551, doi:10.1038/s41558-018-0191-0.

Kunkel, K. E., D. R. Easterling, D. A. R. Kristvich, B. Gleason, L. Stoecker, and R. Smith (2012), Meteorological Causes of the Secular Variations in Observed Extreme Precipitation Events for the Conterminous United States, *J Hydrometeorol*, *13*(3), 1131-1141.

Lee, E., R. Bieda, J. Shanmugasundaram, and H. B. Richter (2016), Land surface and atmospheric conditions associated with heat waves over the Chickasaw Nation in the South Central United States, *J Geophys Res-Atmos*, *121*(11), 6284-6298.

Lesk, C., P. Rowhani, and N. Ramankutty (2016), Influence of extreme weather disasters on global crop production, *Nature*, *529*(7584), 84-+, doi:10.1038/nature16467.

Liu, C. H., et al. (2017), Continental-scale convection-permitting modeling of the current and future climate of North America, *Clim Dynam*, *49*(1-2), 71-95, doi:10.1007/s00382-016-3327-9.

Lobell, D. B., G. L. Hammer, G. McLean, C. Messina, M. J. Roberts, and W. Schlenker (2013), The critical role of extreme heat for maize production in the United States, *Nat Clim Change*, *3*(5), 497-501, doi:10.1038/Nclimate1832.

Lobell, D. B., A. Torney, and C. B. Field (2011), Climate extremes in California agriculture, *Climatic Change*, *109*, 355-363, doi:10.1007/s10584-011-0304-5.

Lorenz, R., E. B. Jaeger, and S. I. Seneviratne (2010), Persistence of heat waves and its link to soil moisture memory, *Geophys Res Lett*, *37*.

McFarland, J., et al. (2015), Impacts of rising air temperatures and emissions mitigation on electricity demand and supply in the United States: a multi-model comparison (vol 131, pg 111, 2015), *Climatic Change*, *132*(4), 739-739, doi:10.1007/s10584-015-1452-9.

Melillo, J. M., Terese (T.C.) Richmond and G. W. Yohe (2014), Highlights of Climate Change Impacts in the United States: The Third National Climate Assessment.*Rep*. *148*, U.S. Global Change Research Program.

Min, S. K., X. B. Zhang, F. W. Zwiers, and G. C. Hegerl (2011), Human contribution to more-intense precipitation extremes, *Nature*, *470*(7334), 378-381.

Miralles, D. G., A. J. Teuling, C. C. van Heerwaarden, and J. V. G. de Arellano (2014), Mega-heatwave temperatures due to combined soil desiccation and atmospheric heat accumulation, *Nat Geosci*, *7*(5), 345-349, doi:10.1038/Ngeo2141.

Perkins, S. E., L. V. Alexander, and J. R. Nairn (2012), Increasing frequency, intensity and duration of observed global heatwaves and warm spells, *Geophys Res Lett*, *39*, doi:Artn L20714 10.1029/2012gl053361.

NOAA, N. (2018), State of the Climate: Global Climate Report for Annual 2017*Rep*.

NOAA National Centers for Environmental Information (NCEI) U.S. Billion-Dollar Weather and Climate Disasters (2018). https://www.ncdc.noaa.gov/billions/

NOAA National Centers for Environmental Information, State of the Climate: Global Climate Report for Annual 2017, published online January 2018, retrieved on August 2, 2018 from https://www.ncdc.noaa.gov/sotc/global/201713.

Petri, Y., and K. Caldeira (2015), Impacts of global warming on residential heating and cooling degree-days in the United States, *Scientific Reports*, *5*, doi:ARTN 1242710.1038/srep12427.

Raghavendra, A., A. G. Dai, S. M. Milrad, and S. R. Cloutier-Bisbee (2019), Floridian heatwaves and extreme precipitation: future climate projections, *Clim Dynam*, *52*(1-2), 495-508, doi:10.1007/s00382-018-4148-9.

Rasmijn, L. M., G. van der Schrier, R. Bintanja, J. Barkmeijer, A. Sterl, and W. Hazeleger (2018), Future equivalent of 2010 Russian heatwave intensified by weakening soil moisture constraints, *Nat Clim Change*, *8*(5), 381-+, doi:10.1038/s41558-018-0114-0.

Rastogi, D., J. S. Holladay, K. J. Evans, B. Preston, and M. Ashfaq (2019), Shift in seasonal climate patterns likely to impact residential energy consumption in the United States, *Environ Res Lett*, *14*(7), doi:ARTN 074006 10.1088/1748-9326/ab22d2.

Rastogi, D., S. C. Kao, M. Ashfaq, R. Mei, E. D. Kabela, S. Gangrade, B. S. Naz, B. L. Preston, N. Singh, and V. G. Anantharaj (2017), Effects of climate change on probable maximum

precipitation: A sensitivity study over the Alabama-Coosa-Tallapoosa River Basin, *J Geophys Res-Atmos*, *122*(9), 4808-4828.

Raymond, C., D. Singh, and R. M. Horton (2017), Spatiotemporal Patterns and Synoptics of Extreme Wet-Bulb Temperature in the Contiguous United States, *J Geophys Res-Atmos*, *122*(24), 13108-13124. RECS Residential Energy Consumption Survey (RECS) – U.S. Energy Information Administration., edited.

Russo, S., J. Sillmann, and A. Sterl (2017), Humid heat waves at different warming levels, *Sci Rep-Uk*, *7*, doi:ARTN 7477 10.1038/s41598-017-07536-7.

Rosenzweig, C., F. N. Tubiello, R. Goldberg, E. Mills, and J. Bloomfield (2002), Increased crop damage in the US from excess precipitation under climate change, *Global Environ Chang*, *12*(3), 197-202, doi:Pii S0959-3780(02)00008-0Doi 10.1016/S0959-3780(02)00008-0.

Ruth, M., and A. C. Lin (2006), Regional energy demand and adaptations to climate change: Methodology and application to the state of Maryland, USA, *Energ Policy*, *34*(17), 2820-2833.

Sailor, D. J., and J. R. Munoz (1997), Sensitivity of electricity and natural gas consumption to climate in the USA - Methodology and results for eight states, *Energy*, *22*(10), 987-998.

Santer, B. D., et al. (2007), Identification of human-induced changes in atmospheric moisture content, *P Natl Acad Sci USA*, *104*(39), 15248-15253.

Schoetter, R., J. Cattiaux, and H. Douville (2015), Changes of western European heat wave characteristics projected by the CMIP5 ensemble, *Clim Dynam*, *45*(5-6), 1601-1616, doi:10.1007/s00382-014-2434-8.

Sebastian, A., K. Lendering, B. Kothuis, A. Brand, S. N. Jonkman, P. van Gelder, M. Godfroij, B. Kolen, M. Comes, and S. Lhermitte (2017), Hurricane Harvey Report: A fact-finding effort in the direct aftermath of Hurricane Harvey in the Greater Houston Region.

Sherwood, S. C., and M. Huber (2010), An adaptability limit to climate change due to heat stress, *P Natl Acad Sci USA*, *107*(21), 9552-9555, doi:10.1073/pnas.0913352107.

Sherwood, S. C., W. Ingram, Y. Tsushima, M. Satoh, M. Roberts, P. L. Vidale, and P. A. O'Gorman (2010), Relative humidity changes in a warmer climate, *J Geophys Res-Atmos*, *115*, doi:Artn D0910410.1029/2009jd012585.

Shiva, J. S., D. G. Chandler, and K. E. Kunkel (2019), Localized Changes in Heat Wave Properties Across the United States, *Earths Future*, *7*(3), 300-319, doi:10.1029/2018ef001085.

Skamarock, W. C., J. B. Klemp, J. Dudhia, D. O. Gill, D. M. Barker, W. Wang, and J. G. Powers (2008), A description of the Advanced Research WRF version 3. NCAR Technical note-475+ STR.

Smith, T. T., B. F. Zaitchik, and J. M. Gohlke (2013), Heat waves in the United States: definitions, patterns and trends, *Climatic Change*, *118*(3-4), 811-825, doi:10.1007/s10584-012-0659-2.

Steadman, R. G. (1979), Assessment of Sultriness .1. Temperature-Humidity Index Based on Human Physiology and Clothing Science, *J Appl Meteorol*, *18*(7), 861-873, doi:Doi 10.1175/1520-0450(1979)018<0861:Taospi>2.0.Co;2.

Suggitt, A. J., P. K. Gillingham, J. K. Hill, B. Huntley, W. E. Kunin, D. B. Roy, and C. D. Thomas (2011), Habitat microclimates drive fine-scale variation in extreme temperatures, *Oikos*, *120*(1), 1-8.

Teuling, A. J., et al. (2010), Contrasting response of European forest and grassland energy exchange to heatwaves, *Nat Geosci*, *3*(10), 722-727.

Ukkola, A. M., A. J. Pitman, M. G. Donat, M. G. De Kauwe, and O. Angelil (2018), Evaluating the Contribution of Land-Atmosphere Coupling to Heat Extremes in CMIP5 Models, *Geophys Res Lett*, *45*(17), 9003-9012.

Vose, R. S., D.R. Easterling, K.E. Kunkel, A.N. LeGrande, and M.F. Wehner (2017), Temperature changes in the United States. In: Climate Science Special Report: Fourth National Climate Assessment*Rep*., 185-206 pp, U.S. Global Change Research Program, Washington, DC, USA, .

Wada, Y., et al. (2013), Multimodel projections and uncertainties of irrigation water demand under climate change, *Geophys Res Lett*, *40*(17), 4626-4632, doi:10.1002/grl.50686.

Wang, H. J., and Q. Y. Chen (2014), Impact of climate change heating and cooling energy use in buildings in the United States, *Energ Buildings*, *82*, 428-436, doi:10.1016/j.enbuild.2014.07.034.

Wasko, C., A. Sharma, and S. Westra (2016), Reduced spatial extent of extreme storms at higher temperatures, *Geophys Res Lett*, *43*(8), 4026-4032.

Wehrli, K., B. P. Guillod, M. Hauser, M. Leclair, and S. I. Seneviratne (2018), Assessing the dynamic versus thermodynamic origin of climate model biases, *Geophys Res Lett*, *45*(16), 8471-8479.

Wilbanks, T. B., Vatsal; Bilello, Daniel; Bull, Stanley; Ekmann, James; Horak, William; Huang, Y. Joe; Levine, Mark D.; Sale, Michael J.; Schmalzer, David and Scott, Michael J., (2008), Effects of Climate Change on Energy Production and Use in the United States*Rep*., US Department of Energy Publication.

Willett, K. M., N. P. Gillett, P. D. Jones, and P. W. Thorne (2007), Attribution of observed surface humidity changes to human influence, *Nature*, *449*(7163), 710-U716.

Zhou, Y. Y., et al. (2014), Modeling the effect of climate change on U.S. state-level buildings energy demands in an integrated assessment framework, *Appl Energ*, *113*, 1077-1088, doi:10.1016/j.apenergy.2013.08.034.

Zhu, X., and T. J. Troy (2018), Agriculturally Relevant Climate Extremes and Their Trends in the World's Major Growing Regions, *Earths Future*, *6*(4), 656-672, doi:10.1002/2017ef000687.

Appendix

Table 2.1 List of the dynamically downscaled CMIP5 GCMs.

No.	GCM Name	Ensemble
1	ACCESS1-0	r1i1p1
2	BCC-CSM1-1	r1i1p1
3	CCSM4	r6i1p1
4	CMCC-CM	r1i1p1
5	FGOALS-g2	r1i1p1
6	GFDL-ESM2M	r1i1p1
7	MIROC5	r1i1p1
8	MPI-ESM-MR	r1i1p1
9	MRI-CGCM3	r1i1p1
10	NorESM1-M	r1i1p1
11	IPSL-CM5A-LR	r1i1p1

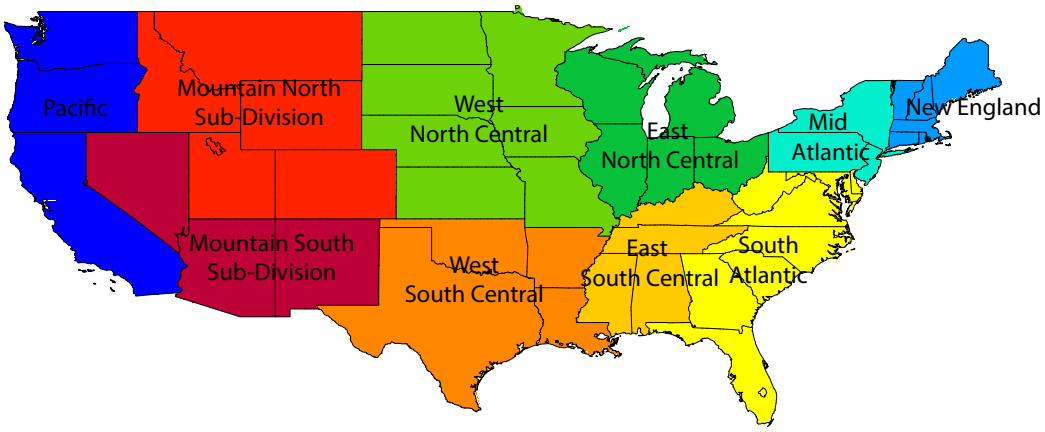

Figure 2.1 Map showing US Census divisions.

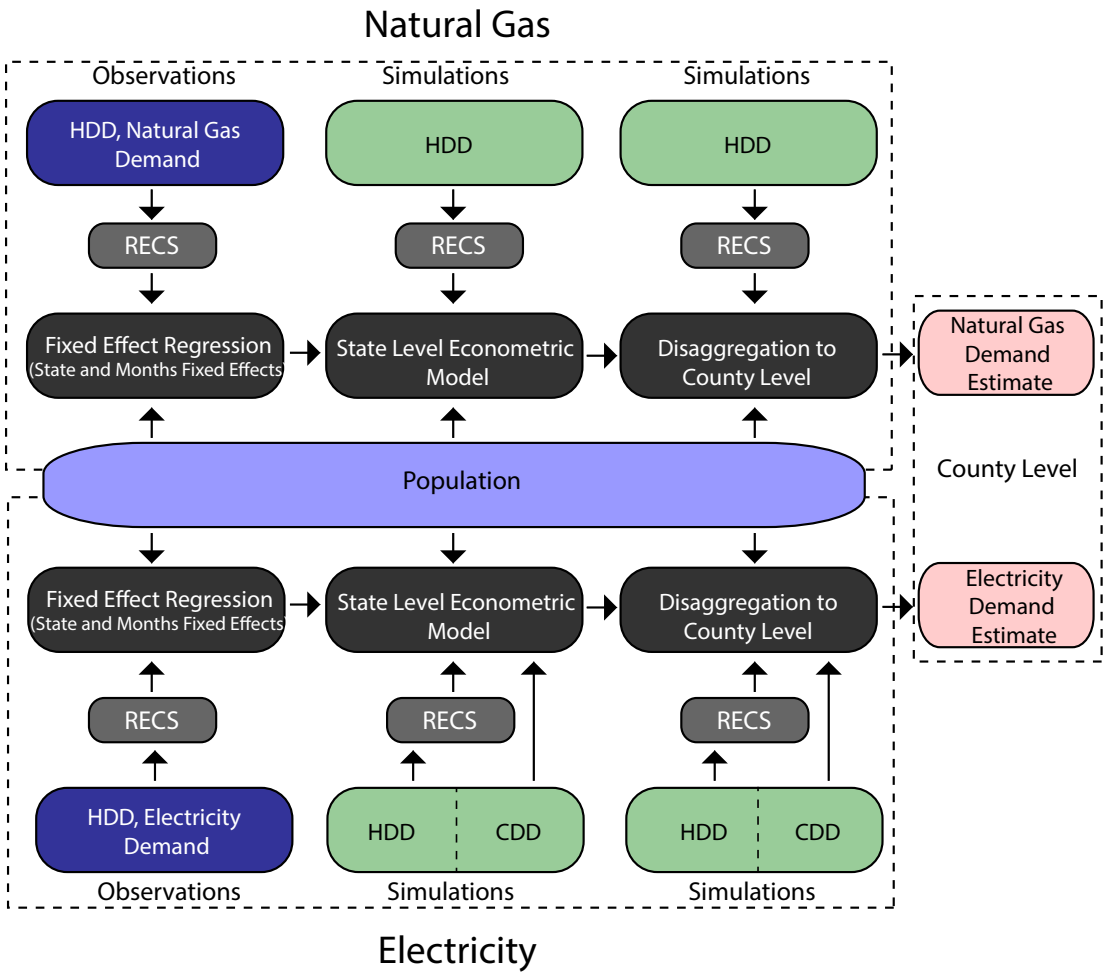

Figure 2.2 Schematic showing various steps of methodology.

Table 2.2 Summary of the electricity demand econometric model. Yes implies the use if that particular fixed effect. Symbols are as show in equation 1.

	$\log(E_{sch}^{smy})$	Std. Error	t-statistics
α_{e0}	0.00003	1.80E-06	16.63
α_{e1}	-1.79E-10	4.77E-11	-3.75
β_{e0}	0.0000424	9.65E-07	43.94
β_{e1}	-3.01E-10	1.18E-11	-25.45
γ_{e0}	1.44E-07	2.99E-09	48.37
c_e	12.60142	0.0216013	583.36
N	9,408		
Fixed Effects			
County	Yes		
Month	Yes		
R-square	0.9862		
F-statistics	10423.33		

Table 2.3 Summary of the natural gas demand econometric model. Yes implies the use if that particular fixed effect. Symbols are as show in equation 1.

	$\log(NG_{sh}^{smy})$	Std. Error	t-statistics
α_{ng0}	0.0000409	1.79E-06	22.86
α_{ng1}	-6.10E-10	3.57E-11	-17.07
γ_{ng0}	4.82E-08	4.73E-09	10.18
c_{ng}	8.158396	0.029287	278.57
N	7,052		
Fixed Effects			
State	Yes		
Month	Yes		
R-square	0.9804		
F-statistics	5930.69		

Figure 2.3 Historical period comparisons. Climatology of heating degree days (HDD) in (a) observations (PRISM) (b) simulations (RegCM4). Climatology of cooling degree days (CDD) in (c) PRISM (d) RegCM4. Trends in HDD in e) PRISM (f) RegCM4. Trends in CDD in (g) PRISM (h) RegCM4. The units for HDD and CDD are in degree Celsius i) Trends in HDD and CDD (PRISM and RegCM4), natural gas and electricity demands (EIA and RegCM4) for ten metropolitan areas across the US. An upward (downward) triangle indicates positive (negative) trend. Separate triangles are drawn for the observation and the RegCM4 if the direction of trend does not match with "o" inside the triangle representing the observations. Filled triangle indicate trend is significant in both the observations and the RegCM4. All comparisons are for 1981 to 2005 historical period except for the comparisons with the EIA data that corresponds to 1990 to 2005 historical period. RegCM4 results represent mean of all ensemble members.

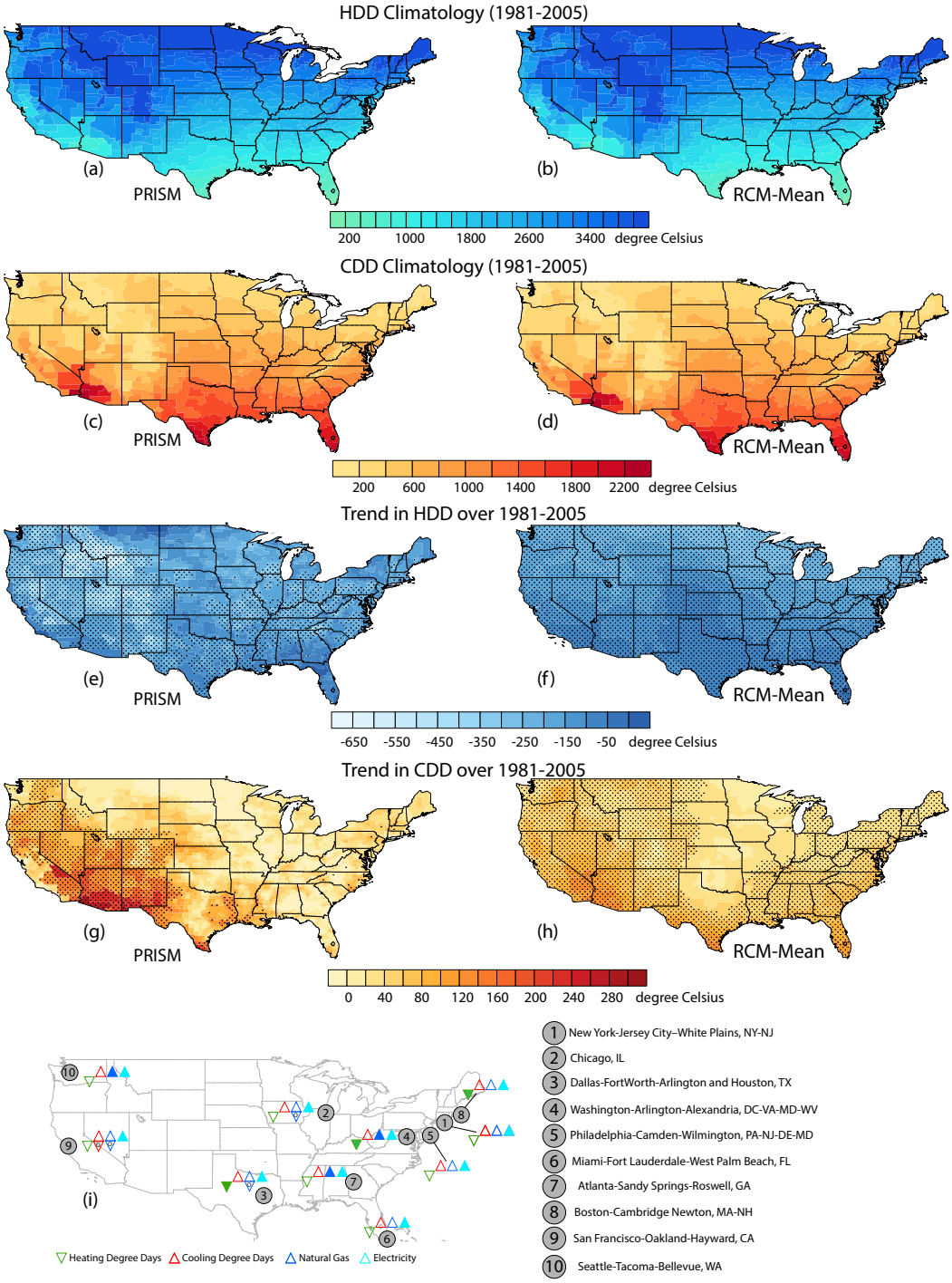
HDD Climatology (1981-2005)
(a)
PRISM
(b)
RCM-Mean
200 1000 1800 2600 3400 degree Celsius
CDD Climatology (1981-2005)
(c)
PRISM
(d)
RCM-Mean
200 600 1000 1400 1800 2200 degree Celsius
Trend in HDD over 1981-2005
(e)
PRISM
(f)
RCM-Mean
-650 -550 -450 -350 -250 -150 -50 degree Celsius
Trend in CDD over 1981-2005
(g)
PRISM
(h)
RCM-Mean
0 40 80 120 160 200 240 280 degree Celsius
(i)
Heating Degree Days
Cooling Degree Days
Natural Gas
Electricity
1 New York-Jersey City--White Plains, NY-NJ
2 Chicago, IL
3 Dallas-FortWorth-Arlington and Houston, TX
4 Washington-Arlington-Alexandria, DC-VA-MD-WV
5 Philadelphia-Camden-Wilmington, PA-NJ-DE-MD
6 Miami-Fort Lauderdale-West Palm Beach, FL
7 Atlanta-Sandy Springs-Roswell, GA
8 Boston-Cambridge Newton, MA-NH
9 San Francisco-Oakland-Hayward, CA
10 Seattle-Tacoma-Bellevue, WA

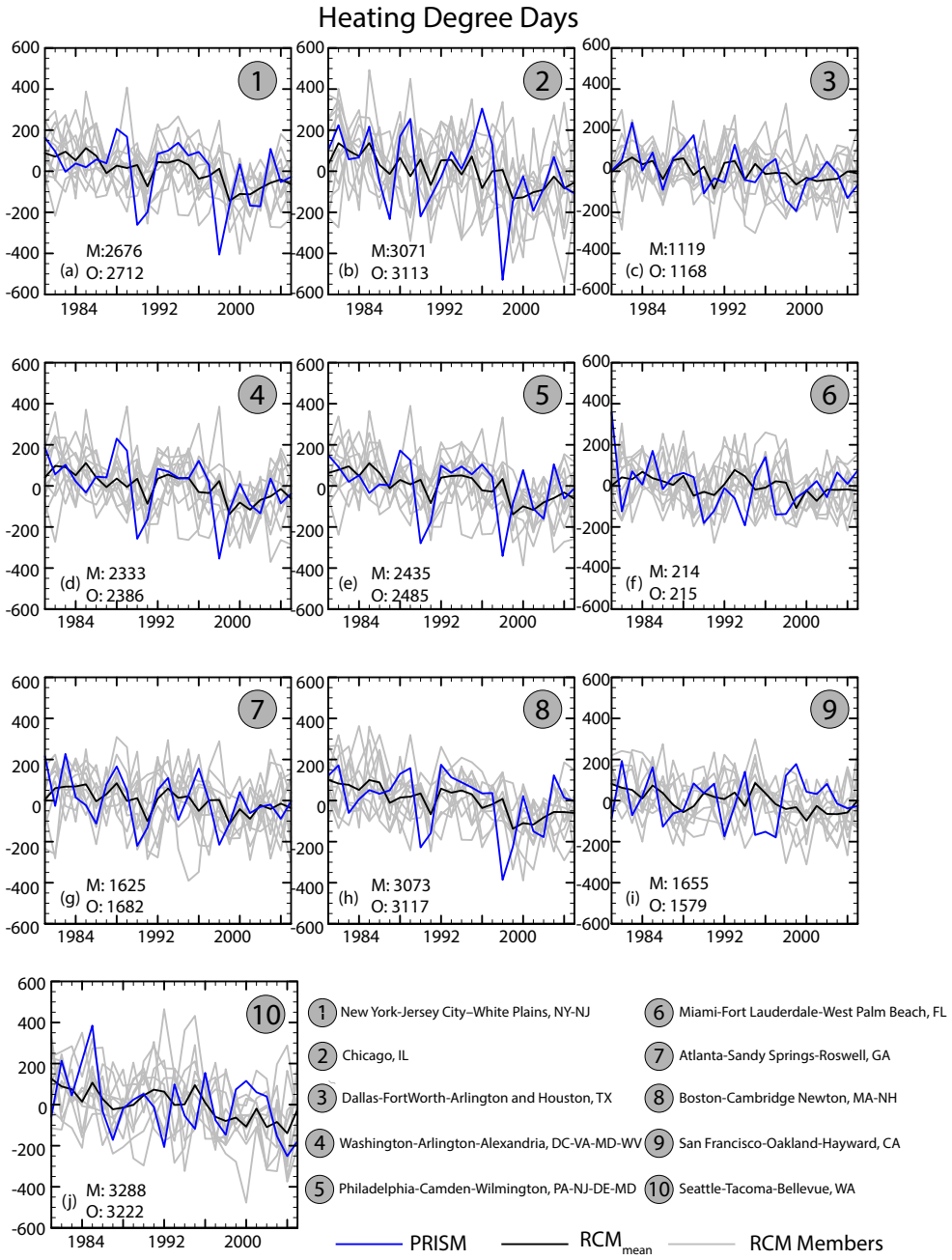

Figure 2.4 Time series of average annual HDD anomaly over 1981 to 2005 period for PRISM, 11 RegCM4 ensemble members and RegCM4 mean for ten metropolitan areas across the US. The values in the plots are the average annual HDD values in degree Celsius during the 1981-2005 period for RegCM4 mean (M) and Observations (O).

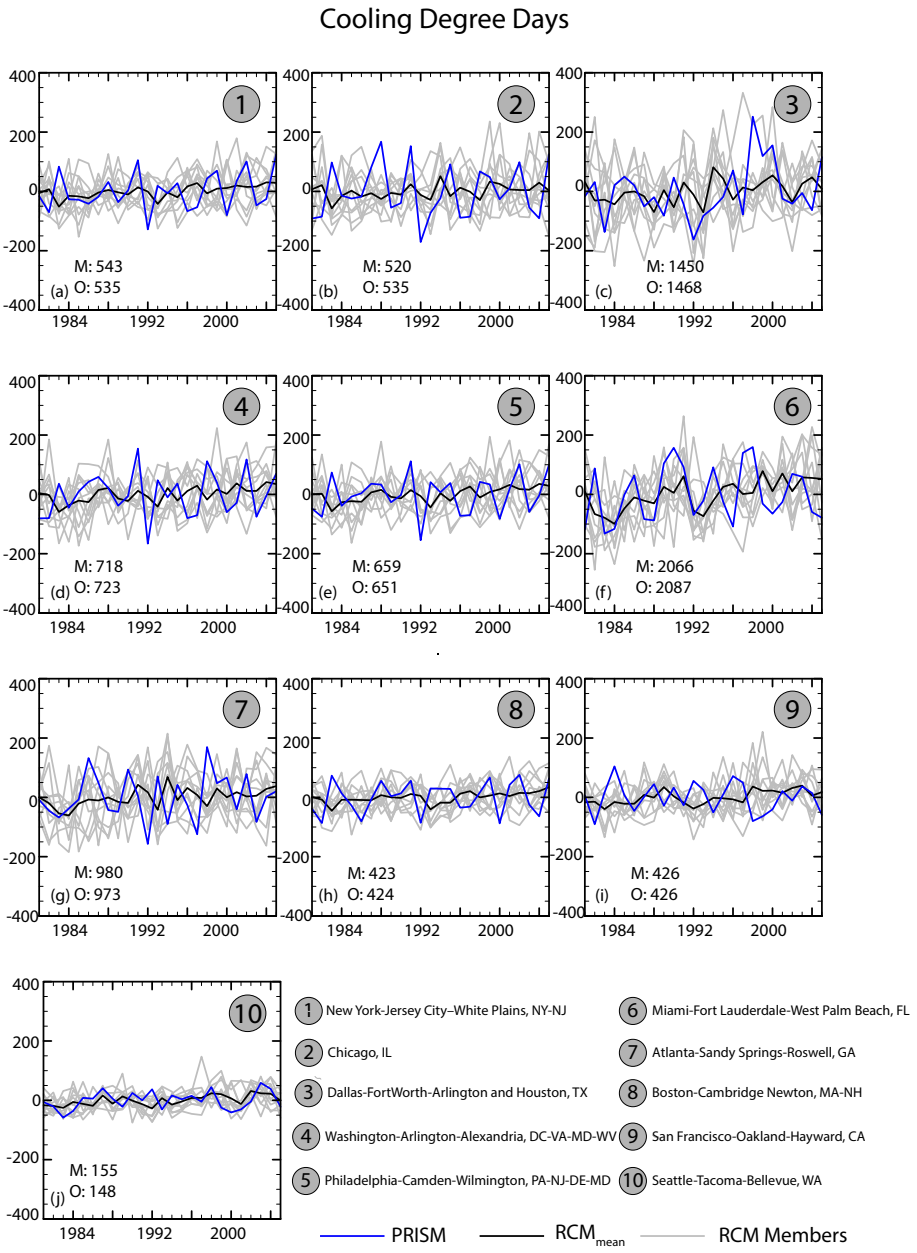

Figure 2.5 Time series of average annual CDD anomaly over 1981 to 2005 period for PRISM, 11 RegCM4 ensemble members and RegCM4 mean for ten metropolitan areas across the US. The values in the plots are the average annual CDD values in degree Celsius during the 1981-2005 period for RegCM4 mean (M) and Observations (O).

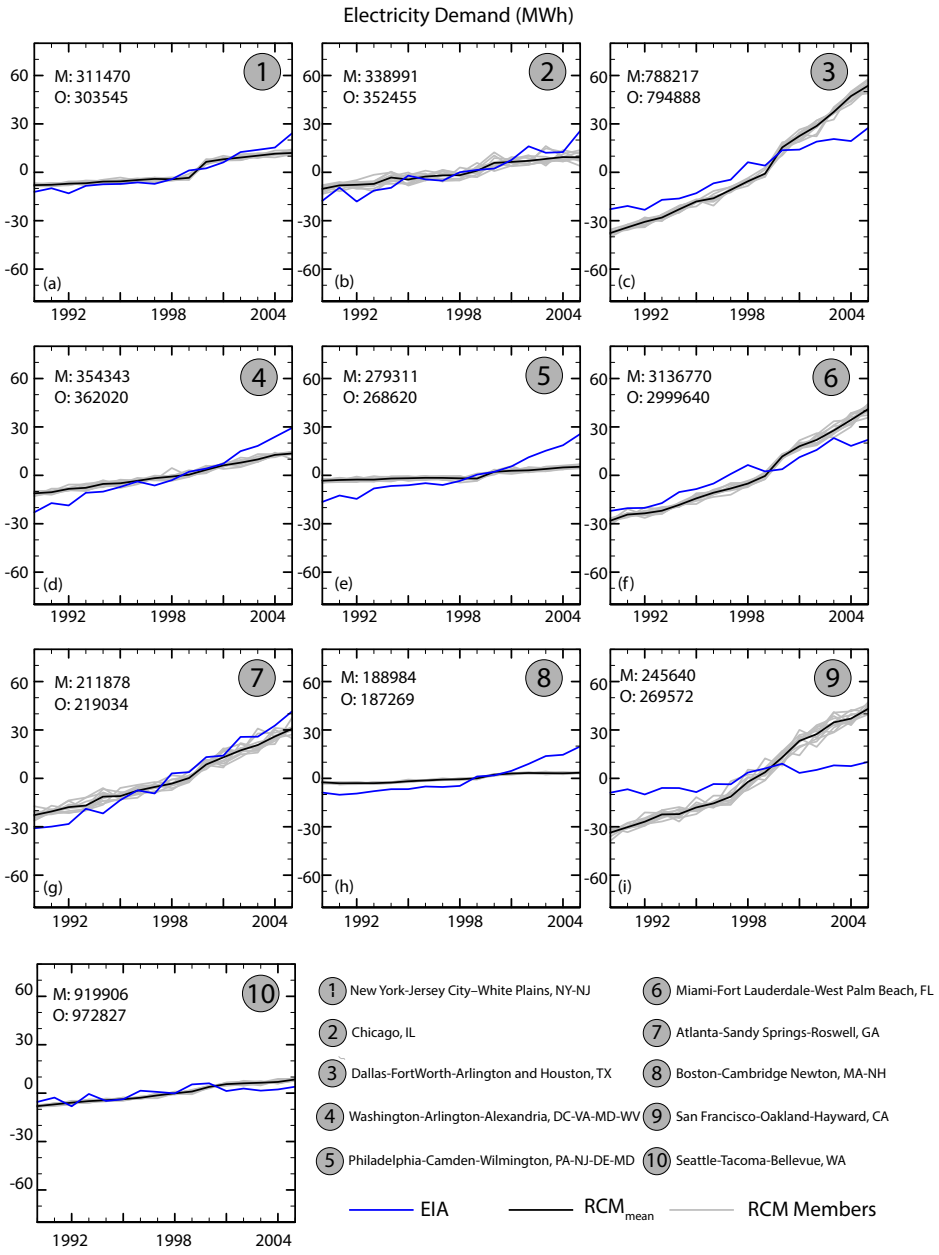

Figure 2.6 Time series of percent anomaly in annual electricity demand over 1990 to 2005 period for EIA, 11 RegCM4 ensemble members and RegCM4 mean for ten metropolitan areas across the US. The values in the plot are the average annual electricity demand values in MWh during the 1990-2005 period for RegCM4 mean (M) and Observations (O).

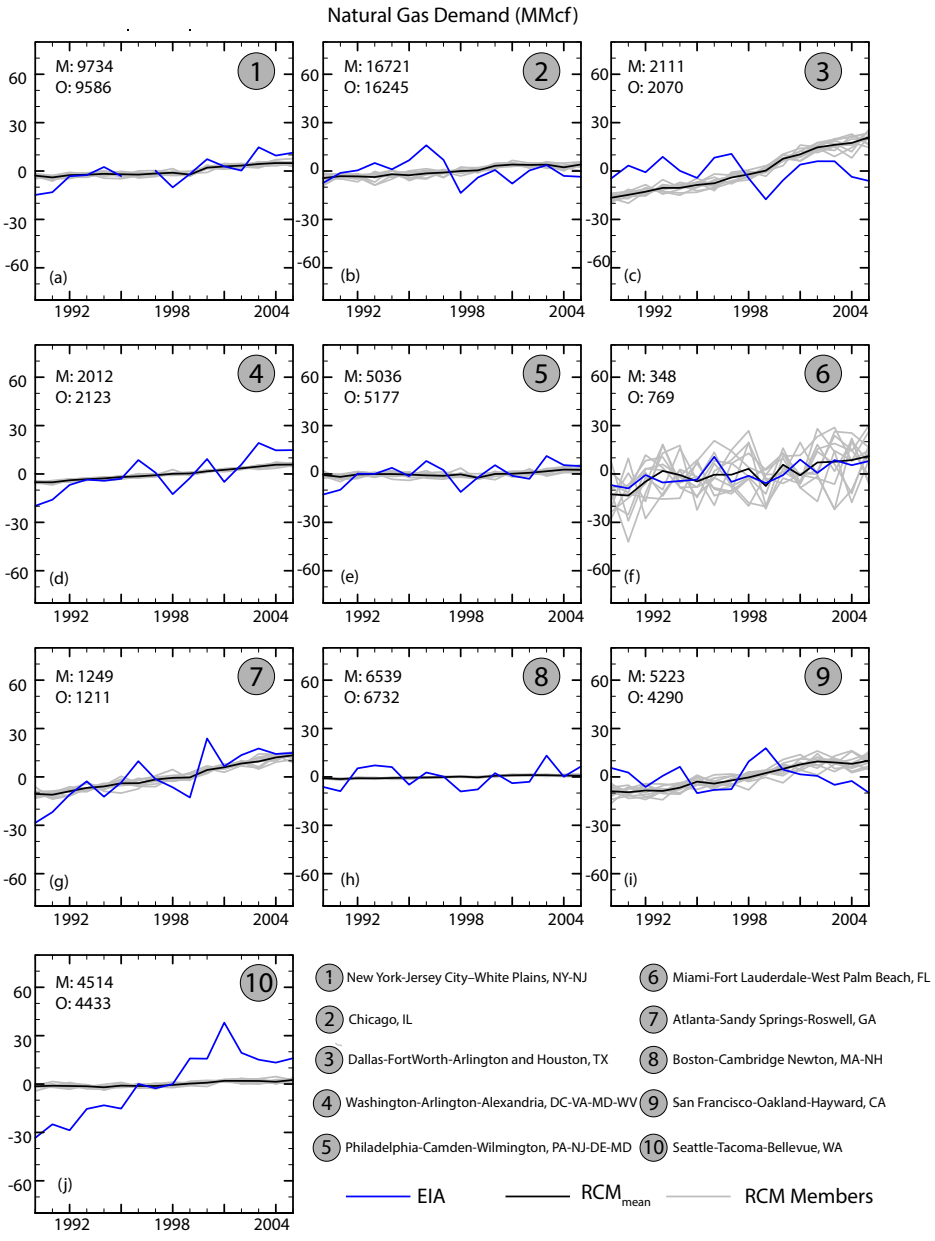

Figure 2.7 Time series of percent anomaly in annual natural gas demand over 1990 to 2005 period for EIA, 11 RegCM4 ensemble members and RegCM4 mean for ten metropolitan areas across the US. The values in the plots are the average annual natural gas demand values in MMcf during the 1990-2005 period for RegCM4 mean (M) and Observations (O).

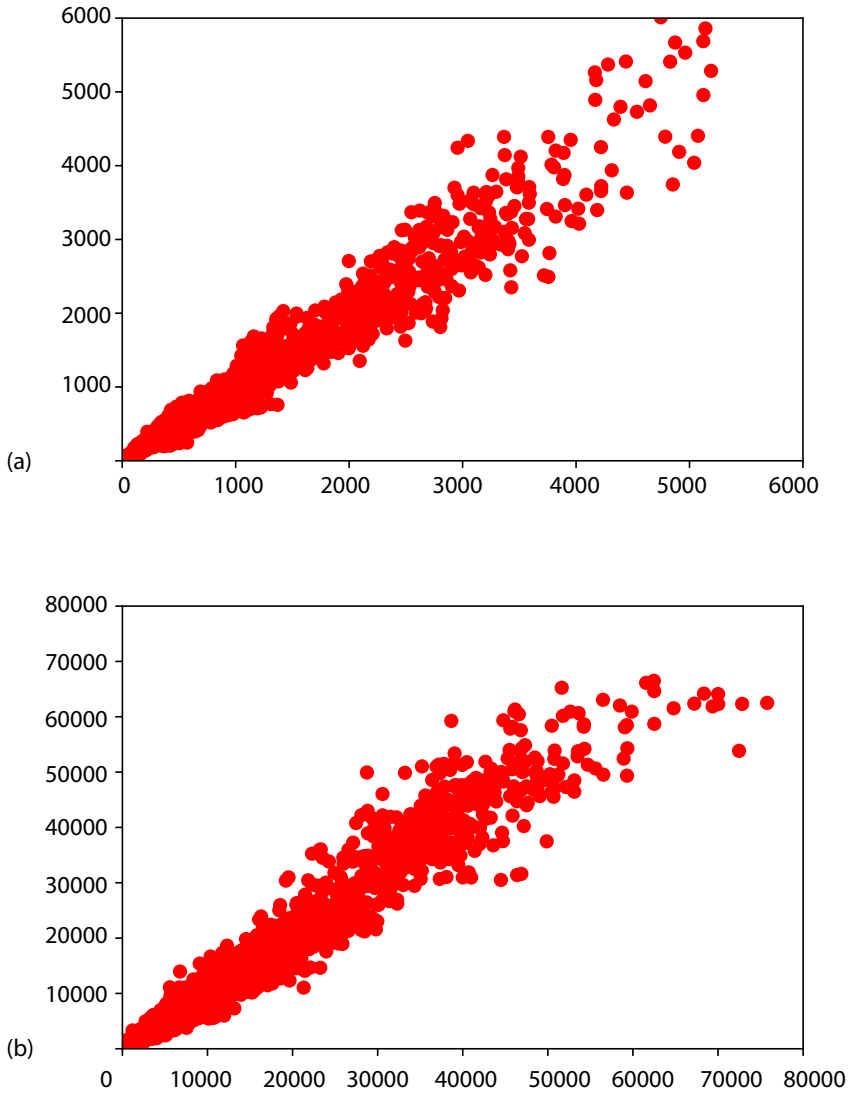

Figure 2.8 Scatter plots showing model predicted demand as simulated by the statistical model, driven with climate inputs from RCM, versus EIA consumption for period 1990 to 2005 for (a) Electricity (GWh) (b) Natural gas (MMcf). RCM results represent mean of all ensemble members.

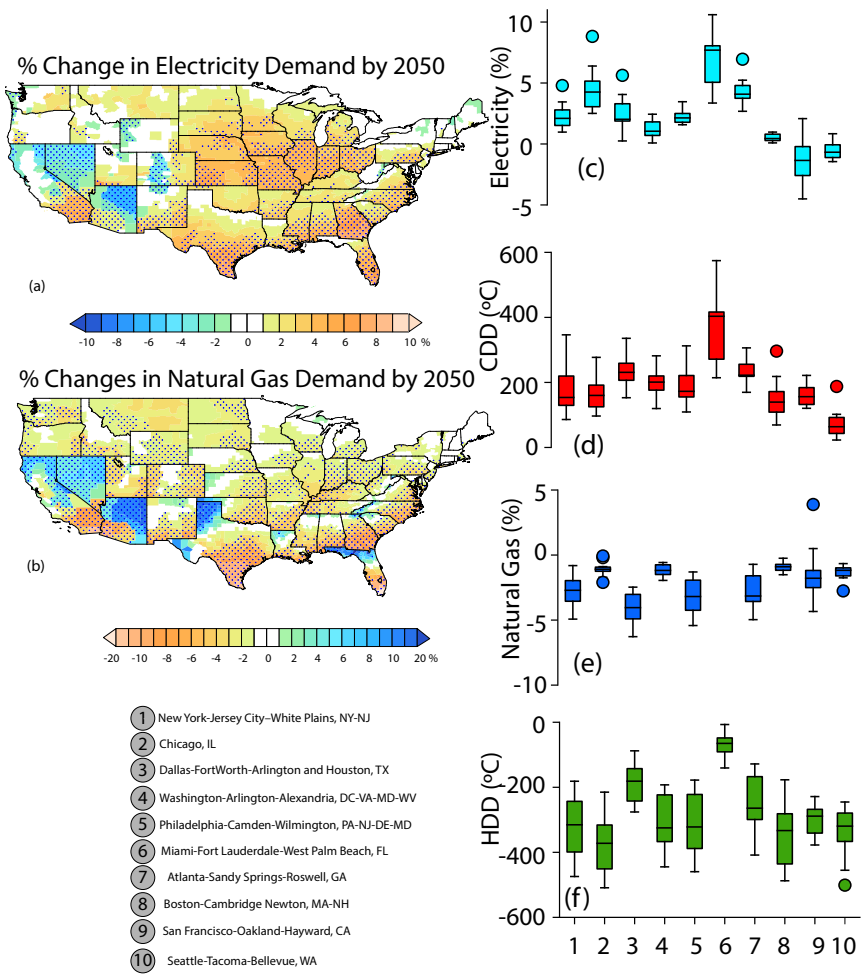

Figure 2.9 Future period projected changes. Percent change in the residential (a) electricity demand (b) natural gas demand. Box and whisker plots show the spread of projected changes across RegCM4 11 ensemble members for (c) residential electricity demand, (d) CDD, (e) residential natural gas demand, and (f) HDD for the ten metropolitan areas. Changes are shown as absolute values in (d) and (f) and percent values in (c) and (e). Changes for Miami-Fort Lauderdale-West Palm are not shown in (e) due to negligibly small natural gas demand. Changes are calculated at county level for each year as the departure from the 2011 value. We then fit a linear regression to 40 years time series in the future period (2011-2050). Finally, we calculate the change as the percent or absolute difference between the last and first points on the regression line.

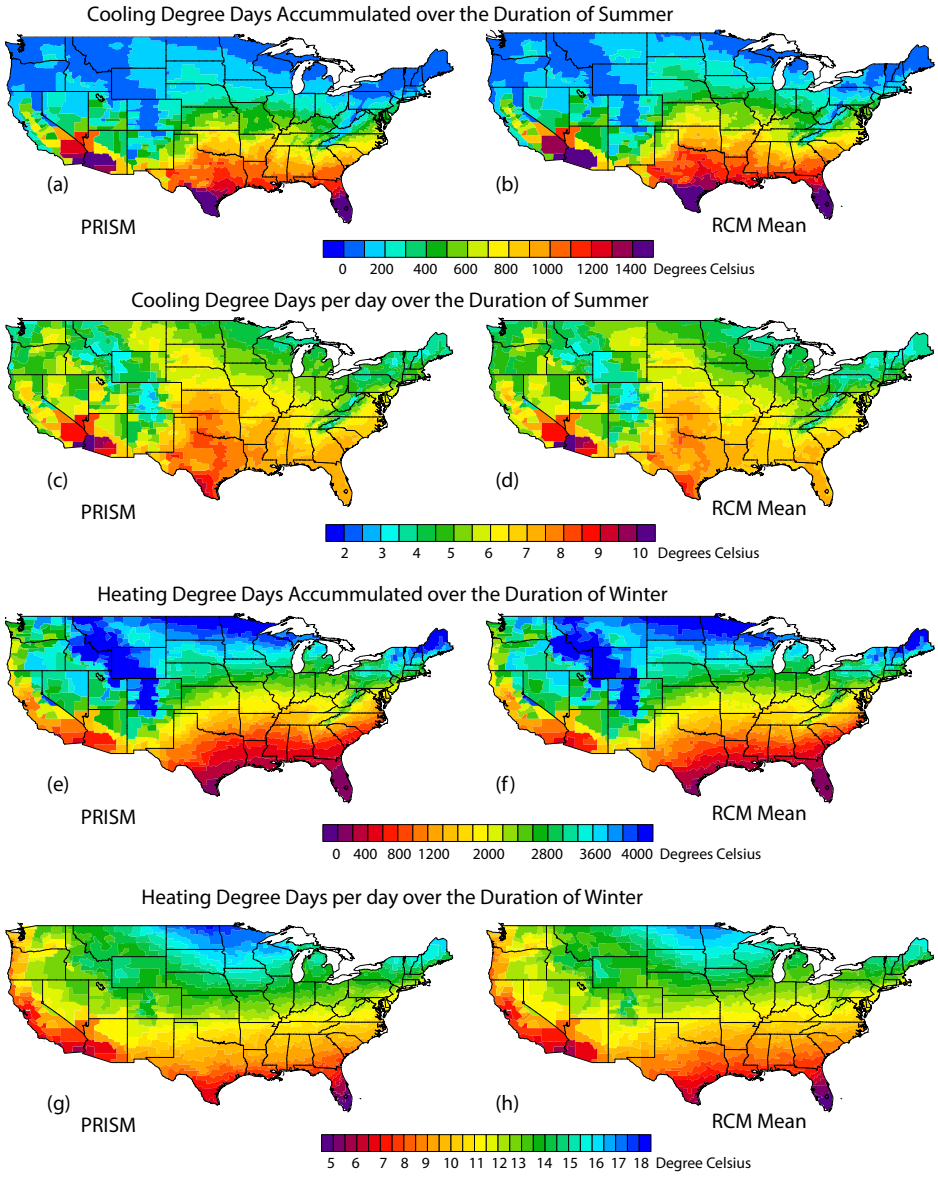

Figure 2.10 Historical comparisons (1981 to 2005) between the observations (PRISM) and simulations (RegCM4) for (a, b) CDD accumulated over the duration of summer, (c, d) CDD per day during summer, (e, f) HDD accumulated over the duration of winter, (g, h) HDD per day during winter. All the units are in degree Celsius.

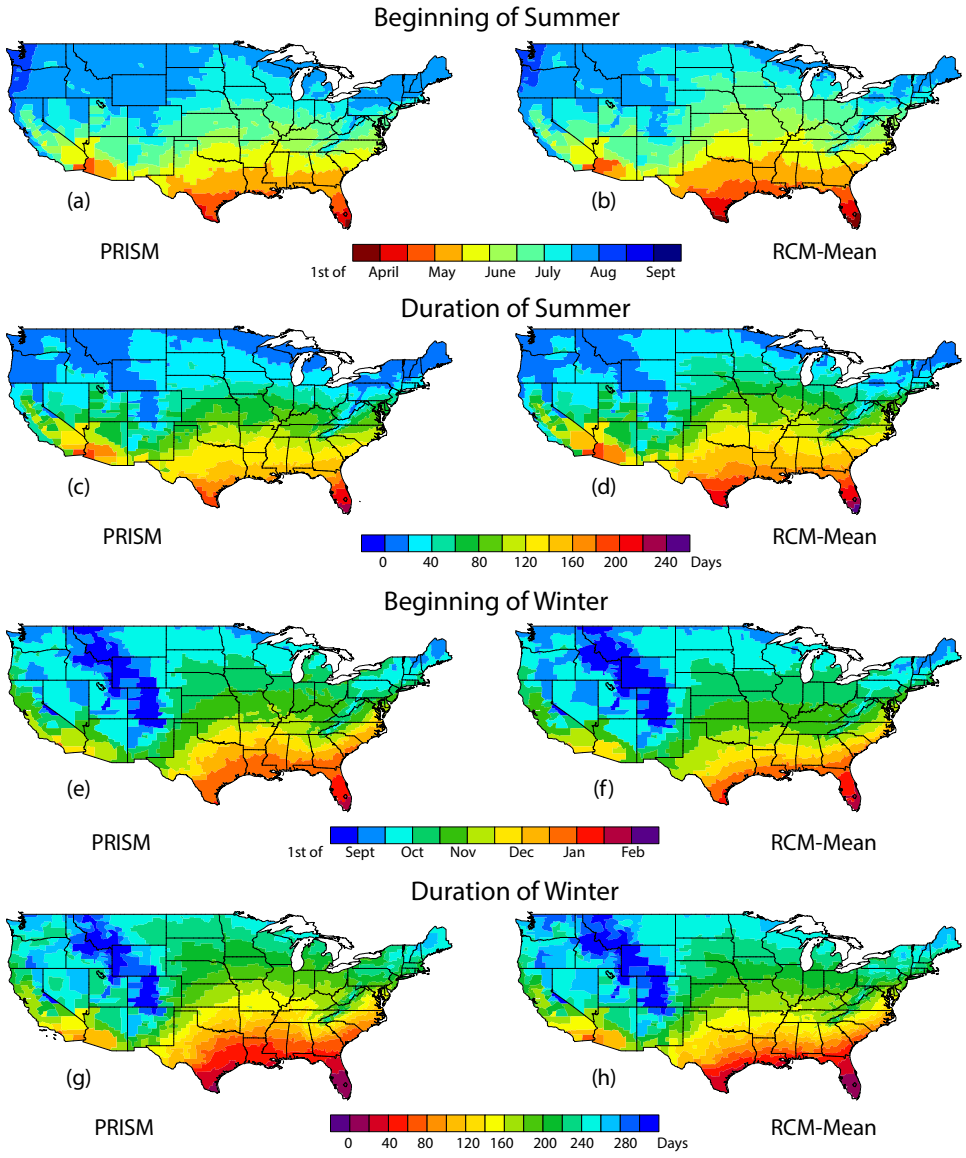

Figure 2.11 Beginning of summer in (a) PRISM (b) RegCM4. Duration of summer in (c) PRISM (d) RegCM4. Beginning of winter in (e) PRISM (f) RegCM4. Duration of winter in (g) PRISM (h) RegCM4. All calculations are based on 1981 to 2005 period. RegCM4 results represent mean of all ensemble members.

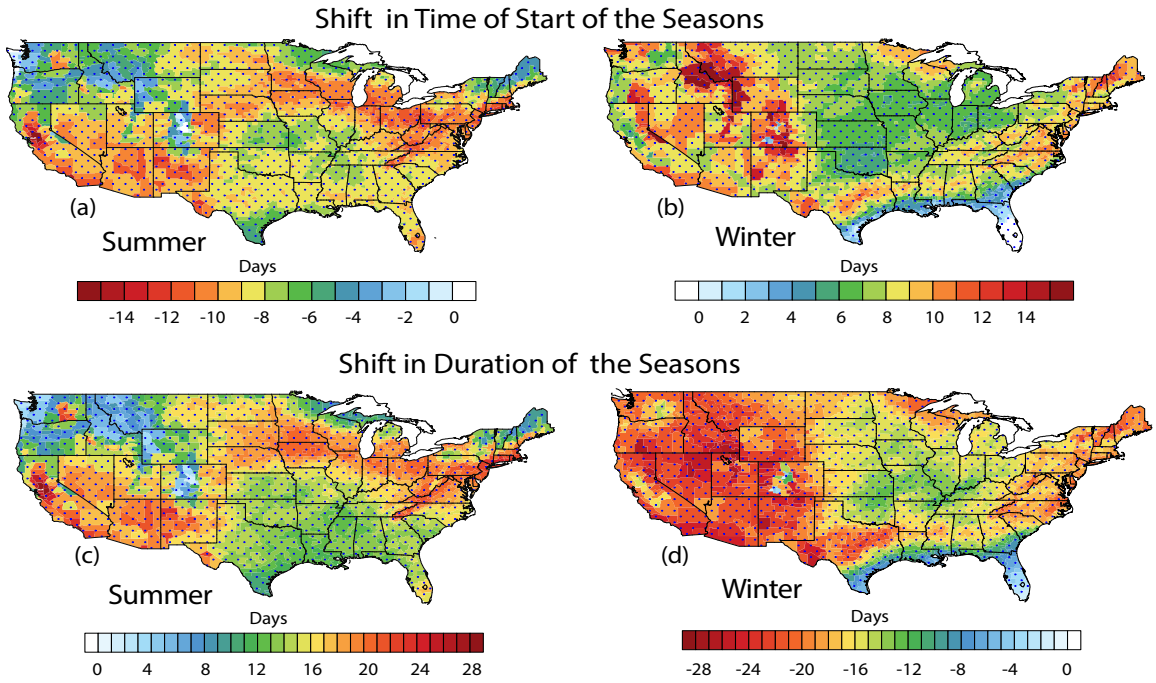

Figure 2.12 Projected changes (2011 to 2050 minus 1981 to 2005) in (a) timing of summer (b) timing of winter (c) duration of summer (d) duration of winter in RegCM4.

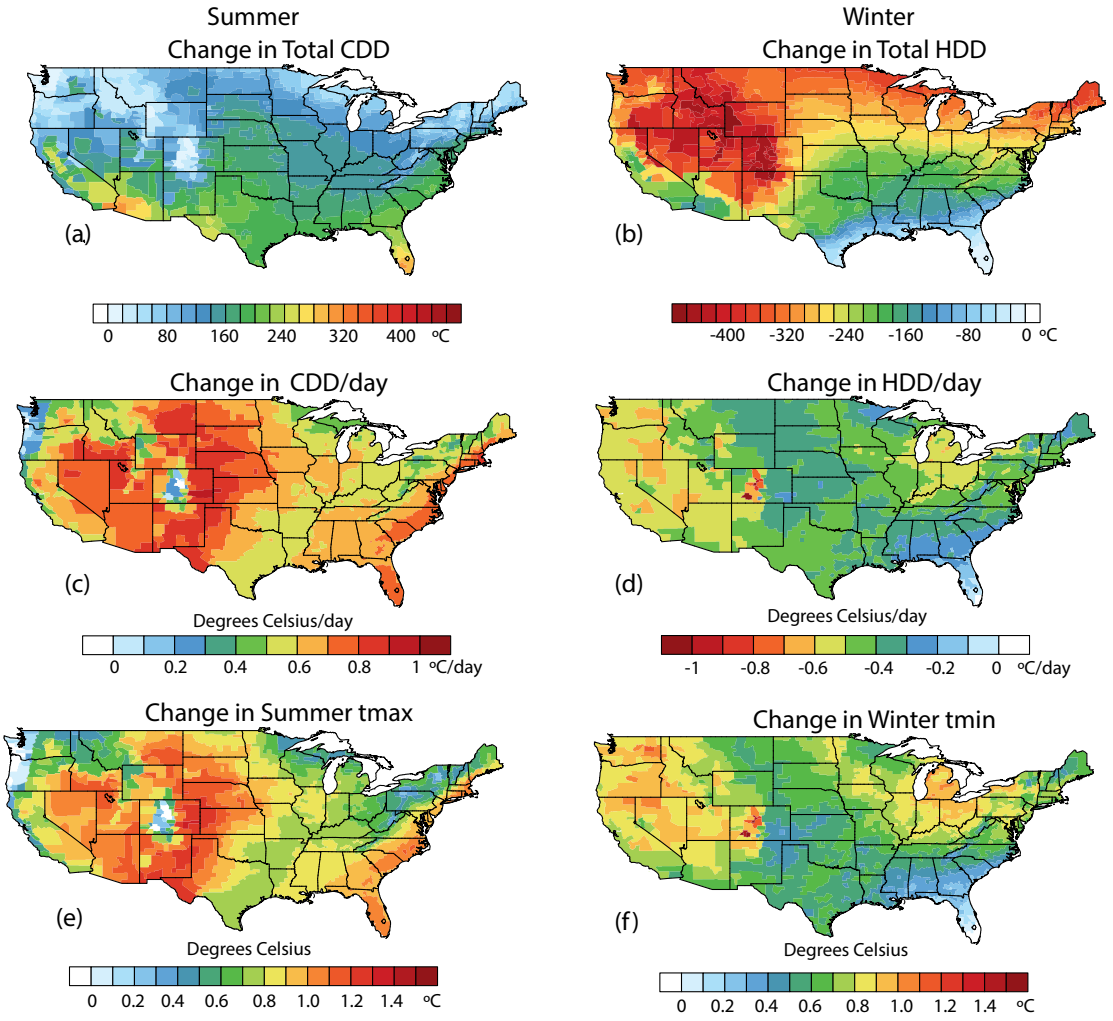

Figure 2.13 Future changes (2011 to 2050 minus 1981 to 2005) in (a) accumulated CDD during summer, (b) accumulated HDD during winter, (c) CDD per day during summer, (d) HDD per day during winter, (e) daily maximum temperature during summer, (f) daily minimum temperature during winter. All the units are in degree Celsius.

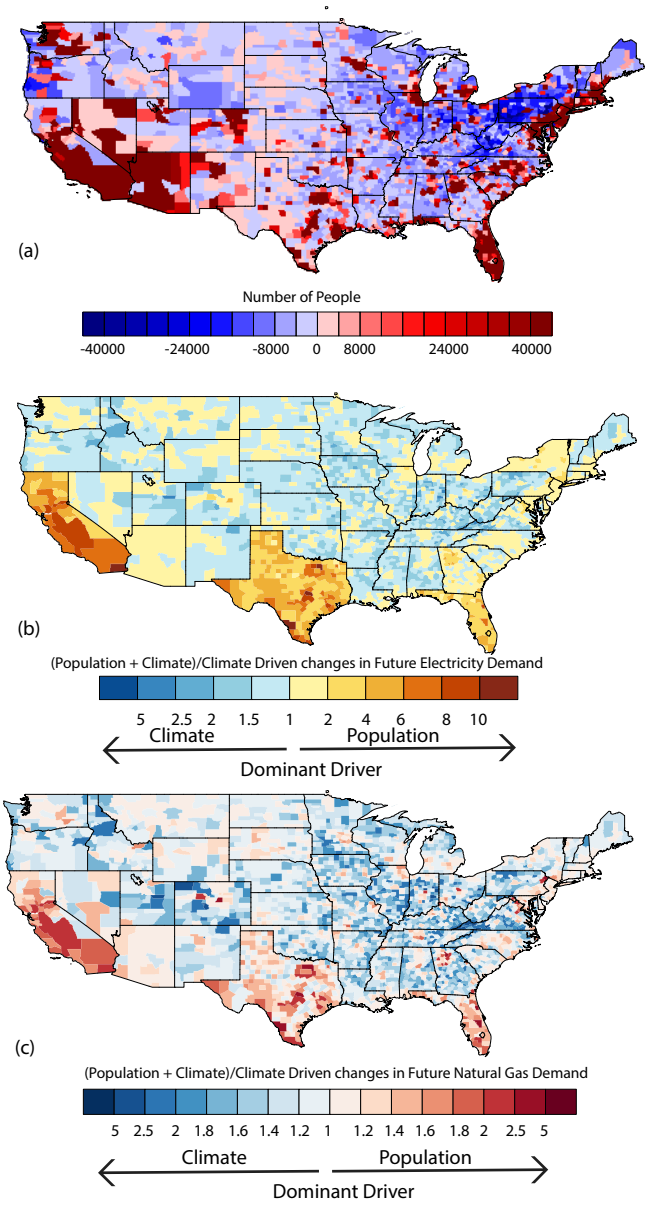

Figure 2.14 (a) Projected future changes in the population under EPA A2 scenario with respect to 2005 Census population. Relative changes in demand (b) electricity (c) natural gas with and without population changes in the future period (2011-2050). The relative change is calculated by dividing the demand projections when econometric model considers both population change and climate change by the demand projections when econometric model only considers climate change.

Figure 3.1 Scatter plots between the mean duration and (a-d) the mean intensity of the heatwaves, (e-h) the mean percentage area under the heatwaves for Southeast, Northeast-Midwest, Central and West US respectively. Each circle represents average characteristics of heatwaves (filled for AT_{max} and hollow for T_{max}) during each summer (JJA). Line plots show mean percentage area under heatwaves (solid lines for AT_{max} and dashed lines for T_{max}) over the Southeast for JJA during (i) 2010 (i) 2012. The spatial maps show the average differences between AT_{max} and T_{max} magnitudes during the heatwaves in 2010 for (k) WRF-CTRL (l) PRISM and in 2012 for (m) WRF-CTRL (n) PRISM. Black color denote observations (PRISM) and red color indicate WRF-CTRL in scatter as well as line plots. The four regions are marked in Figure 1m.

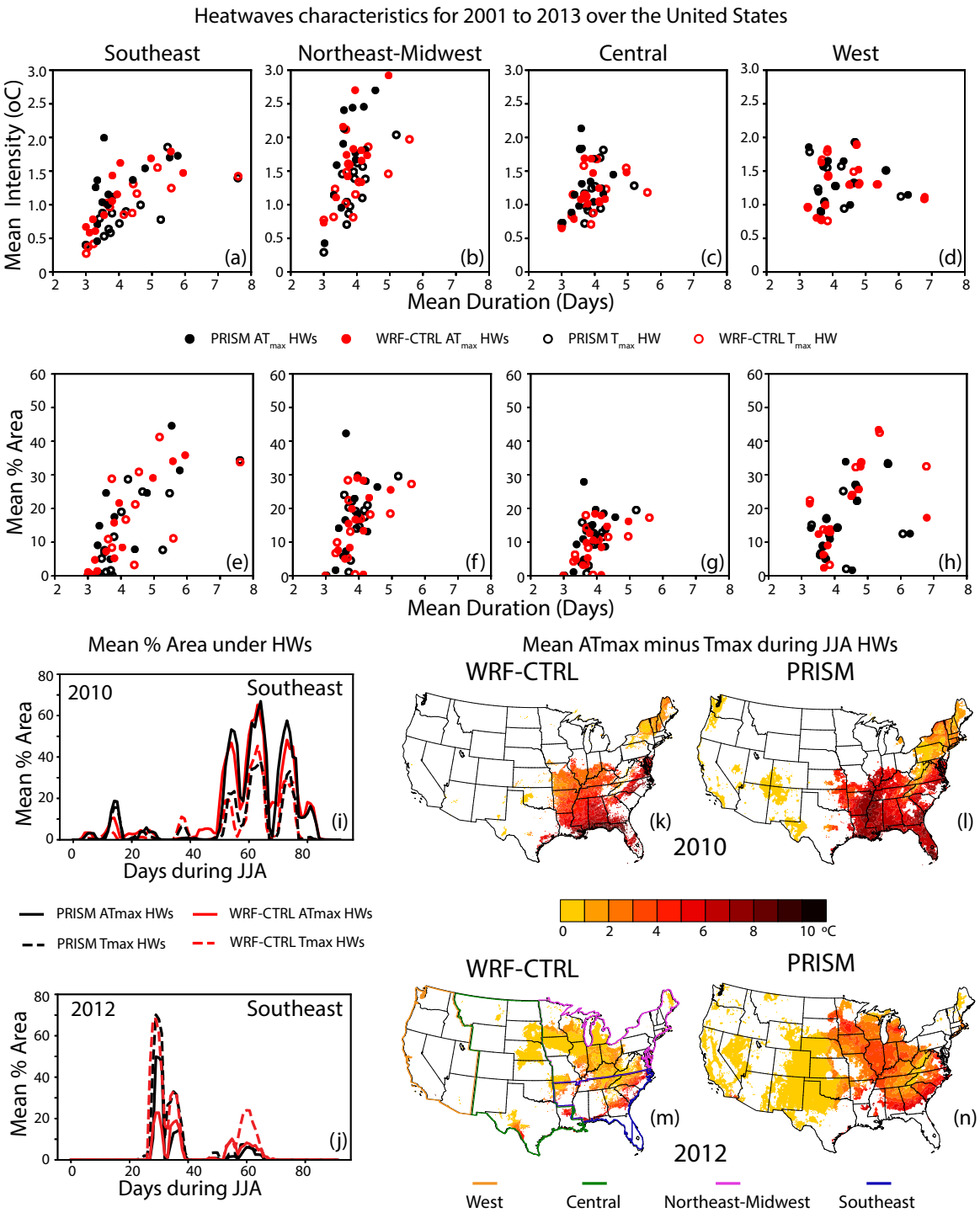
Heatwaves characteristics for 2001 to 2013 over the United States
Southeast
Northeast-Midwest
Central
West
Mean Intensity (oC)
Mean Duration (Days)
(a)
(b)
(c)
(d)
PRISM ATmax HWs
WRF-CTRL ATmax HWs
PRISM Tmax HW
WRF-CTRL Tmax HW
Mean % Area
(e)
(f)
(g)
(h)
Mean % Area under HWs
2010
Southeast
(i)
Days during JJA
PRISM ATmax HWs
WRF-CTRL ATmax HWs
PRISM Tmax HWs
WRF-CTRL Tmax HWs
2012
Southeast
(j)
Mean ATmax minus Tmax during JJA HWs
WRF-CTRL
PRISM
(k)
(l)
2010
0 2 4 6 8 10 °C
WRF-CTRL
PRISM
(m)
(n)
2012
West
Central
Northeast-Midwest
Southeast

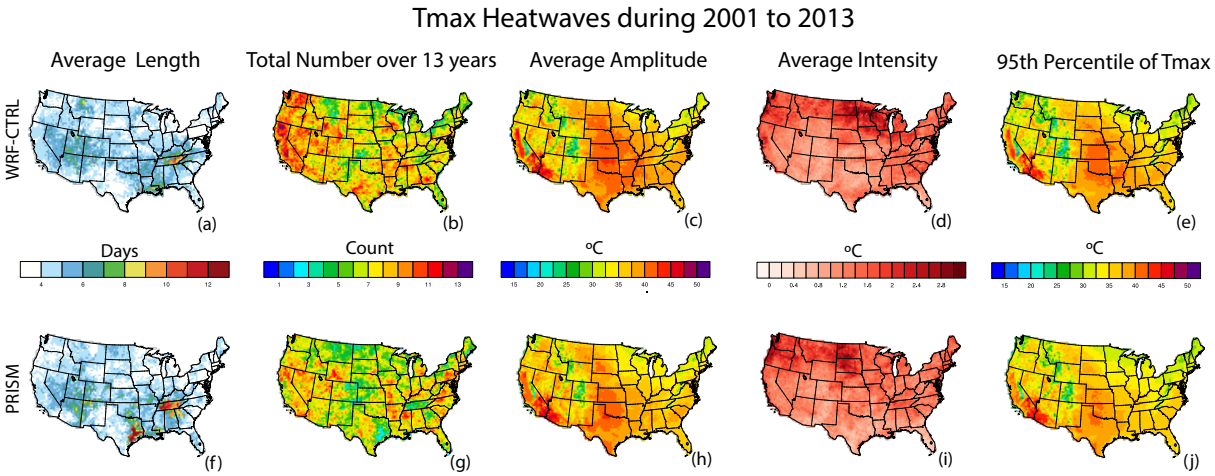

Figure 3.2 Spatial plots showing average length, total number, average amplitude, average intensity of T_{max} heatwaves, 95th percentile of Tmax over 2001 to 2013 in (a-e) WRF-CTRL (f-j) PRISM respectively.

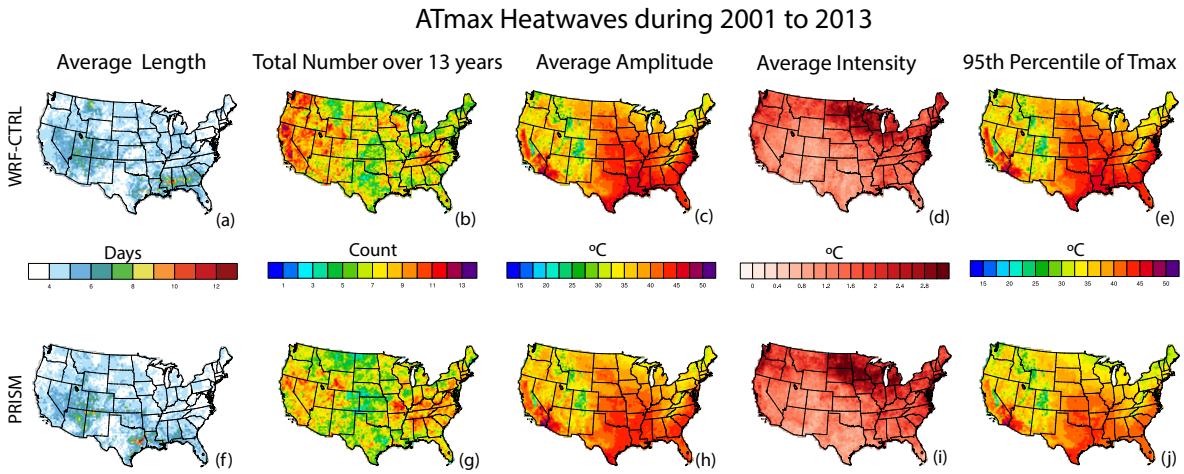

Figure 3.3 Spatial plots showing average length, total number, average amplitude, average intensity of AT_{max} heatwaves, 95th percentile of AT_{max} over 2001 to 2013 in (a-e) WRF-CTRL (f-j) PRISM respectively.

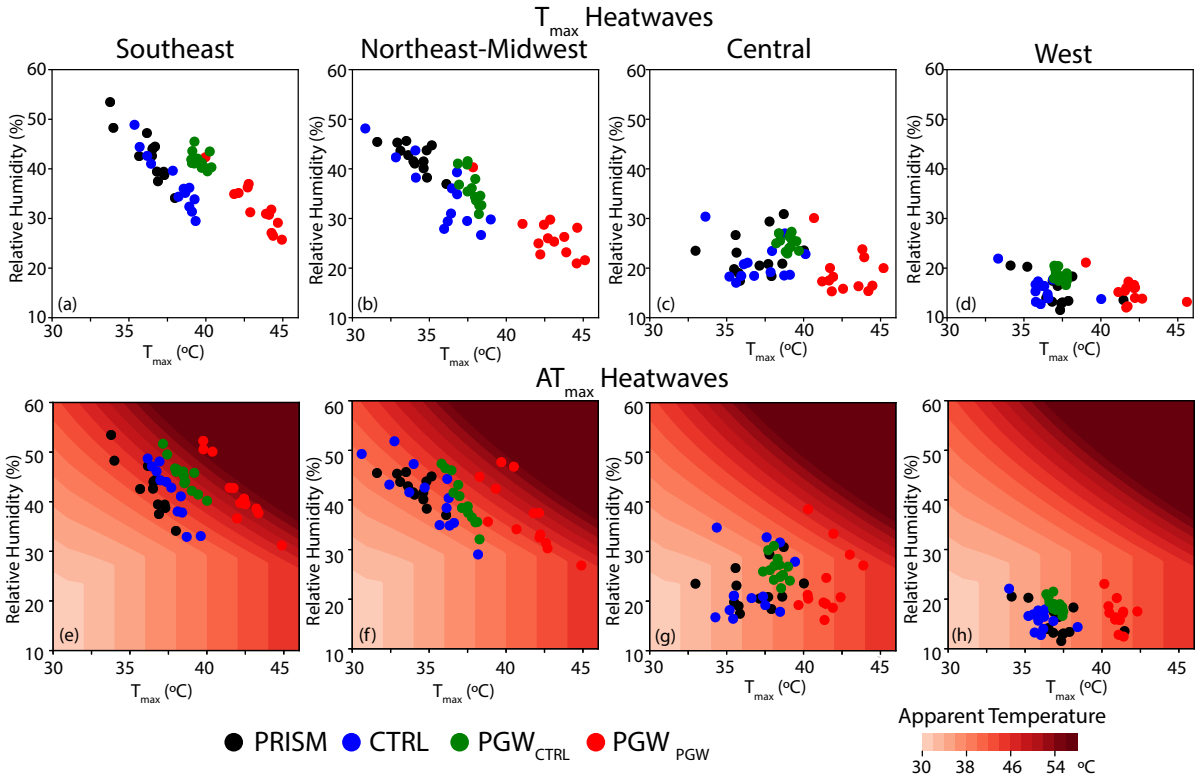

Figure 3.4 Scatter plots between average T_{max} and average relative humidity during (a-d) T_{max} heatwaves (e-h) AT_{max} heatwaves for Southeast, Northeast-Midwest, Central and West US respectively. Each circle represent averages during heatwaves occurring in summer (JJA). Black, blue, green and red circles are used for PRISM, CTRL, PGW_{CTRL} and PGW_{PGW} heatwaves respectively. The background contours in (e-h) correspond to respective values for AT_{max}.

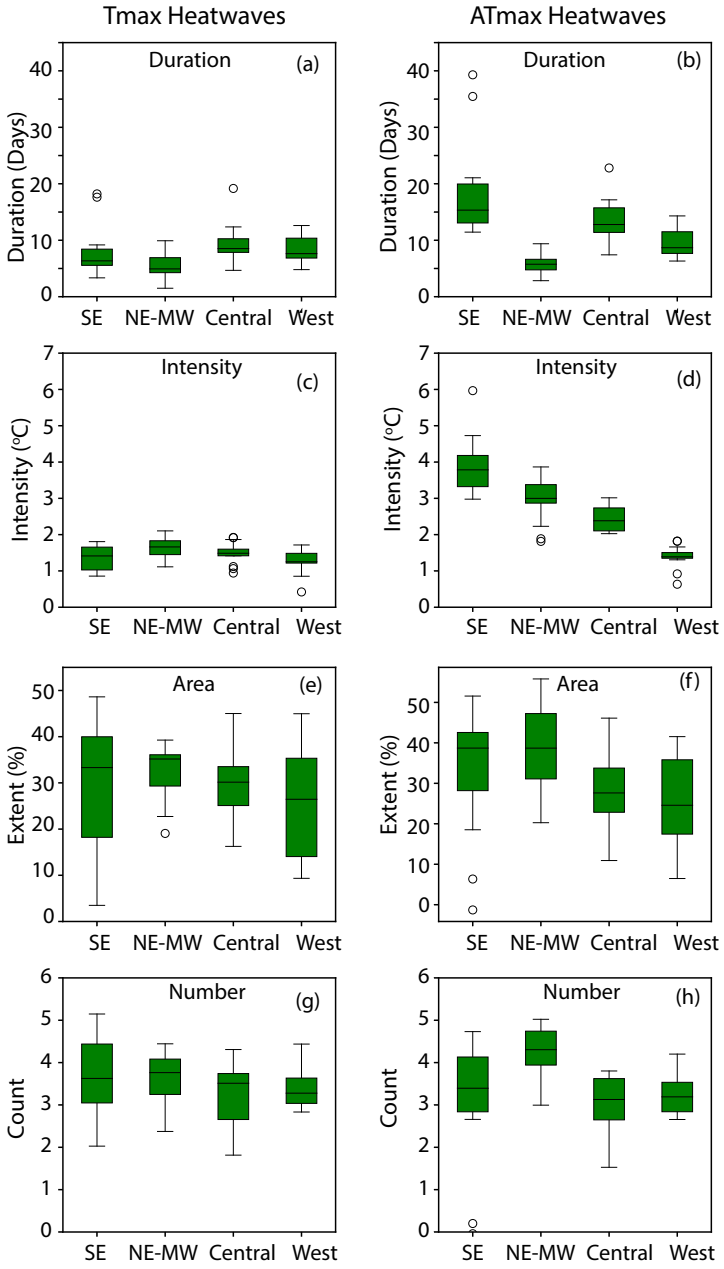

Figure 3.5 Box plots showing the spread in paired differences in characteristics between PGW_{CTRL} and CTRL heatwaves for each year over the 13 year analysis period (2001 to 2013) during T_{max} and AT_{max} heatwaves for (a,b) average duration (c,d) average intensity (e,f) percentage land area (g,h) number respectively. All changes shown here are significant at 95 percent confidence level using two tailed Student's T-test.

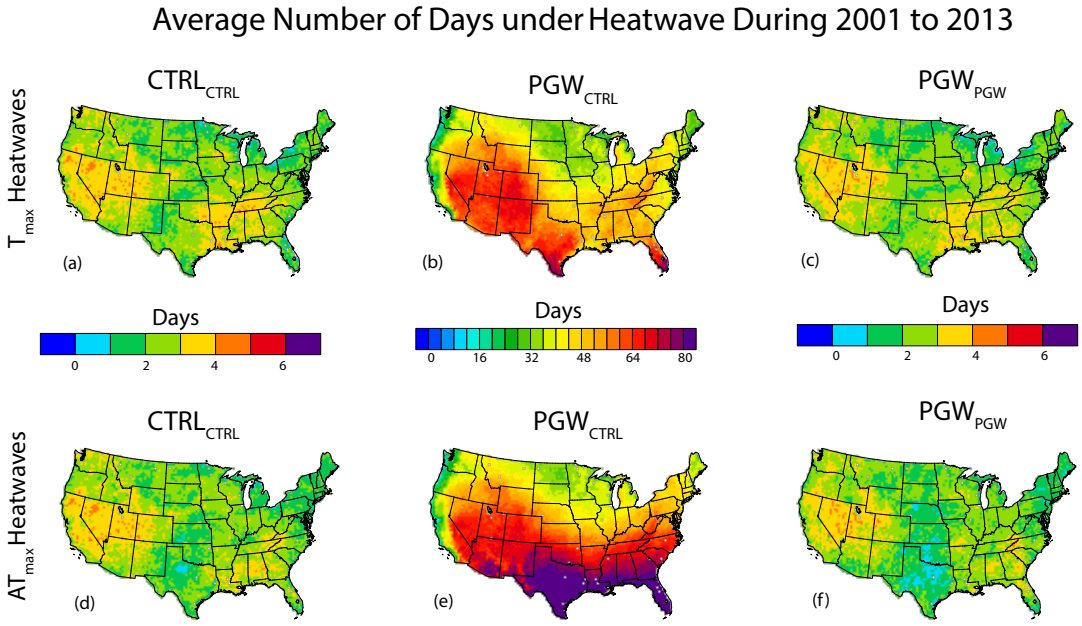

Figure 3.6 Average number of days under T_{max} and AT_{max} heatwaves during (a,d) $CTRL_{CTRL}$ (b,e) PGW_{CTRL} and (c,f) PGW_{PGW} respectively.

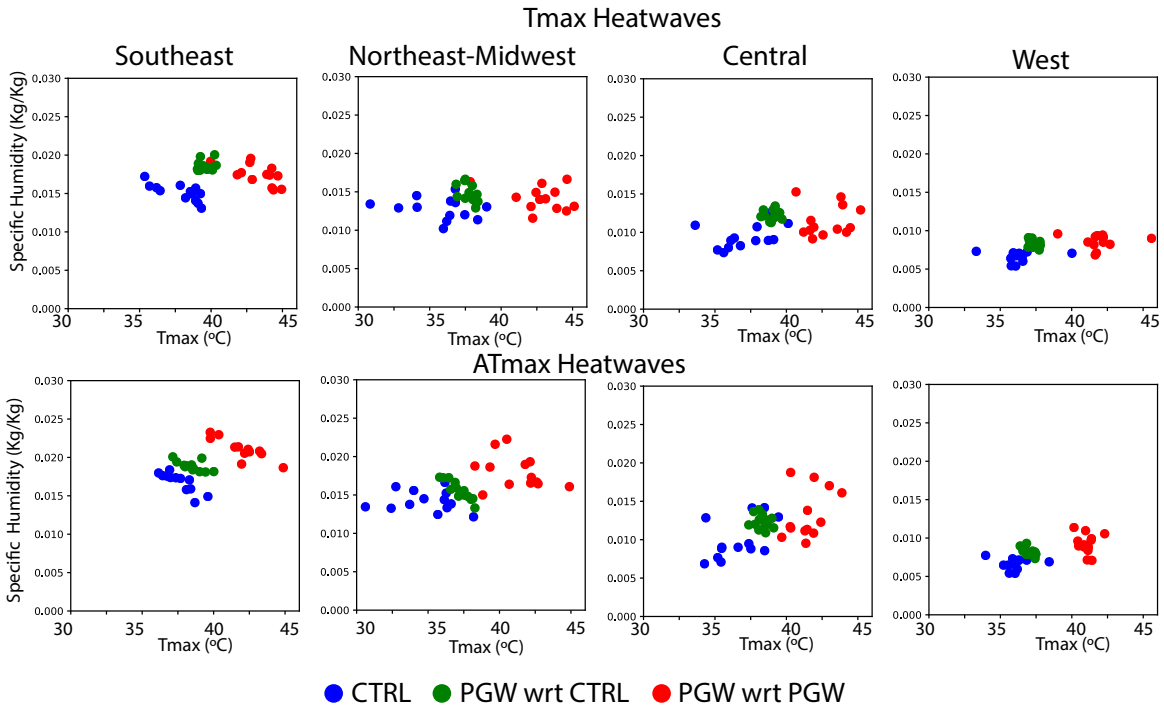

Figure 3.7 Scatter plots between average T_{max} and average specific humidity during (a-d) T_{max} heatwaves (e-h) AT_{max} heatwaves for Southeast, Northeast-Midwest, Central and West US respectively. Each circle represent averages during heatwaves occurring in summer (JJA). Black, blue, green and red circles are used for PRISM, CTRL, PGW_{CTRL} and PGW_{PGW} heatwaves respectively.

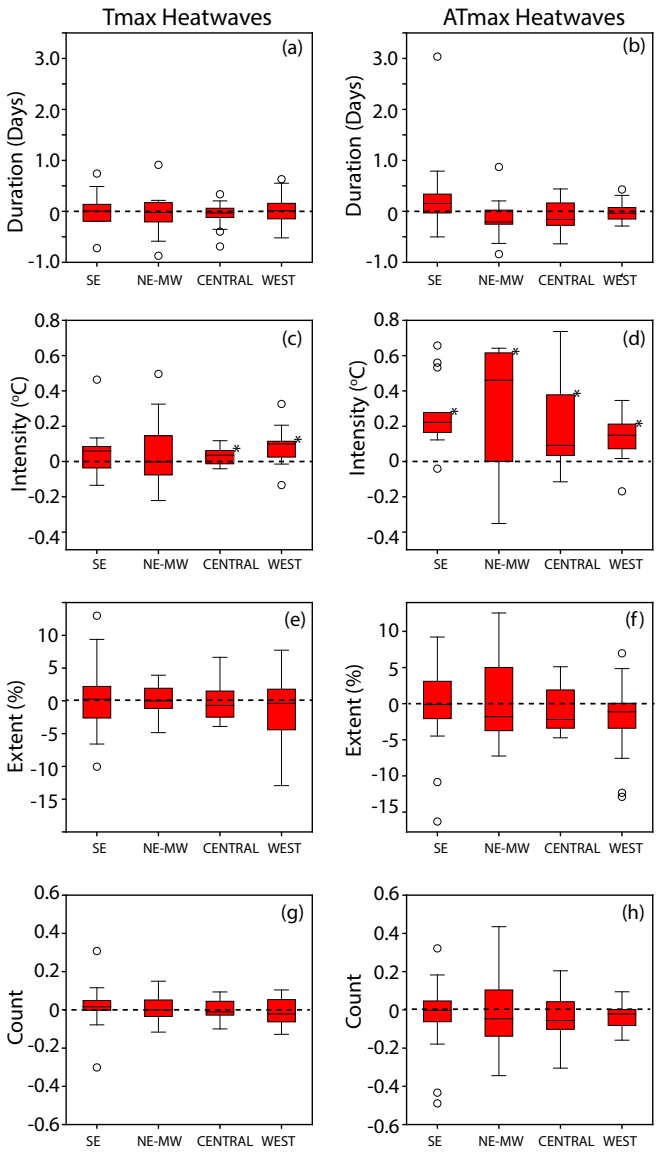

Figure 3.8 Box plots showing the spread in paired differences in characteristics between PGW_{PGWL} and CTRL heatwaves for each year over the 13 year analysis period (2001 to 2013) during T_{max} and AT_{max} heatwaves for (a,b) average duration (c,d) average intensity (e,f) percentage land area (g,h) number respectively. Boxes marked with asterisk sign show significant differences at 95 percent confidence level using two-sided Student's T-test.

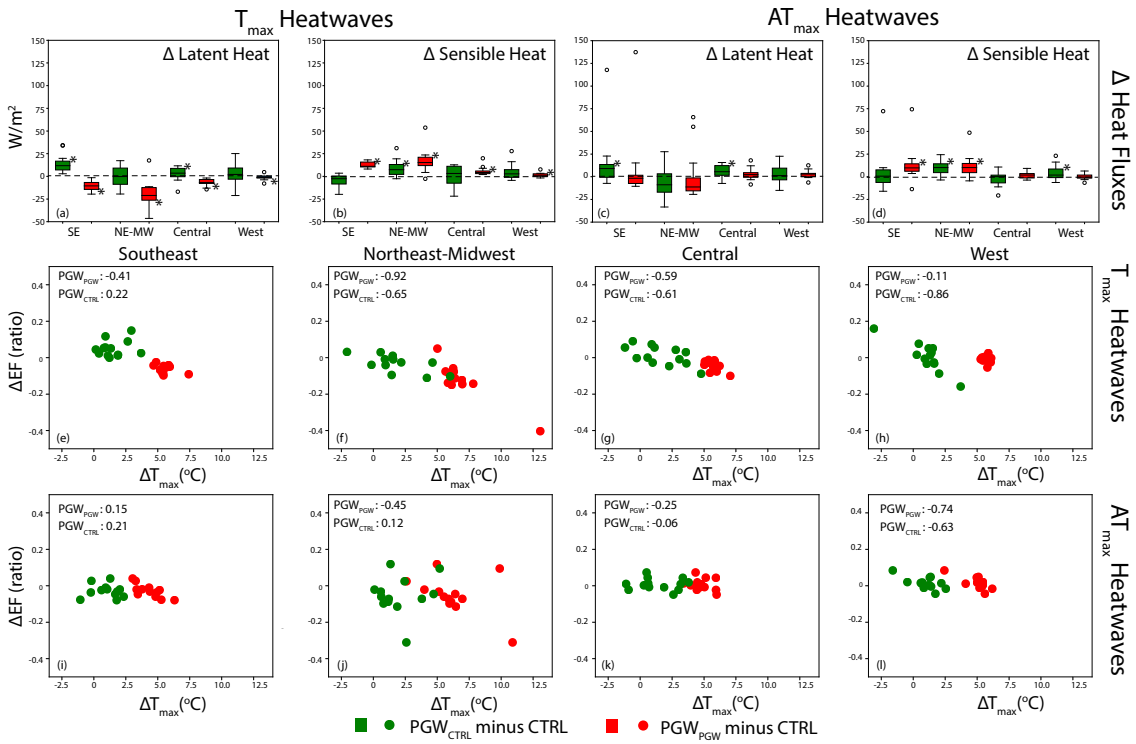

Figure 3.9 Box plots showing the spread in paired differences between years over the 13 year analysis period (2001 to 2013) during T_{max} heatwaves for (a) latent heat (b) sensible heat and during AT_{max} heatwaves for (c) latent heat (d) sensible heat. Green (Red) boxes show the differences between PGW_{CTRL} (PGW_{PGW}) and CTRL heatwaves. Boxes marked with asterisk sign show significant differences at 95 percent confidence level using two-sided Student's T-test. Scatter plot between change in T_{max} and change in evaporative fraction (EF) for T_{max} Heatwaves (e-h) for AT_{max} Heatwaves (i-l) for Southeast, Northeast-Midwest, Central and West US respectively. Green (Red) dots represent change between PGW_{CTRL} (PGW_{PGW}) and CTRL heatwaves for each year during 2001 to 2013 period. The number inside the plots are correlation coefficients between changes in T_{max} and EF during PGW_{PGW} minus CTRL heatwaves (marked as PGW_{PGW}) and PGW_{CTRL} minus CTRL (marked as PGW_{CTRL}).

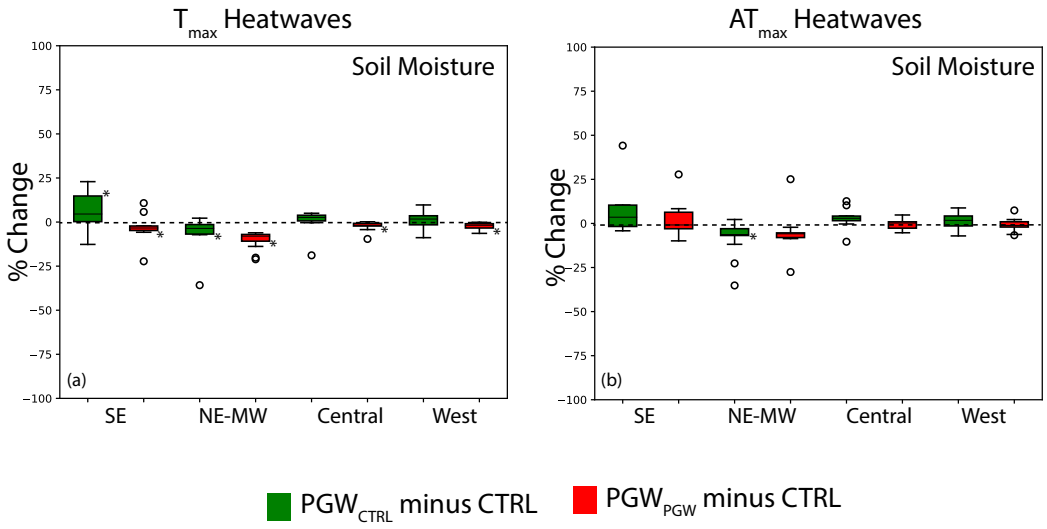

Figure 3.10 Box plots showing the spread in paired differences in soil moisture between years over the 13 year analysis period (2001 to 2013) during (a) T_{max} heatwaves (b) AT_{max} heatwaves. Green (Red) boxes show the differences between PGW_{CTRL} (PGW_{PGW}) and CTRL heatwaves. Boxes marked with asterisk sign show significant differences at 95 percent confidence level using two-sided Student's T-test.

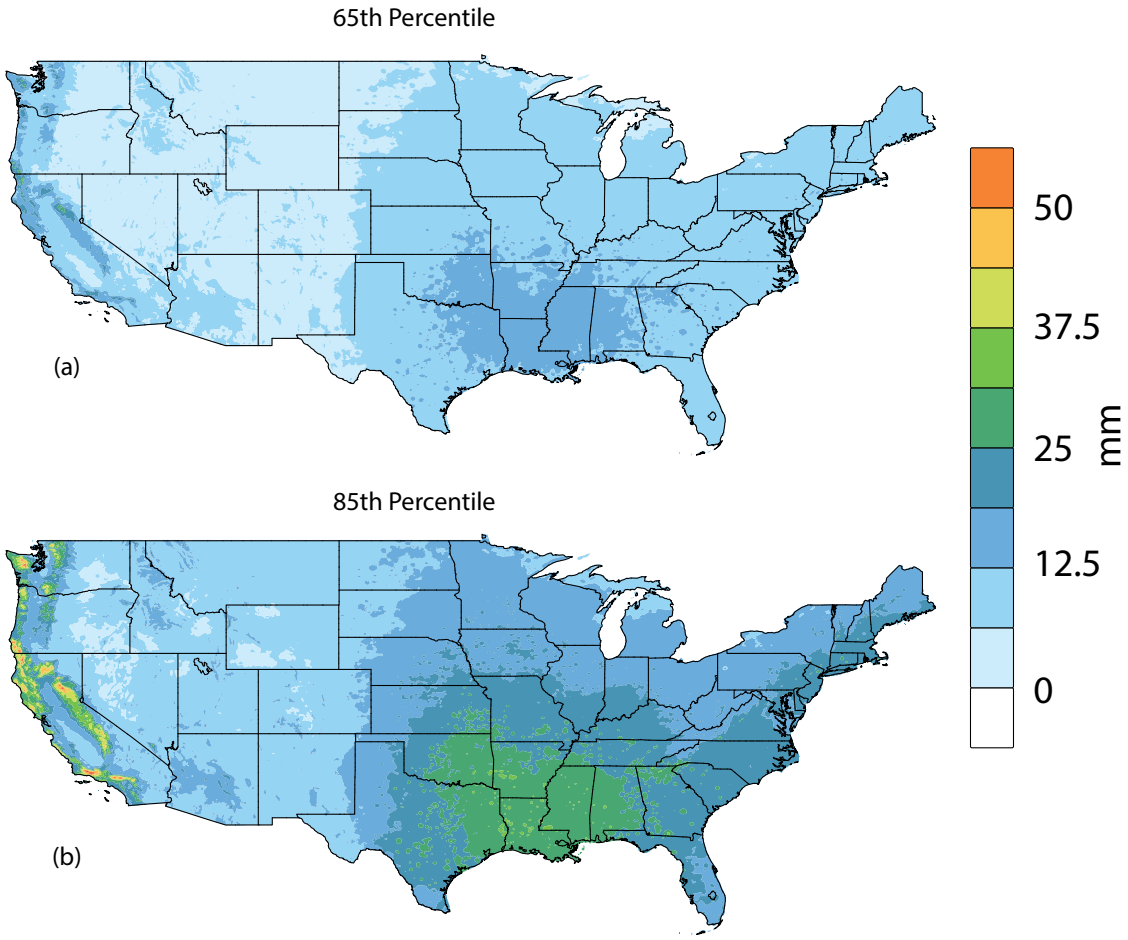

Figure 4.1 a) 65th b) 85th percentile of daily precipitation in observations (PRISM)

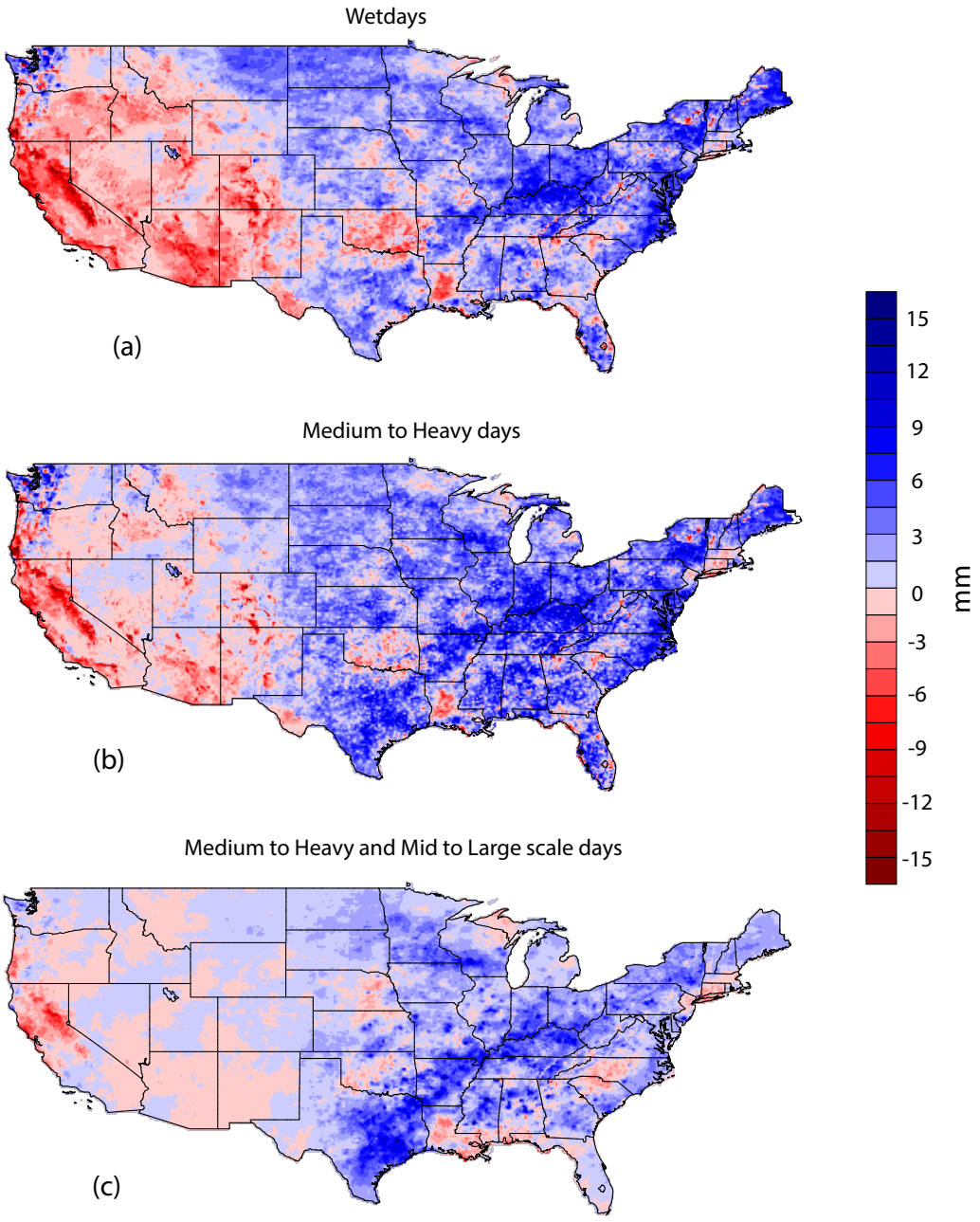

Figure 4.2 Total change in precipitation during a) Wetdays (>1mm) b) Medium to Heavy days (>12.5 mm) c) Medium to Heavy days with Mid to Large spatial scale (> 200 thousand sq. km.) over 1981 to 2016 period.

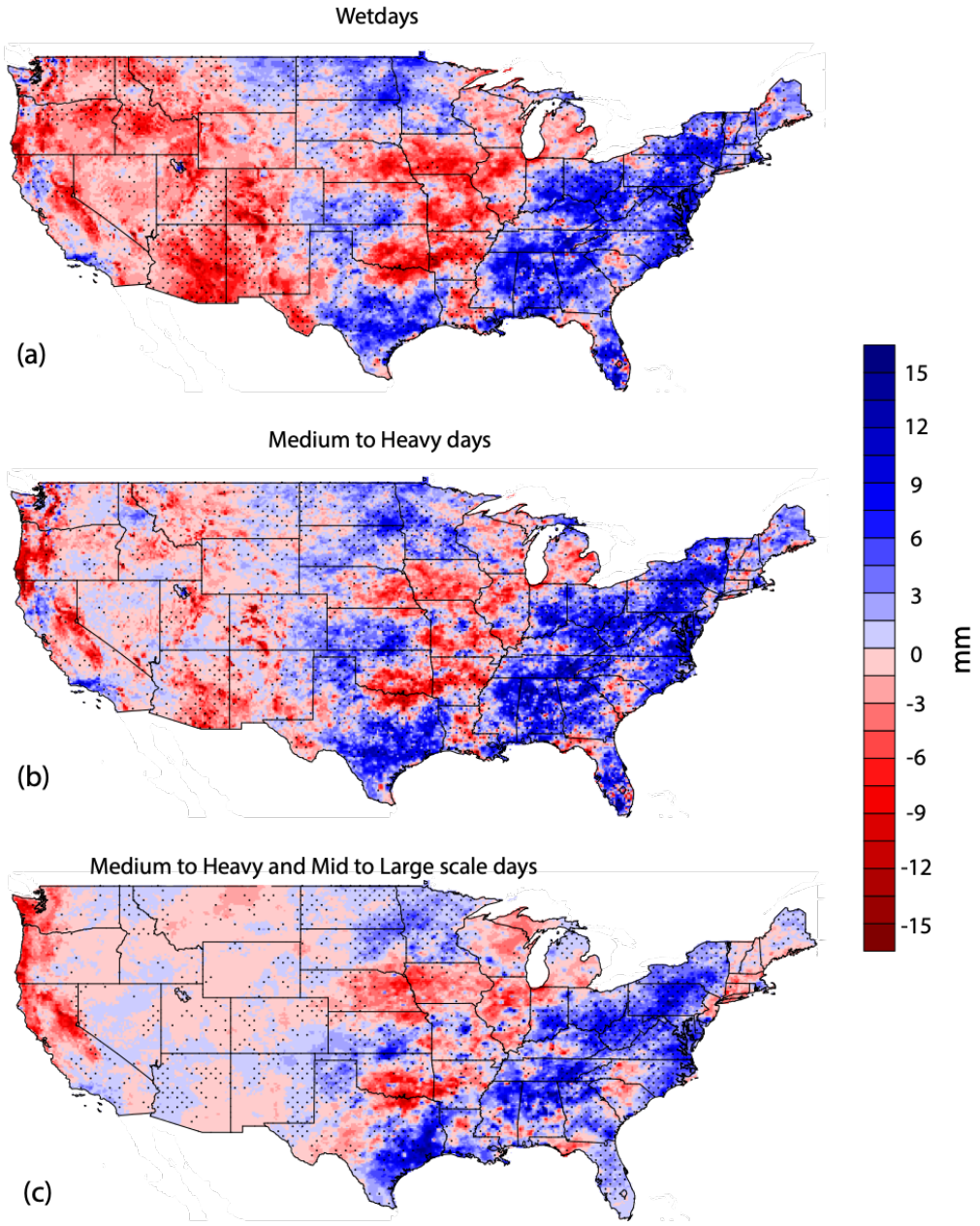

Figure 4.3 Same as Figure 4.2 but for 1981- 2005 period. Stippled area show the region where sign of change is robustly simulated by the RCMs.

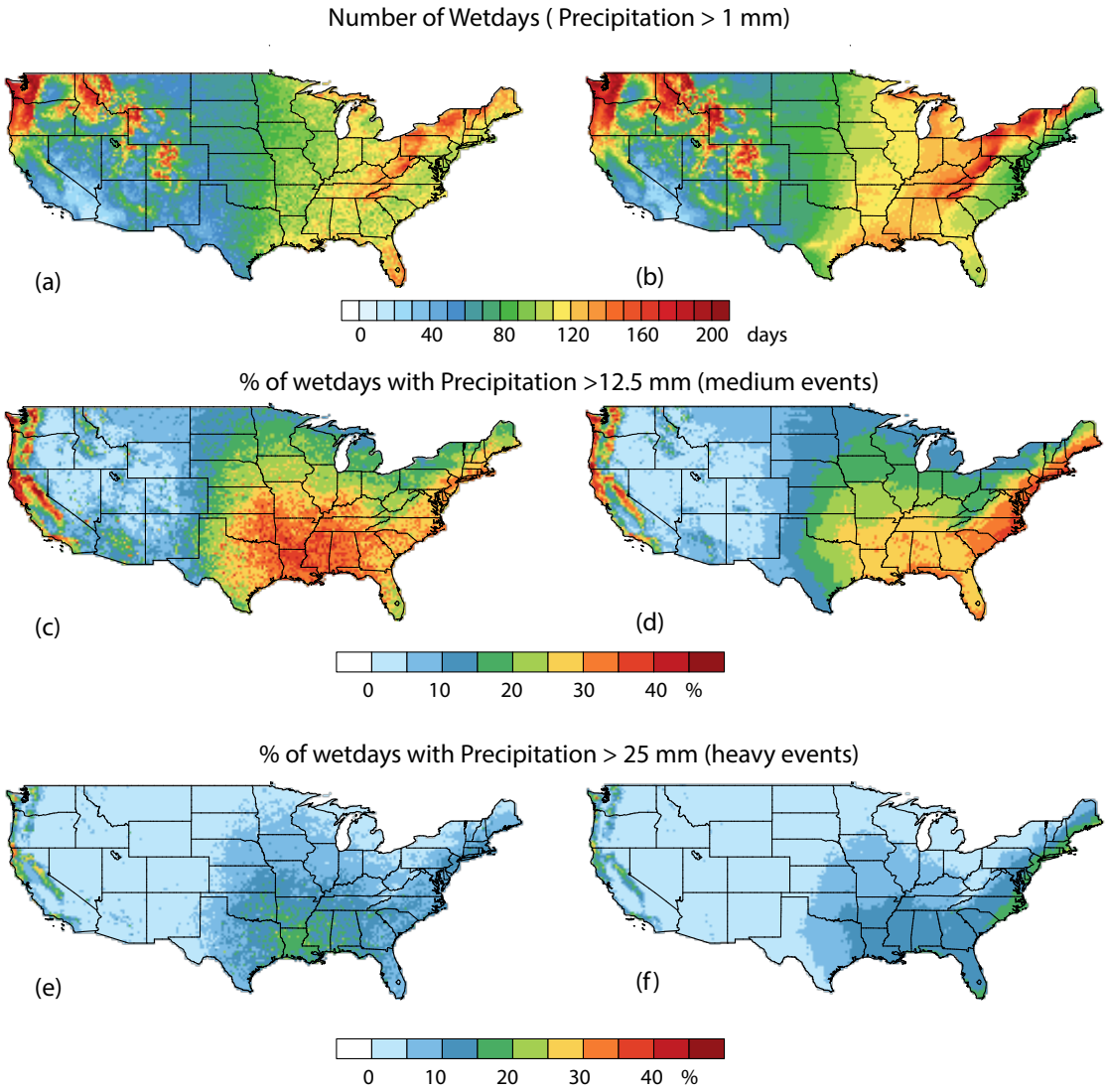

Figure 4.4 Total number of wetdays , percent of wetdays occurring as T_i days and percent of wetdays occurring as H_i days in (a, c, e) Observation (b, d, f) PRISM respectively.

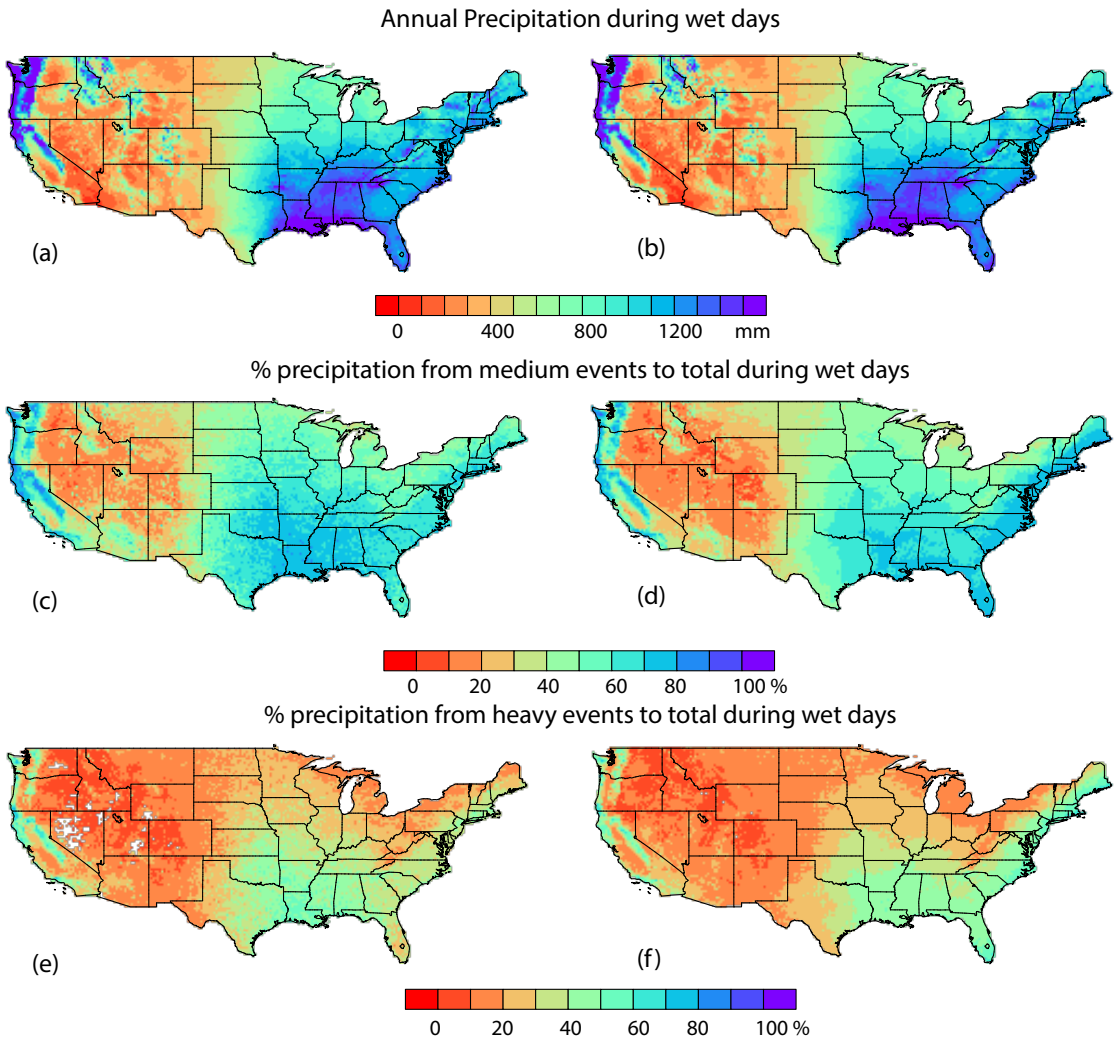

Figure 4.5 Precipitation from wetdays , percent of precipitation from wetdays occurring during Ti days and percent of precipitation from wetdays occurring during Hi days in (a, c, e) Observation (b, d, f) PRISM respectively.

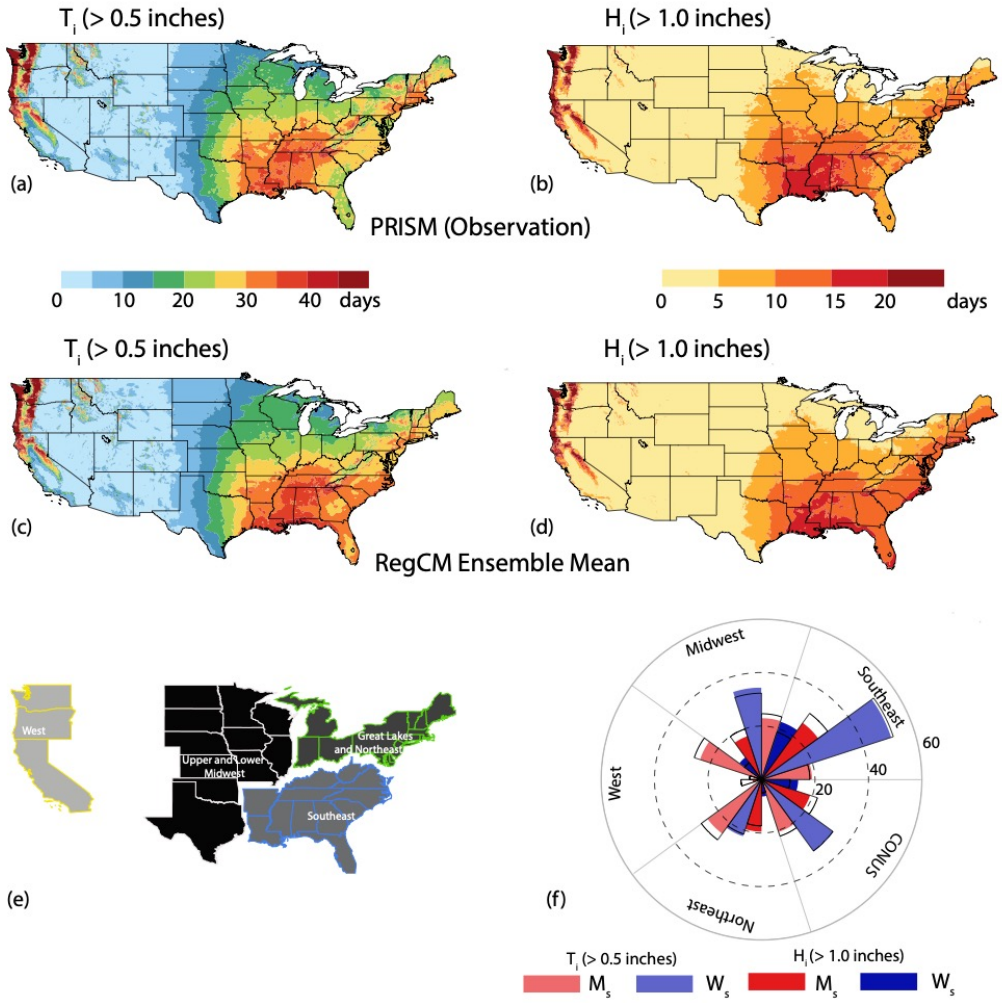

Figure 4.6 Spatial maps showing annual frequency of precipitation events >0.5 inch (T_i) and >1.0 inch (H_i) in PRISM observations (a and b) and RCM ensemble mean (c and d). (e) Four regions for regional analysis. (f) Polar map showing simulated percentage of the annual precipitation contributed by M_s (red) and W_s (green) during T_i (light colors) and H_i events (strong colors). Black hollow lines represent magnitudes based on the PRISM observations.

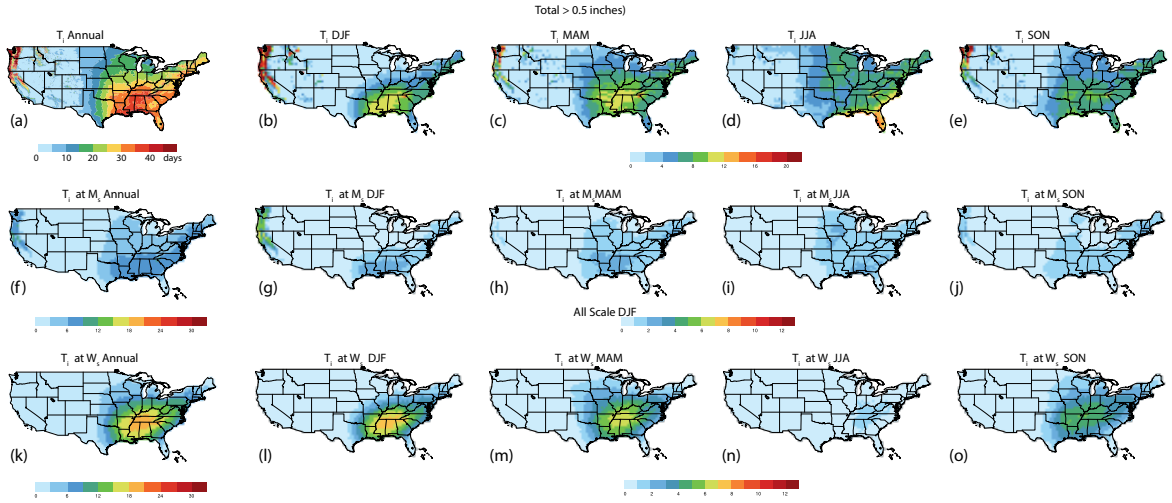

Figure 4.7 Spatial maps showing number of (a-e) T_i events (f-j) T_i events at Ms scale (k-o) T_i events at W_s scale annual and seasonal across the US averaged over 1981-2005 period.

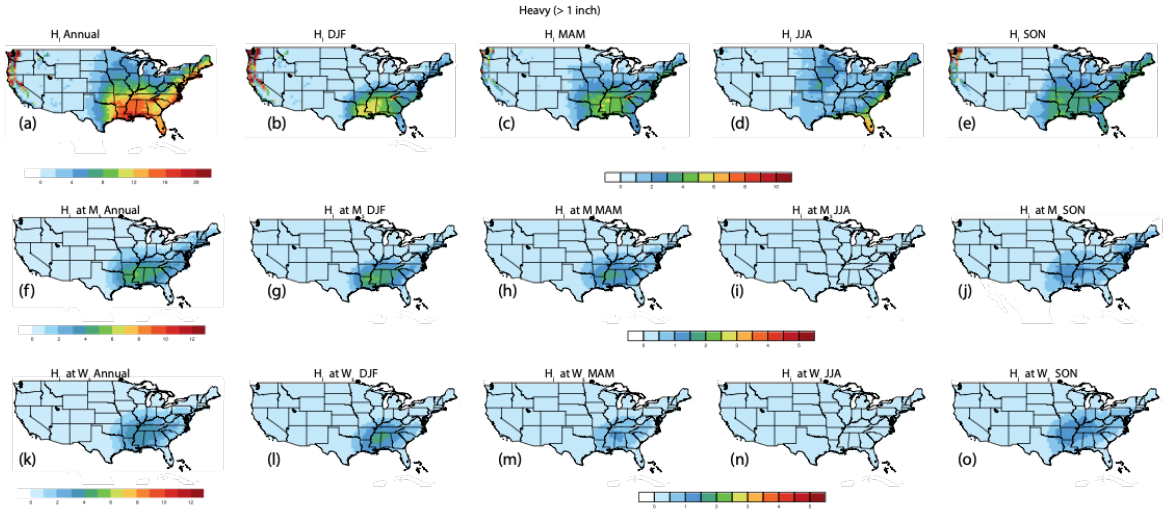

Figure 4.8 Spatial maps showing number of (a-e) H_i events (f-j) H_i events at M_s scale (k-o) H_i events at W_s scale annual and seasonal across the US averaged over 1981-2005 period.

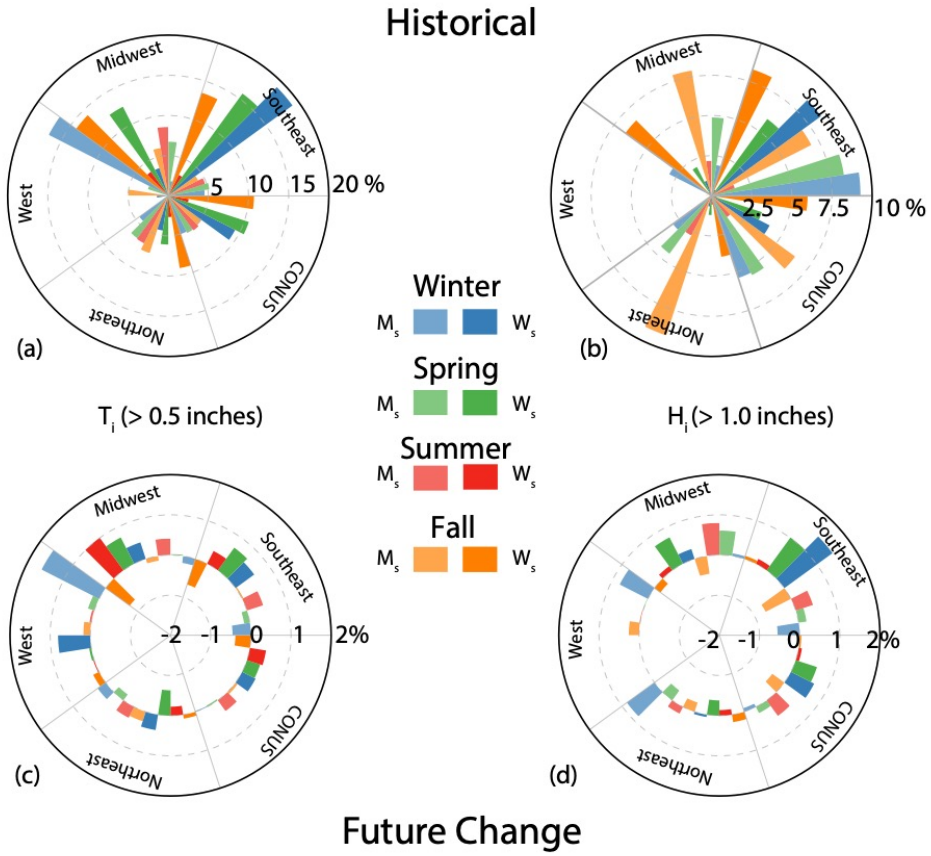

Figure 4.9 Polar map showing simulated historical (1966-2005) percentage of the seasonal precipitation for (a) T_i events (b) H_i events, projected changes (2011-2050 with respect to 1966-2005) in the percentages (c) H_i events (d) T_i events contributed during Winter (blue), Spring (green), Summer (red) and Fall (orange), for M_s events (light colors) and W_s events (strong colors).

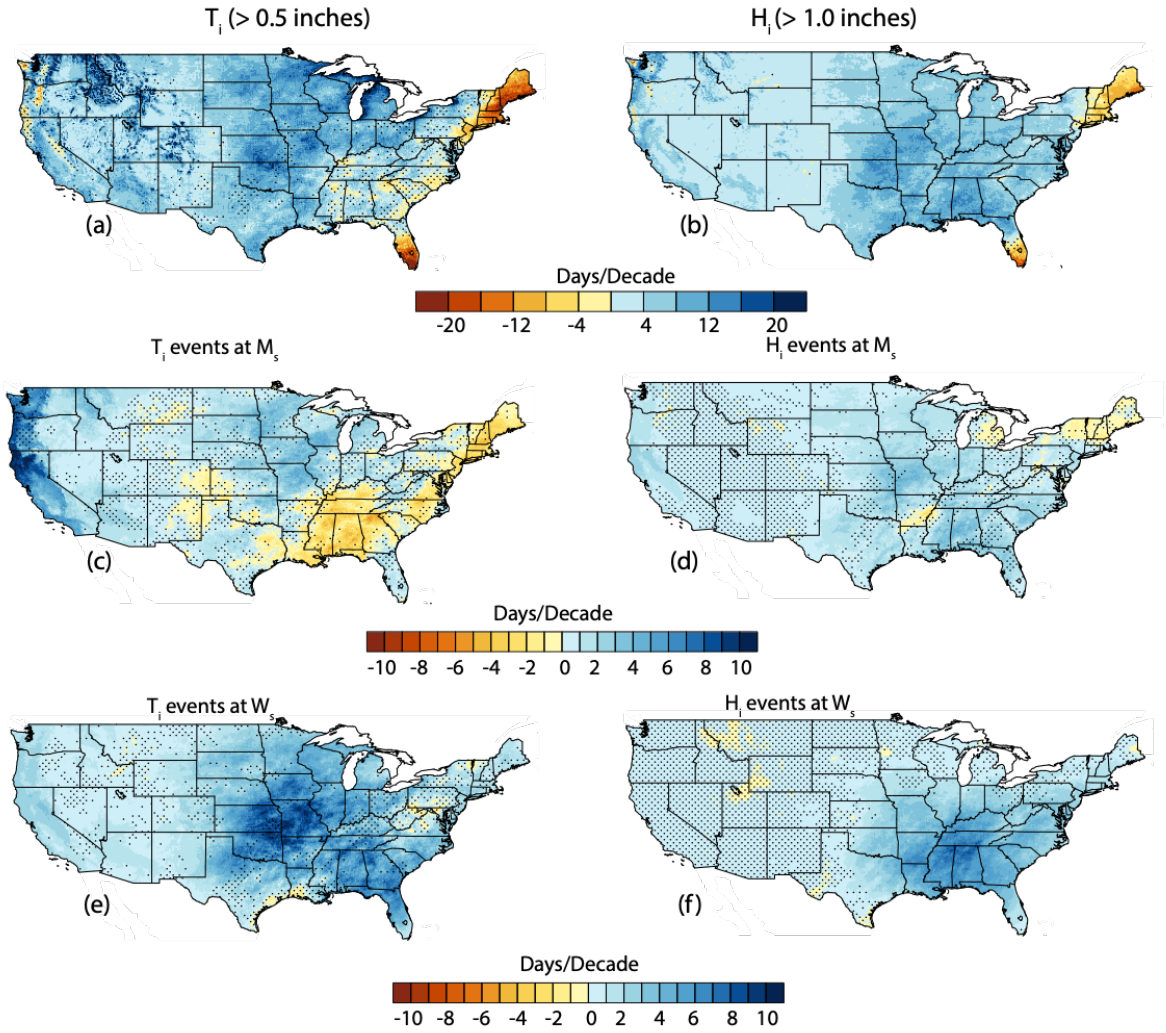

Figure 4.10 Projected changes (2011 to 2050 minus 1966 to 2005) in a) T_i events b) H_i events c) T_i events at M_s scale d) H_i events at M_s scale e) T_i events at W_s scale f) H_i events at W_s scale. Stippled where less than 8 models agree i.e. not robust.

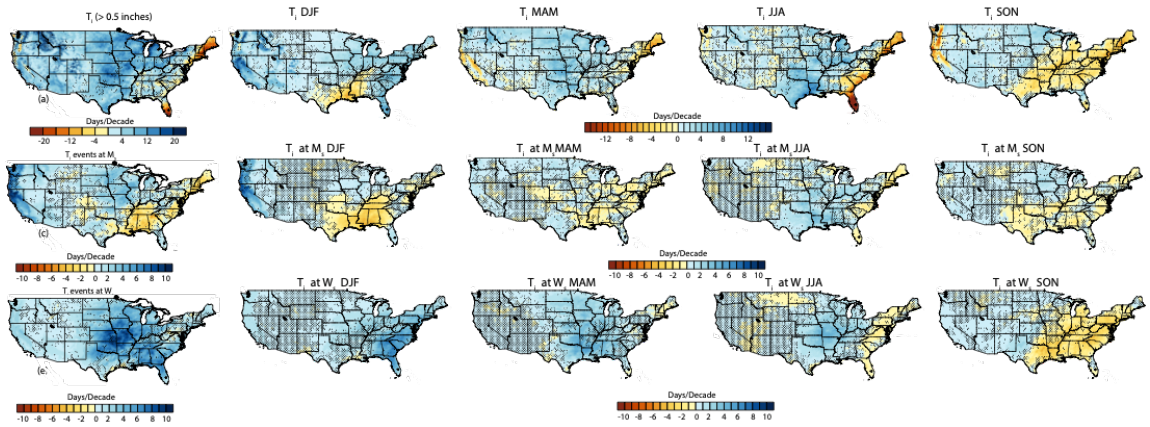

Figure 4.11 Projected changes (2011 to 2050 minus 1966 to 2005) in annual and seasonal number of (a-d) T_i events (e-h) T_i events at M_s scale (i-l) T_i events at W_s scale. Stippled where less than 8 models agree i.e. not robust.

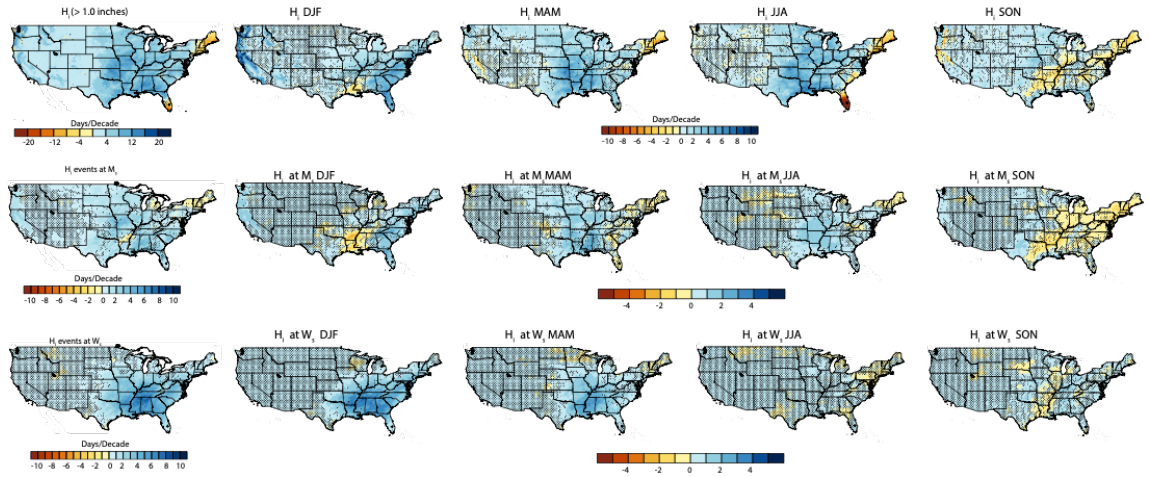

Figure 4.12 Projected changes (2011 to 2050 minus 1966 to 2005) in annual and seasonal number of (a-d) H_i events (e-h) H_i events at M_s scale (i-l) H_i events at W_s scale. Stippled where less than 8 models agree i.e. not robust.

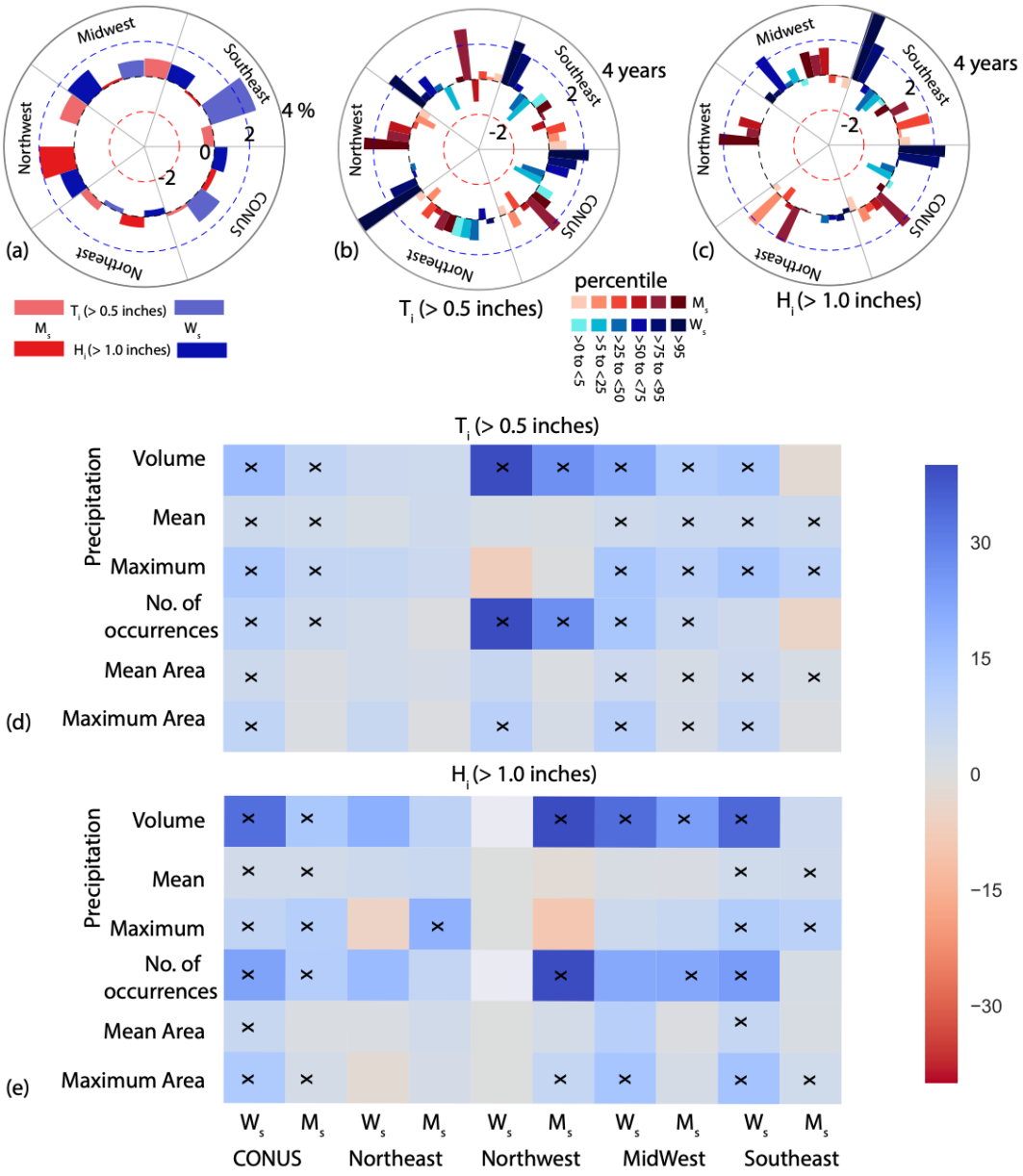

Figure 4.13 Polar maps showing a) projected changes (2011 to 2050 minus 1966 to 2005) in percentage of precipitation contributed by T_i and H_i events at M_s and W_s scales. Polar maps showing projected changes in number of years with frequency of (b) T_i and (c) H_i events falling within the six percentiles as shown. Heat maps showing projected percentage changes in precipitation event volume, mean, maximum, frequency, mean area and maximum area for (d) T_i events (e) H_i events at M_s and W_s scales. Projected changes are significant at 95% confidence interval if a cell is marked with x.

Table 5.1 Selected historic extreme storms in the ACT river basin along with Daymet/PRISM observations and CFSR-WRF-CT simulation results. The R2 and RMSE between CFSR-WRF-CT and Daymet/PRISM are also reported.

N	Period	72-hour ACT domain average precipitation (mm/72 hours)							
		Daymet	PRISM	CFSR-WRF-CT simulation					
				P1	P2	P3	P4	P5	P6
1	02/10/1981–02/12/1981 W	92	90	99	91	79	111	99	93
2	02/01/1982–02/03/1982 W	88	86	82	76	67	92	82	80
3	04/07/1983–04/09/1983 W	81	78	104	96	90	133	115	128
4	12/02/1983–12/04/1983 W	72	73	50	47	43	62	54	56
5	01/15/1987–01/17/1987 W	74	68	53	52	48	65	58	60
6	02/27/1987–03/01/1987 W	71	75	63	63	58	72	68	69
7	09/29/1989–10/01/1989 S	90	84	105	106	97	132	126	128
8	02/15/1990–02/17/1990 W	82	79	46	40	37	66	51	62
9	03/16/1990–03/18/1990 W	148	160	131	120	113	144	131	130
10	02/18/1991–02/20/1991 W	74	73	40	39	35	50	45	46
11	03/02/1991–03/04/1991 W	82	85	78	72	66	92	81	83
12	12/01/1991–12/03/1991 W	71	70	48	45	41	63	55	58
13	10/03/1995–10/05/1995 S	173	173	164	155	150	192	174	189
14	03/06/1996–03/08/1996 W	83	81	61	54	48	89	77	80
15	09/24/1997–09/26/1997 S	66	61	54	48	47	69	58	66
16	10/25/1997–10/27/1997 S	81	73	90	76	71	134	108	125
17	01/06/1998–01/08/1998 W	97	97	65	62	57	82	76	82
18	03/07/1998–03/09/1998 W	105	98	79	74	72	117	94	116
19	09/28/1998–09/30/1998 S	117	118	88	85	78	114	106	107
20	09/25/2002–09/27/2002 S	103	102	80	79	76	102	94	103
21	05/06/2003–05/08/2003 S	67	69	61	43	43	113	92	99
22	06/30/2003–07/02/2003 S	92	84	95	94	92	125	114	127
23	09/06/2004–09/08/2004 S	28	26	34	31	31	40	39	38
24	09/16/2004–09/18/2004 S	128	122	118	112	112	132	121	133
25	08/24/2008–08/26/2008 S	121	117	126	120	118	174	164	167

Table 5.1 continued

N	Period	72-hour ACT domain average precipitation (mm/72 hours)							
		Daymet	PRISM	CFSR-WRF-CT simulation					
				P1	P2	P3	P4	P5	P6
26	12/10/2008–12/12/2008 [W]	111	108	98	87	77	116	99	98
27	03/26/2009–03/28/2009 [W]	105	101	102	96	86	114	103	103
28	11/10/2001–11/12/2001 [S]	77	79	73	70	68	73	70	69
29	05/02/2010–05/04/2010 [S]	84	82	73	65	61	92	78	86
30	09/04/2011–09/06/2011 [S]	109	115	140	141	132	177	164	177
			R^2 – Daymet	**0.725**	0.703	0.706	0.620	0.626	0.605
			R^2 – PRISM	**0.704**	0.683	0.681	0.580	0.595	0.558
			RMSE – Daymet (mm)	**19**	22	25	26	21	24
			RMSE – PRISM (mm)	**19**	22	25	28	22	26

Note: W—storms occur during winter/spring; S—storms occur during summer/fall

Figure 5.1 Study area showing the nested WRF domain and ACT basin.

Table 5.2 Six sets of cumulus parameterizations and cloud microphysics schemes tested in this study.

WRF no.	Cumulus parameterization	Cloud microphysics scheme
P1	Grell-Devenyi ensemble scheme	Lin et al.
P2	Grell-Devenyi ensemble scheme	WRF Single Moment 5-class scheme
P3	Grell-Devenyi ensemble scheme	Thompson scheme
P4	Kain-Fritsch scheme	Lin et al.
P5	Kain-Fritsch scheme	WRF Single Moment 5-class scheme
P6	Kain-Fritsch scheme	Thompson scheme

Note: In addition, the Mellor-Yamada-Janjic (Eta) TKE boundary layer scheme, Rapid Radiative Transfer model for long wave, and Dudhia scheme for short wave are used.

Table 5.3 List of CCSM4-WRF 5-day simulations for the ACT river basin and their maximum 72-hour domain average precipitation.

N	CCSM4-WRF 5-day simulation starting date and maximum 72-hour domain average precipitation					
	1981–2010 baseline		2021–2050 near future		2071–2100 far future	
	Starting date	Max. 72-hour precip. (mm)	Starting date	Max. 72-hour precip. (mm)	Starting date	Max. 72-hour precip. (mm)
1	12/09/1983 W	116	02/04/2022 W	86	11/24/2076 S	75
2	02/16/1984 W	49	06/02/2023 S	56	02/18/2077 W	115
3	12/18/1984 W	116	11/22/2023 S	41	09/24/2079 S	77
4	03/29/1985 W	78	05/03/2024 S	68	01/05/2080 W	89
5	02/21/1987 W	61	03/13/2026 W	73	02/20/2080 W	70
6	11/11/1987 S	54	01/01/2029 W	106	05/29/2080 S	63
7	03/27/1989 W	58	01/14/2029 W	100	10/20/2080 S	98
8	02/19/1991 W	67	11/13/2029 S	53	03/31/2082 W	100
9	02/26/1991 W	95	01/20/2031 W	44	03/22/2083 W	71
10	11/29/1992 S	136	07/31/2032 S	80	02/15/2084 W	77
11	12/04/1992 W	61	11/27/2033 S	83	03/10/2084 W	119
12	03/11/1994 W	70	03/15/2034 W	65	02/27/2085 W	103
13	02/10/1997 W	73	01/26/2037 W	105	02/25/2088 W	94
14	09/01/1997 S	69	12/21/2037 W	40	11/04/2088 S	67
15	12/30/1997 W	112	02/16/2038 W	52	03/31/2089 W	43
16	11/10/1998 S	78	11/24/2038 S	117	04/01/2091 W	100
17	03/30/1999 W	53	02/25/2039 W	53	01/02/2092 W	66
18	01/24/2000 W	83	04/30/2040 W	77	03/17/2092 W	90
19	03/13/2000 W	75	02/06/2041 W	67	12/18/2092 W	99
20	11/09/2001 S	51	03/24/2042 W	113	01/24/2093 W	65
21	04/18/2003 S	52	11/25/2042 S	87	01/31/2093 W	71
22	11/01/2003 S	53	03/13/2043 W	89	02/09/2094 W	135
23	12/15/2003 W	58	11/30/2043 S	89	04/20/2096 W	62
24	01/11/2004 W	60	04/23/2045 W	75	10/31/2096 S	95
25	02/01/2004 W	114	01/29/2046 W	76	12/04/2096 W	77
26	11/16/2005 S	52	03/11/2046 W	89	01/16/2097 W	69

Table 5.3 continued

N	CCSM4-WRF 5-day simulation starting date and maximum 72-hour domain average precipitation					
	1981–2010 baseline		2021–2050 near future		2071–2100 far future	
	Starting date	Max. 72-hour precip. (mm)	Starting date	Max. 72-hour precip. (mm)	Starting date	Max. 72-hour precip. (mm)
27	03/26/2007 W	86	04/06/2046 W	44	02/15/2097 W	146
28	01/03/2010 W	88	12/25/2048 W	93	02/26/2098 W	119
29	02/04/2010 W	94	03/12/2049 W	65	12/15/2099 W	64
30	04/22/2010 W	54	12/27/2049 W	49	04/06/2100 W	80

Note: W—storms occur during winter/spring; S—storms occur during summer/fall

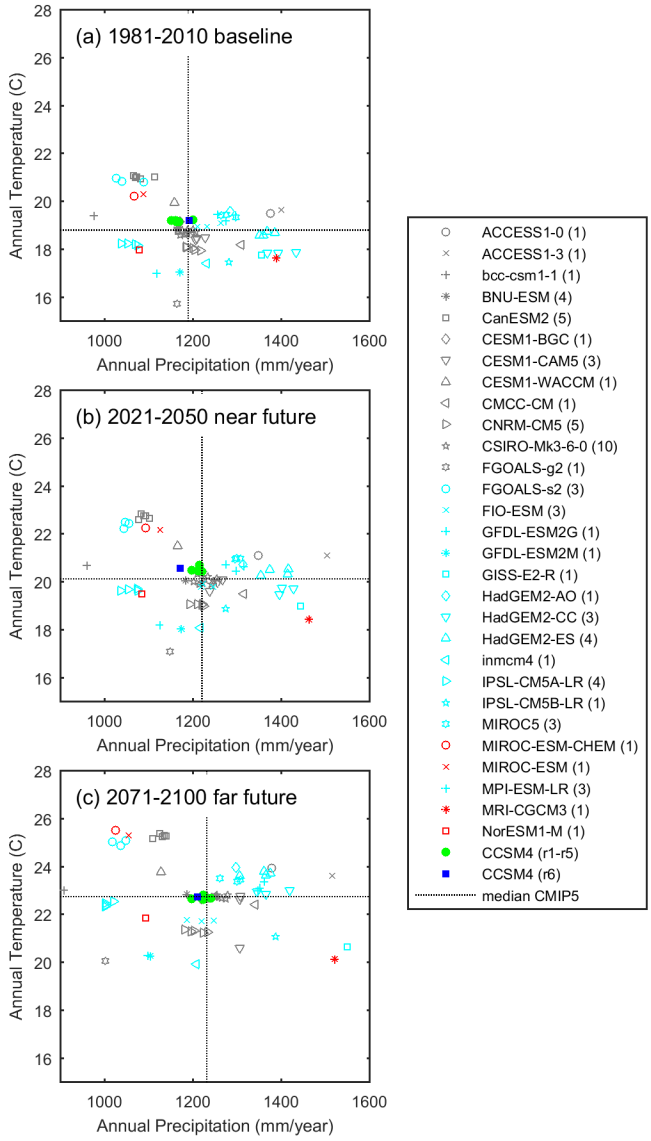

Figure 5.2 Scatter plots of mean annual temperature and precipitation averaged over the outer WRF domain for 70 CMIP5 climate simulations from 30 GCMs under (a) 1981–2010 baseline (with 1981–2005 20th century and 2006–2010 RCP 8.5 experiments), (b) 2021–2050 near future, and (c) 2071–2100 far future periods. Blue squares denote CCSM4-r6i1p1, green full circles denote the other five ensemble members of CCSM4, and all other symbols denote the remaining 64 CMIP5 simulations. The number of ensemble members of each GCM is marked in parentheses after the GCM name. Dashed lines denote the ensemble median of 70 CMIP5 simulations.

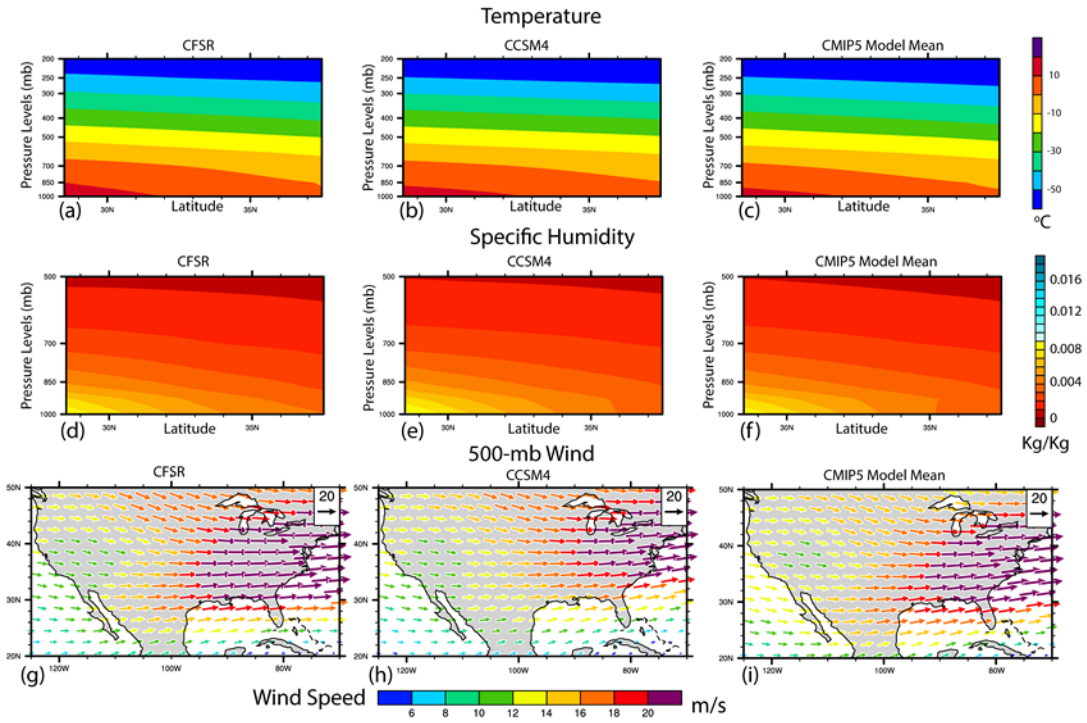

Figure 5.3 Comparison of 1981–2005 synoptic winter air temperature (°C, upper row), winter specific humidity (kg/kg, central row), and winter 500-mb wind (m/s, lower row) for CFSR (left column), CCSM4-r6i1p1 (central column), and CMIP5 multi-model mean (right column). Both air temperature (panels a–c) and specific humidity (panels d–e) are summarized in terms of zonal means at various pressure levels for the inner ACT WRF domain. The synoptic 500-mb wind direction and magnitude are illustrated for the entire United States (panels g–i). Winter months include December, January, and February.

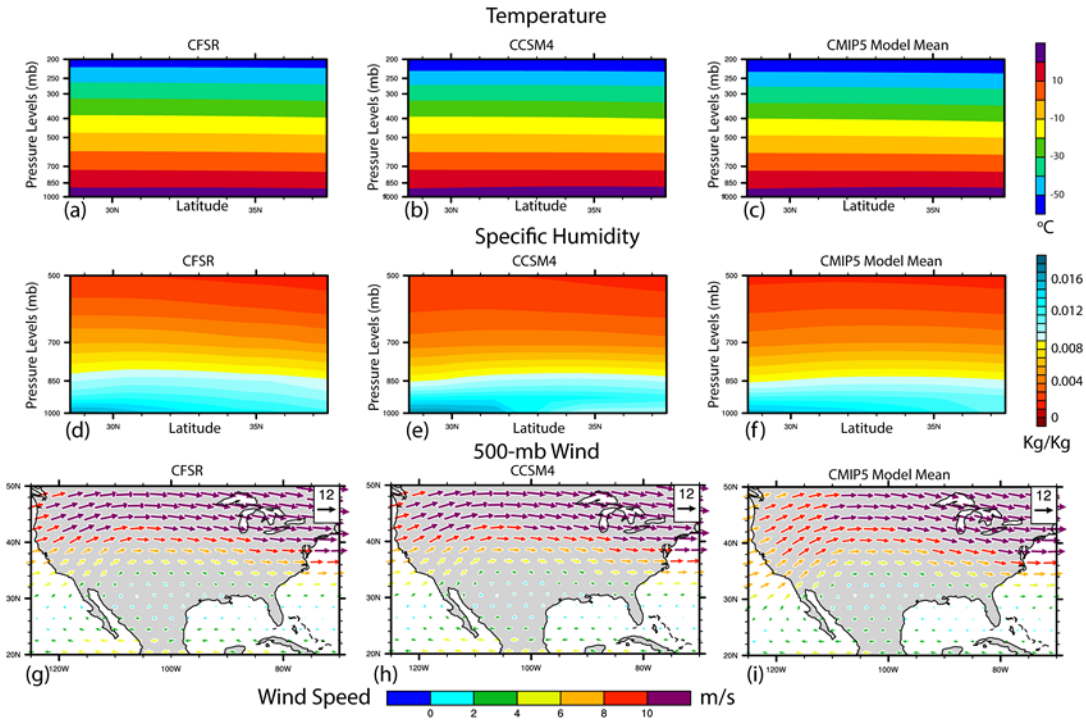

Figure 5.4 Comparison of 1981–2005 synoptic summer air temperature (°C, upper row), summer specific humidity (kg/kg, central row), and summer 500-mb wind (m/s, lower row) for CFSR (left column), CCSM4-r6i1p1 (central column), and CMIP5 multi-model mean (right column). Both air temperature (panels a–c) and specific humidity (panels d–e) are summarized in terms of zonal means at various pressure levels for the inner ACT WRF domain. The synoptic 500-mb wind direction and magnitude are illustrated for the entire United States (panels g–i). Summer months include June, July, and August.

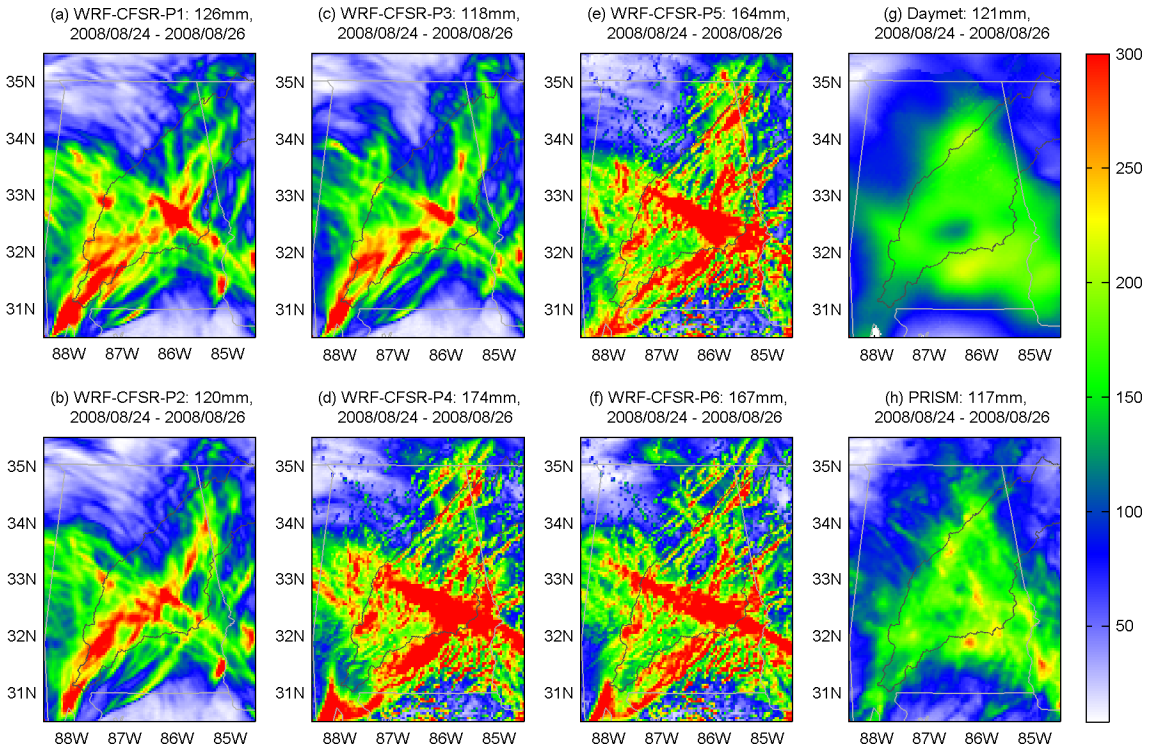

Figure 5.5 Example of WRF tuning for the 2008/08/24 – 2008/08/26 storm over the ACT river basin. Panels (a) to (f) show CFSR-WRF simulations using different parameterization schemes. The observations from Daymet and PRISM are shown in panels (g) and (h).

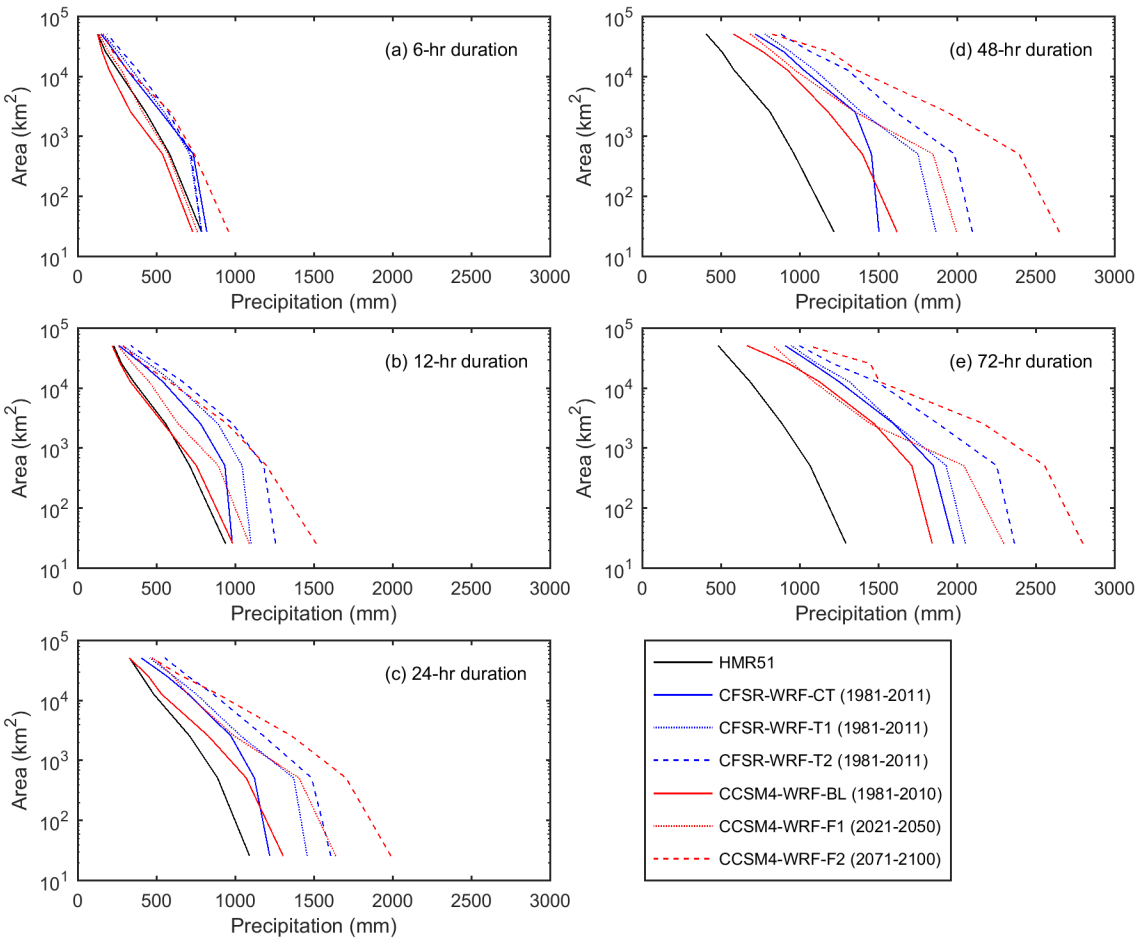

Figure 5.6 Conventional and simulated PMP for (a) 6-hour, (b) 12-hour, (c) 24-hour, (d) 48-hour, and (e) 72-hour storm durations.

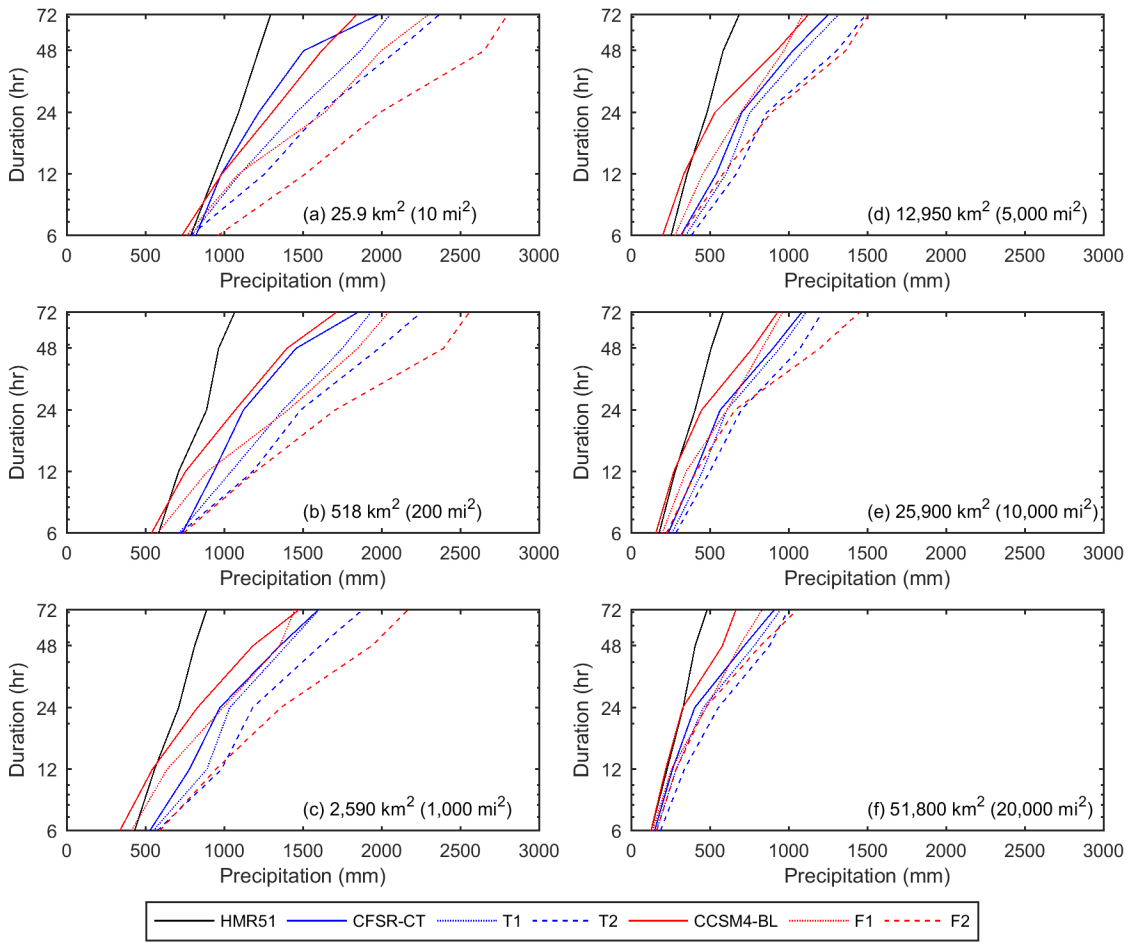

Figure 5.7 Conventional and simulated PMP for (a) 25.9-km^2 (10-mi^2), (b) 518-km^2 (200-mi^2), (c) 2,590-km^2 (1,000-mi^2), (d) 12,950-km^2 (5,000-mi^2), (e) 25,900-km^2 (10,000-mi^2), and (f) 51,800-km^2 (20,000-mi^2) storm areas.

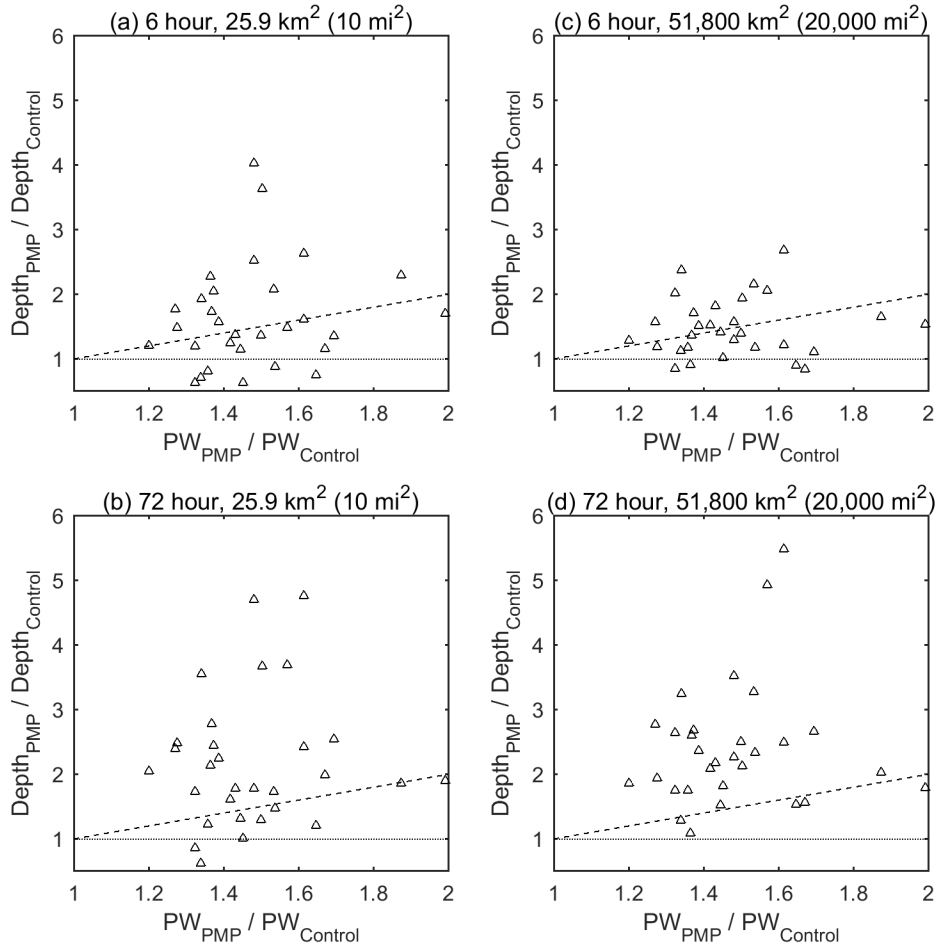

Figure 5.8 Change in precipitable water (PW_{PMP} / $PW_{Control}$) versus change in rainfall depth ($Depth_{PMP}$ / $Depth_{Control}$) under (a) 6-hour, 25.9-km^2 (10-mi^2), (b) 72-hour, 25.9-km^2 (10-mi^2), (c) 6-hour, 51,800-km^2 (20,000-mi^2), and (d) 72-hour, 51,800-km^2 (20,000-mi^2) for the 30 CFSR-WRF-CT storms. Broken line represents PW_{PMP} / $PW_{Control}$ = $Depth_{PMP}$ / $Depth_{Control}$ and dotted line represents $Depth_{PMP}$ / $Depth_{Control}$ = 1.

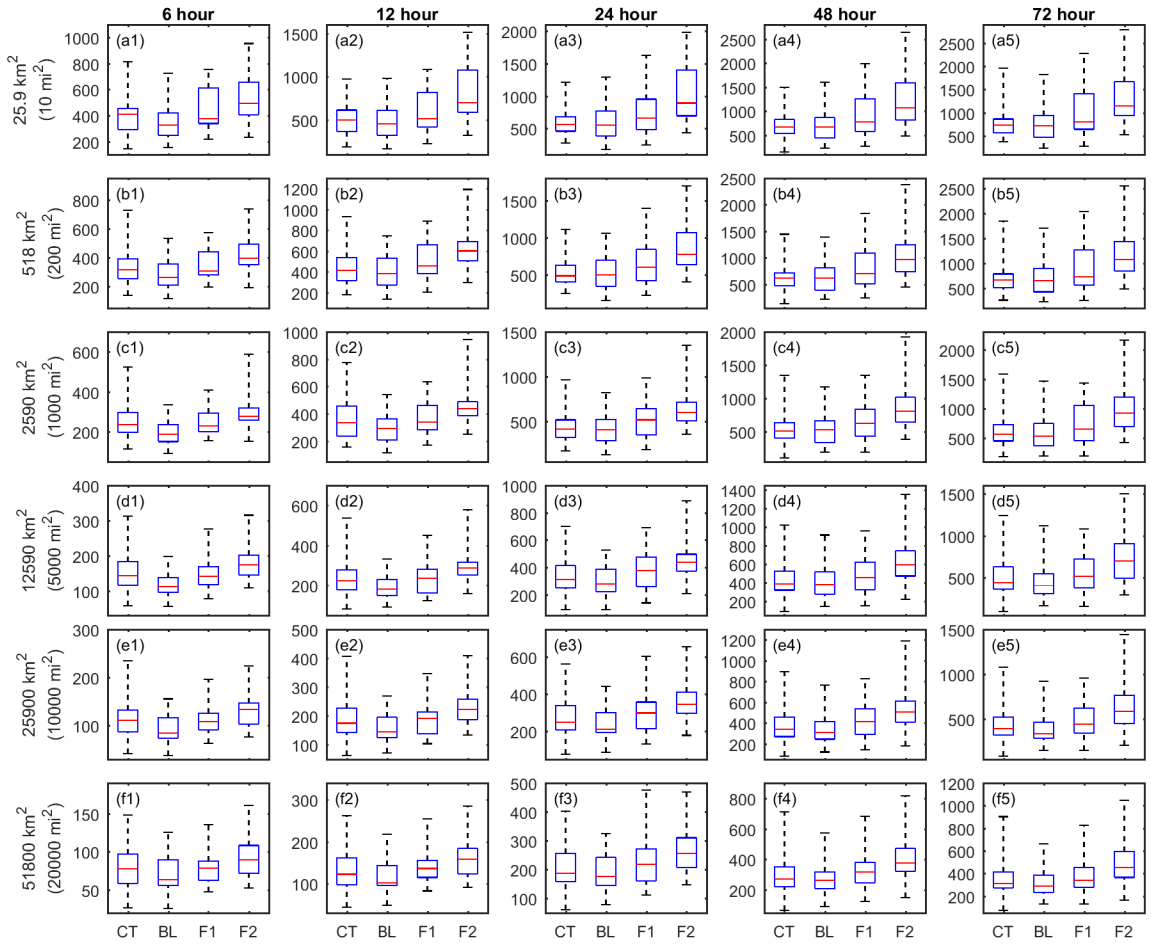

Figure 5.9 Box plot showing the spread of simulated PMP across all 120 storms for different durations and areas, a1 to f5, where letters a through f correspond to areas 25.9 km^2 to 51,800 km^2 and numbers 1 to 6 to durations of from 6 to 72 hours, respectively.

Vita

Deeksha Rastogi is a fellow in The Bredesen Center for Interdisciplinary Research and Graduate Education, at The University of Tennessee, Knoxville and Oak Ridge National Laboratory (ORNL) working towards her Doctor of Philosophy degree in Energy Science and Engineering with a Focus in Environmental and Climate Sciences. She holds a Master of Science (MS) degree in Atmospheric Sciences from University of Illinois at Urbana Champaign and Bachelor of Technology degree in Environmental Engineering from Indian School of Mines, Dhanbad, India. Her research focuses on understanding weather/climate extremes, hydro climate and human systems responses to changing environment at varying spatiotemporal scales. She utilizes a range of earth system modeling tools including numerical models, ensemble of high-resolution model simulations and data analysis to achieve these objectives.